High School Dresden-Bühlau   Model Flight Club Rossendorf

All-day Program Aeromodelling

German Originaltitel:

Ganztagsangebot Modellflug- Ein Begleitheft für den Unterricht
https://www.mfc-rossendorf.de/ > News > Begleitheft > Schrift

Accompanying booklet for lessons

by

Hans Langenhagen

This paper was written in connection with the all-day program Aeromodelling at the high school Dresden-Bühlau. It was started in September 2009 and finished at the beginning of the holidays in July 2019.

Quote Mike Colling:

Why Have an Education Programme?

That is a question that I have been asked more than once and the answer is for a number of reasons. Building and flying model aircraft is a most enjoyable thing to do, I would not do it if I did not enjoy it and I would like more young people to take up the sport.
Model aircraft flying is probably unique in the airsports in having no age limit. It can cost less than any other airsports and can be carried out in just about any reasonable free space both indoors and out. It can be carried out at whatever level you wish from club flying on a Sunday to competing in World Championships.

Model building and flying can be much, much more. For a youngster it can open many new doors to the large world of aviation and technology.
In Britain, the BMFA in collaboration with British Aerospace uses a model building and flying contest in schools as a way to promote interest in Engineering and Technology through flight. The BMFA also promotes model design building and flying with its University Challenge.
A large number of Universities are realising the value of using a model design and building project as a good low cost method to train students in how to problem solve and manage a project.

Colleges of Further education are using models to tempt some young students, about to leave school, to look at a career in aircraft management as an option. Model building and flying can stimulate a youngster's mind and help to keep their desire to enter their chosen airsport when finances allow and the correct age is attained.

_____
Mike Colling was editor of BMFA News magazine (U.K.) for many years.
But he was also active internationally, heading the FAI-CIAM SubCommittee *Education/Technical Experts* for a number of years.
The text is an Extract from *CIAM-flyer Issue #10/March 2000*
https://www.fai.org/sites/default/files/documents/cf2000.pdf
M. Colling kindly authorises the author to include this in his brochure.

Greeting

"Only flying is nicer" - who doesn't know this saying and who hasn't tried to fly with small model airplanes as a child. Everyone very quickly made the experience that in addition to skill in flying, manual skills and technical understanding are also required.

With this brochure, Hans Langenhagen has created a primer on model aircraft construction and model flight. Almost all areas of this very exciting hobby are illuminated, the work steps involved in building are described in detail and the theoretical background is sometimes very intensively examined.
The fact that a phase of the author's life was also put down on paper shows the enthusiasm with which he taught model flying to children, young people and adults from scratch for more than 50 years in the Rossendorf model flying club. The numerous pictures make you want to build model airplanes. At the same time, they are illustrious contemporary witnesses over the decades.

The all-day offer for schools finds a wide space in the presentation. This represents a special form of school education in which school physics should become clearer and more "tangible" for the children based on experience. What is better for this than a model airplane. It is to the credit of Hans Langenhagen that he dedicated himself to this task, giving the children fun experimenting and, quite incidentally, also winning new club members.
The harmony of theory and practice is constantly postulated and finds constant confirmation in the many examples presented. While in the beginnings of this hobby there are seemingly trivial considerations that have to be implemented on the model, the theoretical background increases with larger models to quite imposing theoretical frameworks. So there is something for everyone: for the beginner who wants to get a flying experience quickly and also for the advanced modeler who wants to recognize and try out the subtleties (and also nastiness) of aerodynamics and flight mechanics.

Unforgotten and not unmentioned at this point is Rudi Zimmermann, the good soul of the association and permanent contact point in the workshop. He, too, would have his work confirmed with this brochure. Unfortunately, he could not live to see its completion.
Let us consider this documentation as a tribute to the life's work of a recreational modeler. May it delight many readers with suggestions and technical solutions, so that quite a few technology enthusiasts still see model flying as a meaningful leisure activity.

Prof. Dr. Norbert Brückner

Foreword

Schools in Germany do not only offer the regular curriculum. Rather, it is common that in addition to this, students are offered education in areas that might also interest them. Examples include the school choir or playing musical instruments individually or instruction in a technical field. And here we aero modeller have the chance to recruit new blood for our club. Using the example of a cooperation between the Modellfluglub Rossendorf e.V. and a nearby high school in Dresden, this booklet shows that such a cooperation can be also a bridge to the school syllabus as well to small projects in the context of physics and information technology (IT).

The main topic in the first part of the paper is the practical approach to model airplane building; from the simple to the more difficult. Already with the simple models basic characteristics are described, which allow statements about the flight quality later on. Notes on RC-Training will also be included.

Theory is applied within the second part: with the help of the basic properties studied in simple models, further important parameters can be determined and confirmed by simple measurements. Additionally guidelines fort the design of a model are given, including calculation examples on practically applied models. Commercially available motor gliders of different performance classes are recalculated exemplarily regarding both their flight characteristics as well as their motor-propeller configuration.

Thus, this report could offer something new to the student and likewise be useful to the instructor for reference. For both use cases, the manuscript would have been worthwhile.

Hans Langenhagen   Rossendorf, July 2021

Table of Contents

Examples of measurements and calculations

List of symbols

Symbol	Unit	Meaning	page	fig	Eq
A		Aspect ratio	30		5.7
a	m/s^2	acceleration	84	8.2	
ac		Aerodynamic Center			
α $\quad\alpha_w$ $\quad\alpha_{hs}$ $\quad\alpha_A$		Angle of attack $\quad$ of the of wing $\quad$ of the horizontal stabiliser $\quad$ of the wing, taking into account the wing aspect ratio A	25 73 71	5.2 7.7 7.4	7.3
B = m/S$_w$	gm/dm^2	wing load, Tab. 2.1	4		
Beu		corrective factor for calculation auf x$_N$	75 76	7.12	7.5b
b	m	wing span	5	2.2	
C	As	rechargeable battery capacity			
c	mm	airfoil chord; chord length,	25	5.2	
cg		center-of-gravity			
c_d $\quad c_{dp}$ $\quad c_{do}$ $\quad c_{di}$ $\quad c_{dh}$ $\quad c_{dtot}$		Drag coefficient $\quad$ - airfoil drag $\quad$ - airfoil drag minimum $\quad$ - induced drag $\quad$ - harmful drag $\quad$ - of the model	25 30 30 30 32 32	5.2	5.1/2 5.8 5.6c 5.6
c_l		Lift coefficient	25	5.2	5.1/2
c_m		Moment coefficient	75	7.10	
χ_0		Downwash angle Chi	73		7.4a
D		diameter propeller	78 80		7.7 7.10
E		lift -to- drag –ratio E = 1/ε	6		5.5a
ε		drag-to-lift-ratio; ε = 1/E			
EWD	deg	angle of setting	72	7.7	
F $\quad F_L$ $\quad F_D$ $\quad F_W$ $\quad F_T$ $\quad F_C$ $\quad F_{RF}$		Force $\quad$ lift Force $\quad$ drag force $\quad$ weight force $\quad$ thrust $\quad$ centrifugal $\quad$ rolling friction	28 28 34 59 101	5.4 5.4 5.10 6.1 8.23	5.3 5.28 8.19
ϕ		wing dihedral angle	66	6.16b	7.5d

Symbol	Unit	Meaning	page	fig	Eq
g		acceleration of gravity			
γ		angle of fligth path			
γ_c		climb angle p. 36, 37			
γ_d		descent angle p. 28,			
η		flap angle	27	5.3	
		efficiency	48	5.22	
H	cm, inch	pitch	49	5.29	5.23
			78		7.8
I	A	electrical current			
Io	A	constant current (battery)			
Io	A	no-load current (DC motor)			
J		propeller advance ratio, V/(n*D)	53		5.29
F_L, L		Lift			
$F_{air}(\beta)$	N	air force acting on a deflected flap	93	8.15	8.10
L/D		Lift-drag ratio			
l_μ		airfoil chord length	25	5.2	
lv		load factor	59	6.1	
m	kg, gm	mass			
m_F	gm	mass fuselage	63	6.7	
mw	gm	mass wing			
μ		kinematic viscosity			
M	Nm	bending moment	63	6.8	6.7
	Ndm	flap moment Mx2	95	8.19	
N		yawing Moment (about z-axis, positive nose right)			
NP		Neutral Point	75	7.10	
n		rpm (rounds per minute),	47		5.20
		rated rpm : Nenndrehzahl	78		7.7
		angular velocity, speed,			
		revolutions per second or per min			

Symbol	Unit	Meaning	page	fig	Eq
P	W	Power			
P_{el}	W	electric power supplied to the motor			
P_{dis}	W	dissipation - Verlustleistung -			
P_{mech}	W	mechanical power loss f.i. by friction			
P_{sh}	W	mech. power supplied by the motor shaft			
P_{pr}	W	power absorbed by propeller	50	5.33	5.25
P_{out}	W	mech. power, supplied by the propeller			
P_{sc_req}	W	requested power, solar drive	98	8.21	
P_{sc_del}	W	delivered power, solar cells	98	8.21	
Q		angular velocity (pitch rate) about airplane's y-axis			
R		internal resistance of an electric motor	47 81	5.27	7.12
R_i		internal resistance of a recharg. battery	42	5.20	
Re		Reynolds number			
r_h		horizontal	75	7.10	7.5c
r_v		vertical tail moment arm	77		7.5d
ρ	kg/m^3	air density 1.23 kg/m^3	24		5.1/2
R		radius of cylinder			
R		propeller radius	48/9		5.29
RPV		remote piloted vehicle			
R/C		remote control			
S_w	dm^2	Wing planform area	24		5.1/2
SM		Stability Margin	76		7.6a
s_{lo}	m	space at the moment of lift-off	87		8.2
σ_b	N/mm^2	bending stress	63		
σ_{b_perm}	N/mm^2	permitted bending	64		
σ_{ts}	N/mm^2	tensile strength	58		
σ_{ps}	N/mm^2	compressive strength	58		
σ_{bl}	km	breaking length	58		
t_D	sec; hr	discharge time of a rechargeable battery	41	5.18	5.18
t_{lo}	sec	time at the moment of lift-off	87		8.2
T	N	Thrust			
TO		relatively Tolerance, deviation of rate value	91 92		8.7 8.8
v	m/s	velocity	28	5.4	5.3
v_{lo}	m/s	at the moment of lift-off	87		
v_{cruise}	m/s	cruise velocity	83		
v_∞	m/s	free-stream velocity	8	2.6/7	
v_{sr}	m/s	sink rate, rate of descent/sink	28	5.4	5.4
v_{cr}	m/s	climb rate	36	5.13	5.14
v_{pr}	m/s	air column speed behind the propeller	49		5.24

Symbol	Unit	Meaning	page	fig	Eq
V_H		horizontal tail stabilizer volume	75		7.5c
V_V		vertical tail stabilizer volume	77		7.5d
W	N	model weight, $W = mass*g$			
W_{spar}	mm^3	resistance of spar	64	6.10	6.9b
χ		Chi (from „c")	73	7.7	7.4b
x_N		position of Neutral Point model		75	7.5c
ξ		zeta (from „x")	73		7.4b
y		spanwise distance along a wing span from the center			

The start of the offer in the Rossendorf model making workshop, 1 September 2009

Mr. Langenhagen explains the aim of the GT offer: starting with building simple models, we will approach building different remote control models for training purposes. Often we will build from the kit, i.e. many parts are already prefabricated.

Parallel to the construction work, we will also learn about the physics of flight and how to control a model aircraft remotely: on the simulator in the workshop or with the club's own models (using teacher-student remote control technology) in the gym or on the flying field at Weißig.

The founders of the *All-day Program Model Flight*: R. Zimmermann (top right, †18.05.21) and H. Langenhagen. They were supported by K. Wenzel in 2011/13, F. Schade in 2014/16 and A. Scheffler in 2016/19. "Fire missions" were also performed by W. Dienel, KH. Helling, A. Lorenz and M. Müller

1.0 We start building the "Rossendorf light glider", a polystyrene glider.

First we build a polystyrene glider. We can then also test it in the corridor of the clubhouse.
We are Kelvin from class 5.2, Stefan from class 5.3 and Florian from class 7.1. Zacharias from class 5.3 will join us later.

Then we build the balsa glider CANDY, here the individual parts are pre-cut in a Balsa-board

2.0 We build the Balsa-Gliders Candy und Jimmy

Remove the parts from the pre-cut balsa board. They are joined, aligned and glued together as

specified in the building plan.. On the finished model we set the required position of the centre of

gravity with the help of the rocker. The "fine-tuning" is then done during the first gliding flights.. The Candies are ready and tested

Fig 2.1 Packaging of Jimmy.

- Construction kit from Graupner, the balsa parts are pre-cut and easy to break out.
- Mr. Zimmermann explains the individual assembly steps to each of us and we begin with the fuselage gluing.
  The wing transitions: the centre section and the bent end sections are sanded.
- We calculate the centre of the wing in order to find the place for the support board where the wing
  can be fixed symmetrically to the fuselage support board with rubber rings.
- With steel balls in the fuselage-nose we move the C.G. on the position required by the construction plan.
- We check with the C.G. "balance" whether the C.G. is now at the right position.
- We have to estimate the area of the wing. To do this, we look at it as a rectangle,
  measure its span (from one wing tip the other) and Root Chord Length and
  calculate the rectangle; we get a total surface area of 4,85dm^2:

6th October 2008

Candy

$b = 4.8\,dm$

$c = 0.65\,dm$

$S = 2.99\,dm^2$

$m = 68\,gm$

wing load:

$B = \dfrac{m}{S} = \dfrac{68\,gm}{3\,dm^2} \approx 23\,\dfrac{gm}{dm^2}$

Jimmy

$b = 5.7\,dm$

$c = 0.85\,m$

$S = 4.85\,dm^2$

$m = 80\,gm$

wing load:

$B = \dfrac{m}{S} \approx \dfrac{80\,gm}{5\,dm^2} = 16\,\dfrac{gm}{dm^2}$

Parameter of Balsa-Glider: wing span b, wing area S and specific wing mass B = m/S

Here, Mr. Langenhagen has drawn it neatly and also calculated it more precisely:
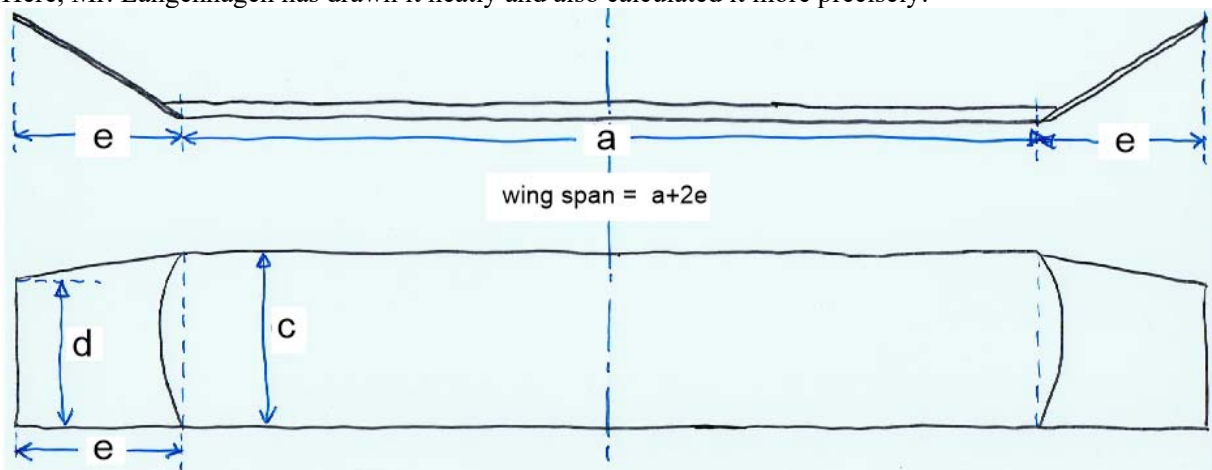

Fig 2.2 We get the wing area by adding the contents of the rectangle and two trapezoids.
Attention: for wings with Dihedral-Angle or "kink ears" the projection on the plane counts.

Wing area JIMMY

wing dimensions $a := 4.05 \, dm$ $e := 0.95 \, dm$ $c := 0.85 \, dm$ $d := 0.7 \, dm$

wing span	$b := a + 2 \cdot e$	$b = 5.95 dm$
wing section rectangular	$Sr := a \cdot c$	$Sr = 3.442 dm^2$
wing section trapezoid	$Str := \dfrac{c + d}{2} \cdot e$	$Str = 0.736 dm^2$
wing area total	$S := Sr + 2 \cdot Str$	$S = 4.915 dm^2$

→ So we've got the surface area quite right with our estimation calculation!

Florian completes the decor, while Stefan already establishes the position of the centre of gravity cg

We summarise the characteristics of the JIMMY:

		Antony_Jimmy	Karl_Jimmy
wing area	S	4,92dm²	4,92dm²
aspect ratio	A	5,95dm/0,85dm = 7	7
modell mass	m	58g	80g
wing load	B	59g/4,9dm² = 11,83 g/dm²	80g/4,9dm² =16,33 g/dm²

Table 2.1 Mass and specific mass per unit area (wing load) of two models related to the wing area.
By the way: The lower the wing loading B, the slower a model can fly; more on this in Chapter 5.2

Afterwards we go to the settlement sports field and do hand launches with the aim of determining the inherent speed and glide ratio of the models.
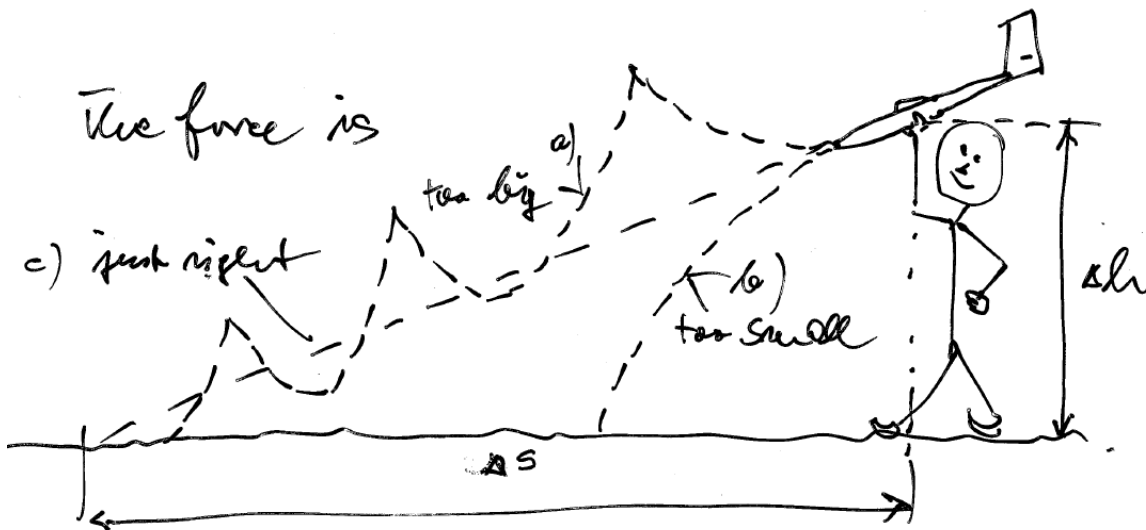
Fig 2.3: Hand launch to determine flight time and distance. The model only comes onto a glide path
(case c), if it is released at the right angle and with precisely dosed force ... this you have
to practise a bit.

Everyone is allowed to throw 5 times. We measure the flight times with the stopwatch and estimate the flight distance Δs by counting steps. Finally, we calculate the average value from the best values of each individual:

	Arne	Justus	Max	Mr. Zimmerm.	average
ejection height/m *)	0,7+1,60 = 2,30	0,7+1,90 = 2,60	0,7+1,65 = 2,35	0,7+1,90 = 2,60	
best Flight distances / m	13	16	14	15	
best Flight times/ s	4	5	4	4	
→aerodyn. quality E **)	13/2,3 =5,7	16/2,60 = 6,15	14/2,35 =5,95	15/2,60 = 5,8	5,9
→path speed v in m/s	13,2/4 = 3,3	16,21/5 = 3,24	14,2/4 = 3,55	15,22/4 = 3,81	3,5
km/h	= 11,9	= 11,7	= 12.8	= 13,7	12,5
→rate of sink v_{sr} in m/s	2,3/4 = 0,58	2,6/5 = 0,52	2,35/4 = 0,59	2,6/ 4 = 0,65	0,59

Table 2.2 Flight parameters of the Jimmy determined from the rough measurements - these are approximate
values

*) We started the models from a small hill, which is about 70 cm high. To this we have to add our personal
starting height, which also depends on how high we hold our arm.
**) the term glide ratio ε is often used, which describes the ratio in relation to 1 - so in the first column this
would read ε = 1: 5,7. More convenient for calculations, however, is the reciprocal value E = 1/ε

But how do the trajectories in figure 2.3 deviate from the glide case "c"?

To answer this question, let us first recall the parachute, which we discussed in the lecture "History and Physics of Aviation" [La16] in connection with Leonardo da Vinci's inventions:

The so-called stationary speed, which in the example shown in Figure 2.4 is about 4m/s, results from the fact that the forces acting on the falling body have "levelled off". The same pointer lengths do not mean that the jumper stops in the air, but that a descent takes place in which the speed no longer changes. We are talking about uniform, unaccelerated movement.
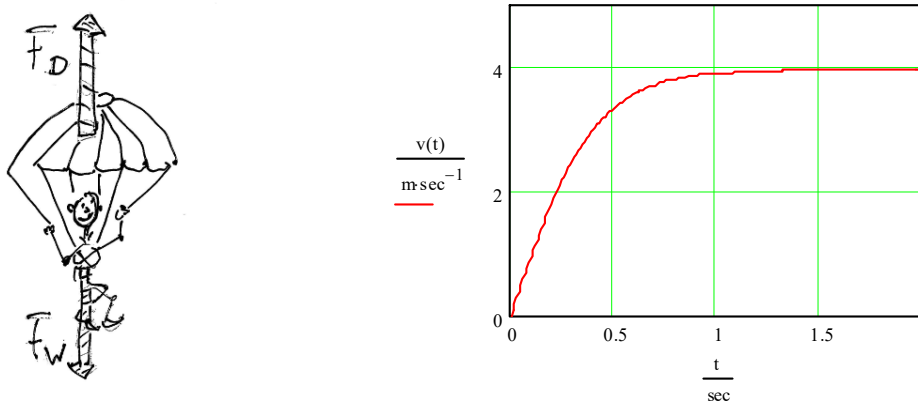
Fig 2.4 In a parachute jump, after a transition phase, the weight force $F_W = m \cdot g$ and the drag force F_D
are in "equilibrium". i.e. equal in magnitude but opposite in direction. The rate of descent,
referred to as sink rate in the following, reaches a stationary value whose magnitude depends on the
mass m and the air drag F_D; the latter is directly proportional to the parachute area S.

Now let's look at the glide of a glider model. Once we have brought it onto the glide path at the "appropriate" speed, a stationary speed will also occur here, i.e. the forces are in equilibrium, Figure 2.5. But which forces are these?
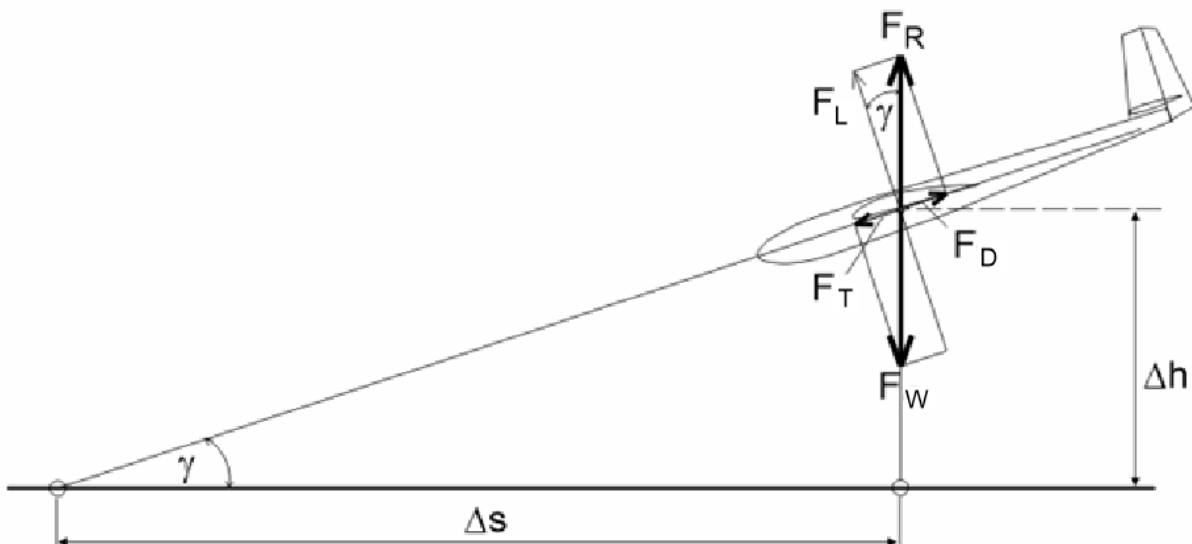

Fig 2.5 Forces during gliding flight of a glider model. More detailed information in section 5.2

We are already familiar with the weight force as the product of mass and acceleration due to gravity from parachute jumps, $F_W = m \cdot g$. Now it is counteracted by a force which is composed of the lift force F_L generated by the aerofoil and the drag force F_D; it is therefore called the resultant force F_R. The (air) resistance force F_D, in turn, is in equilibrium with the propulsion force F_T, which arises because the model glides downwards like a ball on the inclined plane due to gravity.

From the lecture "History and Physics of Aviation" [HisAvi] we know that the lift force on an aircraft arises as a result of its movement through the medium of air. At a sufficiently high speed, a bound vortex forms around the wing, the so-called circulation. This leads to the velocity of the air flowing around the upper surface of the wing becoming greater than that of the aircraft itself. According to Bernoulli, negative pressure develops at high flow velocities and positive pressure at low flow velocities in relation to the more distant medium. The effect of these pressure differences is the lift force F_L.
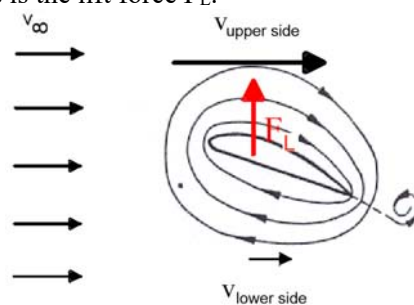

Fig 2.6 On the upper side of the wing, the incoming flow velocity is added to the velocity of the circulation flow. On the underside it is subtracted.

The different flow velocities on the upper and lower wing surface cause a spatial pressure distribution along the airfoil chord $l\mu$ as well as along the span, Figure 2.7. As an approximation, 2/3 of the total lift force of the wing is caused by negative pressure on the upper surface and 1/3 by positive pressure on the lower wing surface.

However, this pressure difference wants to equalise itself, which it finds the opportunity to do at the wingtips. This pressure equalisation is accompanied by a vortex formation behind the wingtips and generates a considerable proportion of the aircraft drag in flight regimes with large angles of attack (thermal gliding, climb and landing approaches of commercial aircraft). However, it is easy to imagine that the greater the span b in relation to the airfoil length $l\mu$, the smaller the effect of this pressure equalisation on flight performance. We will come back to this in chapter 5.

The quantities buoyancy and drag force shown as arrows in figures 2.5 and 2.6 are therefore only an idealisation of the true conditions, but this has the advantage that it can be used to calculate other quantities, such as speed, very easily.
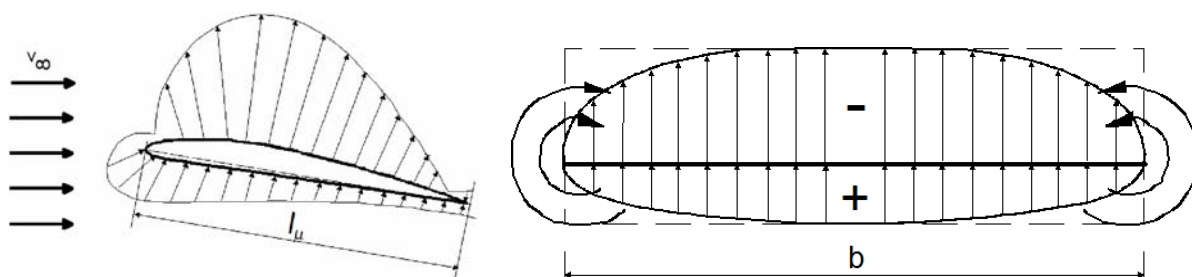

Fig 2.7 As a result of the circulation, there is a spatial pressure distribution around the entire wing. At its ends, there is a flow from areas of higher to lower pressure.

We return to our hand launch experiments according to Figure 2.3. As we will see later, the higher the airspeed, the greater the magnitudes of the air forces F_L and F_D. If we give the model to high an velocity v by applying to much force, the lift force F_L - and thus also the resulting force F_R - increases strongly; figuratively speaking, the length of the force pointer F_R in Fig. 2.5 becomes greater than that of the weight force F_W, since the latter remains constant. The model climbs steeply upwards. During this upward flight, however, the initial energy is consumed, the speed decreases again until it is so small that the circulation collapses and the wing no longer provides lift. The model tilts, picks up speed again and the game begins anew, curve a) in Figure 2.3. If we give the model to low a velocity v by applying to little force, the airfoil does not generate enough lift in the first place, the pointer length of the force F_R remains smaller than that of the weight force F_W, the model does not come onto a glide path, curve b) in Fig. 2.3.

In the evaluation of the glider flights, Table 2.2, we encountered the parameter glide ratio ε or its reciprocal value aerodynamic quality E. It describes the ratio of distance travelled to height loss, E = Δs/Δh. Figure 2.5 shows a correlation between this parameter and the flight path angle γ: the smaller this angle, the better the glide ratio, the greater E. We also see this gliding angle - and thus also E - in the ratio of lift force to drag force: $E = F_L/F_D$.

Because the resulting force FR for small angles $γ \leq 10^0$ is approximately as large as the lift force F_L, i.e. $F_R \approx F_L$, $F_L \approx F_G$ also applies. The lift force is therefore almost as great as the weight force:

$$F_W \approx 65g \cdot 9{,}81 \frac{m}{s^2} = 0{,}64N$$

And because is also E = F_W/F_D, we can now determine the drag force of this small flying model to be

$$F_D \approx \frac{F_W}{E} = \frac{65g}{6} \cdot 9{,}81 \frac{m}{s^2} = 0{,}11N \; .$$

The estimation of these parameters should give us a feeling for the air forces acting on the JIMMY. Table 2.3 shows that the parameters glide ratio, velocity and sink rate are not only parameters of model aircraft. Here are the values for a glider and for a comercial aircraft[1] in comparison to a balsa glider and to a model of a competition class.

We see that the aerodynamic quality of the glider is far superior. This is understandable compared to the commercial aircraft, because gliding is the essential mission for the glider. Economic considerations play no role in its design; it transports a maximum of two people at only moderate speed.

	balsa glider Jimmy	RC soaring RS3, class F3B	glider JANTAR 2B	commercial aircraft A 320
E=1/ε	6	20	48	17
v in m/s	3,5	8	22	72
v_{sr} in m/s	0,6	0.40	0.46	4

Table 2.3: Aerodynamic parameters of differently sized flying machines as they occur in gliding flight, see also Fig. 5.3

by the way: 1m/s = 3,6km/h … you can derive that from the free space right here.

---

[1] In commercial aircraft operations, unpowered flight does not normally occur. Descent flights are always with the engines throttled back, except in the case of engine failure or lack of fuel [HL10].

## 3.0 Motor glider CLIMAXX

Bild 3.1 The packaging view of the Climaxx. All the parts of the kit are CNC-milled and therefore
      worked accurately

- after the rather small flying models, we now dare to build a remote-control flying model
- it will be powered by an electric motor, but should also have good gliding characteristics
- we will hear more about the propulsion system later, for now it is about the
  + <u>construction</u>: it follows the principle of lightweight construction, i.e. the skin (foil) encloses a hollow
    body of low weight with the best possible strength. The fuselage carries the propulsion system and
    the receiver with control devices, some of which are also housed in the wings
  + <u>installation</u>: this is done using the spar/rib/frame/skinning method. Although this method does not
    give the best contour accuracy (interesting for accuracy of the airfoil), it can be mastered by us.
    We will learn more about other construction methods later.

The box is open - can we match all the parts to the construction plan? Reading the drawing is required.

The model construction begins
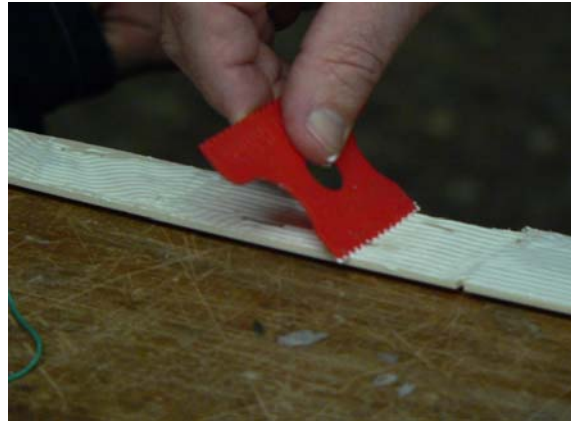
Marco and Paul start with the fuselage. Reinforcement is needed in the front part; we use casein glue (PVA) for these larger gluing areas. The glue can be spread well with a serrated spatula.

Karl and Antony build the wings. We thread the ribs on to the spars and position them over the building plan. The supervisor pins them to the spars, leading and trailing edge with superglue.

Continuing construction Climaxx, wings

- the wing will consist of 2 centre sections and one "ear" each. We build these 4 wing parts over a blank copy, which is protected with a foil. When they are ready, one ear and one centre glued together to form half wings. Only for flight do you put the two halves together and and screw them to the fuselage.
- first, the long balsa ribs are threaded over the spars, inserted into the end rail and aligned then tacked with super glue. When building the centre sections, it is necessary to place the supplied 3x20 strip at the ends of the ribs; this gives the wing profile its planned camber. After gluing in the leading edge strip, also a carbon rod, we can insert the half ribs. Because the wing ears are trapezoidal, we must pay attention to the correct order of the ribs, which are of different lengths.
  When the wing "ear" and the middle section have been glued together, we have to re-glue all the parts once again: the wood-wood joints with casein glue, the ribs-carbon spar joints with UHU-hard.
- The root ribs must be glued in slightly off plumb so that the desired dihedral is achieved when the wing parts are joined. That is why Mr Zimmermann glues them on himself with the help of an angle gauge.

But why does the wing need such a thick tube as the main spar?

In figure 2.5 we had shown the forces acting on the model simplified as pointers, which all act at the centre of gravity. However, as already explained in Figure 2.7 the lift and drag[2] forces are distributed over the entire wing surface due to the circulation flow around the wing along the span. The wing must absorb these forces and must not break even in the maximum load case.
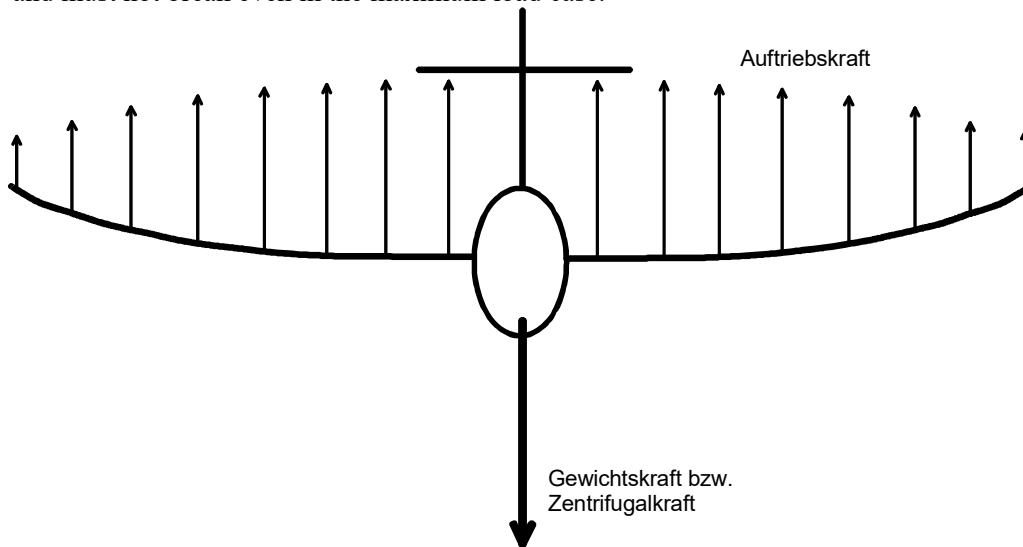
Auftriebskraft

Gewichtskraft bzw.
Zentrifugalkraft

Fig. 3.2 In normal flight the weight force acts on the wing. At the moment of interception from a dive a multiple of the (fuselage) weight force acts on the wing. Especially at the point where the wing is attached to the fuselage, a high bending moment occurs. The main spar must resist this, it must not break. In chapter 6 / Strength we learn how to calculate the necessary dimensioning.
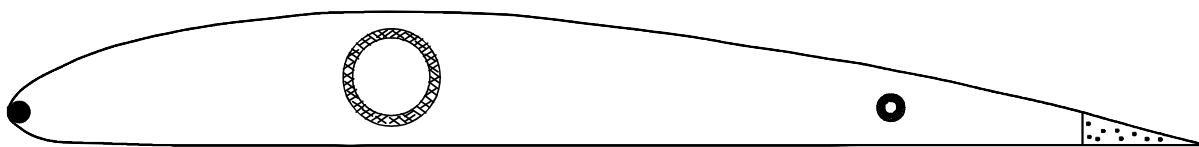
Fig. 3.3 The main spar of a wing can be designed in different ways, here main and auxiliary spar tubes are made of Carbon fibre. Tubular spars add torsional rigidity.
A carbon fibre bar is also used on the wing leading edge, while the trailing edge is made of balsa. However, the leading and trailing edge do not contribute to the strength.

However, the wing is also loaded for twisting: At high airspeed, as can occur in dive, the point of attack of the lift shifts towards the trailing edge and tries to twist the trailing edge of the airfoil upwards. If the wing is "soft" in its structure, it follows this force effect to a certain degree, flaps back again, is bent upwards again, flaps back again ... a "flutter fall" is the inevitable consequence, from which the model can no longer be intercepted.

In many cases it has led to the destruction of a model when the pilot tried to bring it back from high altitude by nosediving. We achieve a safe descent from thermals without increasing speed by reducing lift and increasing drag, as is possible, for example, by extending ailerons upwards on both sides.

---

[2] Since the drag force is only about 1/10 of the lift force, we neglect its effect here. Also, for the sake of clarity, the pressure force acting on the underside is omitted in the sketch.

Continuing construction Climaxx, wing and fuselage

Now the "ear" and half of the centre section must be joined together. The two carbon moulded parts on the main spars ensure the exact dihedral angle and a firm connection. Therefore these are glued with 2-component-glue (Epoxy) by the exercise instructor.

After the fuselage has received its frame and servo mounts, We glue balsa panels cross-grained to the underside of the fuselage. It then looks like this ↑
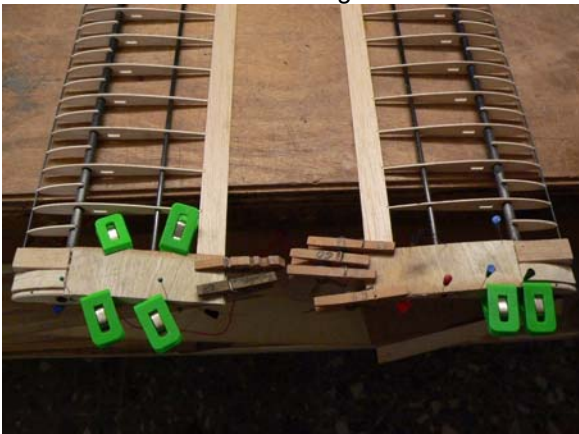
To make it easier to handle later when assembling the wing at the airfield, we applied balsa blocks and plywood sheets (0.6mm thick) to the wing root. When sanding the blocks, the nose area must often be checked for contour accuracy.

Which glue for which connection?

Depending on the type of bonding point, different glues are used for the shell, see Table 3.1. For example, tack bonding with superglue is practical because the steps can be carried out quickly one after the other due to the short curing time. If the adhesive is sprayed with the so-called "activator", the curing process is even accelerated. Another advantage of this adhesive is that it creeps between the bonding surfaces; the glue gaps

should be as thin as possible. But be careful: do not touch it with your fingers! **In the mfcR club workshop, young people up to the age of 16 are only allowed to glue with casein glue!** UHU-hart and casein glue take a little longer to cure, we use it to glue a plywood surface to a balsa slat, for example, or to re-glue the staples made with superglue. It is also very good for thickening strip-rib joints with glue plugs. 2-component adhesives are used for high-strength joints, whereby 5-minute epoxy is usually suitable for our model applications. The following applies to all parts to be bonded: the surfaces must be clean, dry and free of oil, grease and dust!

	superglue	solvent glue	casein glue (PVA)	2-component glue
trade name		UHU-hart, Duosan	Ponal, UHU Coll	5Minute-Epoxy
glues well	wood ⇔ wood wood ⇔ metal wood ⇔ plastics	wood ⇔ wood wood ⇔ plastics (Ribs on spar)	wood ⇔ wood	wood ⇔ wood wood ⇔ metal wood ⇔ plastics plastics ⇔ plastics
apply for	- lightly loaded bonds - pinning parts - difficult to access places - time-critical bondings (airfield repairs)	- lightly loaded bonds - small-area bondings	- loaded bonds - large-area bondings	- highly stressed bondings - smaller bonding areas
processing time	1s	2Min	10Min	20Min
gluing time	10s	30Min	1h	
Further processing possible after	1Min	2h	10h	24h
Manufacturing Base	Cyanoacrylsäure	Cellulose-Nitrat, dissolved in ethyl ethanoate	**P**oly**V**inyl**AC**etat, distributed in aqueous solution	
Hardens as a result of	chemical reaction (Polymerisation), start by moisture	Evaporation of the solvent	Evaporation of the water	chemical reaction (Polymerisation) after contact of resin and hardener
constancy	not moisture or temperature stable	insensitive to water	stable to moisture and temperature	stable to moisture and temperature

Table 3.1 Model-making glue used so far; which is suitable for which connection?

Wing, fuselage and tailplane covering with heat shrink film

The ribs were initially attached to the spars with superglue. Now we glue these areas with UHU hard

First "ironing attempts" - here on the rudder blades.

Tail unit construction

- the tailplane is designed as a V-tail, it consists of 2 surfaces (instead of 3 for the cruciform tailplane)
- first the rudders have to be attached to the tail planes by means of hinges ... this work
  Mr. Zimmermann prefers to do it himself. Then we glue the two halves together using the moulded
  piece and then fit the complete tailplane into the fuselage.

The V-tail is glued together. It must now be fitted

into the recess at the rear of the fuselage.

Now we add plenty of white glue to the gluing surfaces and finally we have to remeasure and align,

so that it "fits" in every direction.

Here are some remaining glues at the wing root

4.0 We control club models

At the club's model airfield near Weißig, the remote-control instructors A. Lorenz (li) und H. Langen-hagen await us with two different-sized powered gliders. We can send them via transmitters around in the sky. That makes fun!

At the beginning it is about flying at an altitude of aprox. 100m along the field edge, flying routes each of which reverses direction with a 180^0 turn.

With the smaller model we are allowed to try a landing. If we land too far away, we have to walk a little longer.

4.1 Longitudinal control
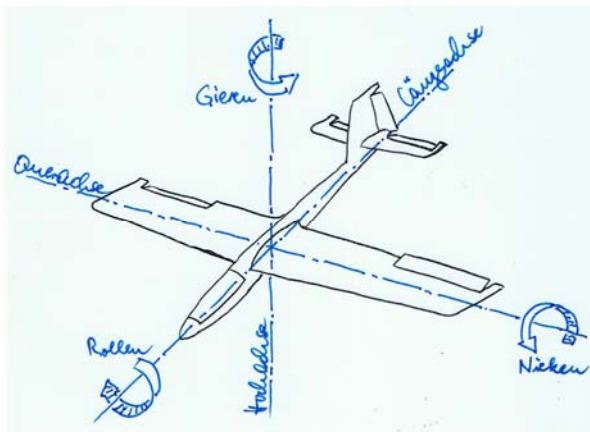
Fig. 4.1 You can imagine 3 axes that meet at the center of gravity. Using the control surfaces, we can turn the model around these axes in flight

A body in space always rotates around its center of gravity. This is also the case with our flight model. With the rudder deflections shown in Figure 4.1 it yaws about the vertical axis (rudder) and rolls around the longitudinal axis (aileron) into a left turn, and it nods downward around the lateral axis. Together this would result in a downward spiral trajectory. The three virtual axes intersect at the center of gravity cg of the model.

Already during the assembly of the balsa glider Jimmy, fig. 2.1, we promoted its position on the longitudinal axis by steel balls in the fuselage nose to the position indicated in the plan. In this model, it is located about 37mm behind the leading edge of wing.

In our remote control flights, we initiated the turns with the right stick and also released it at the end of the desired turn. The aileron on our club models is on this stick. Depending on your instructor's judgment, you may have been allowed to use the left stick to operate the elevator. While the effect of aileron and rudder is plausible in figure 4.1, we still need some knowledge about lift for the effect of elevator, figure 4.2.
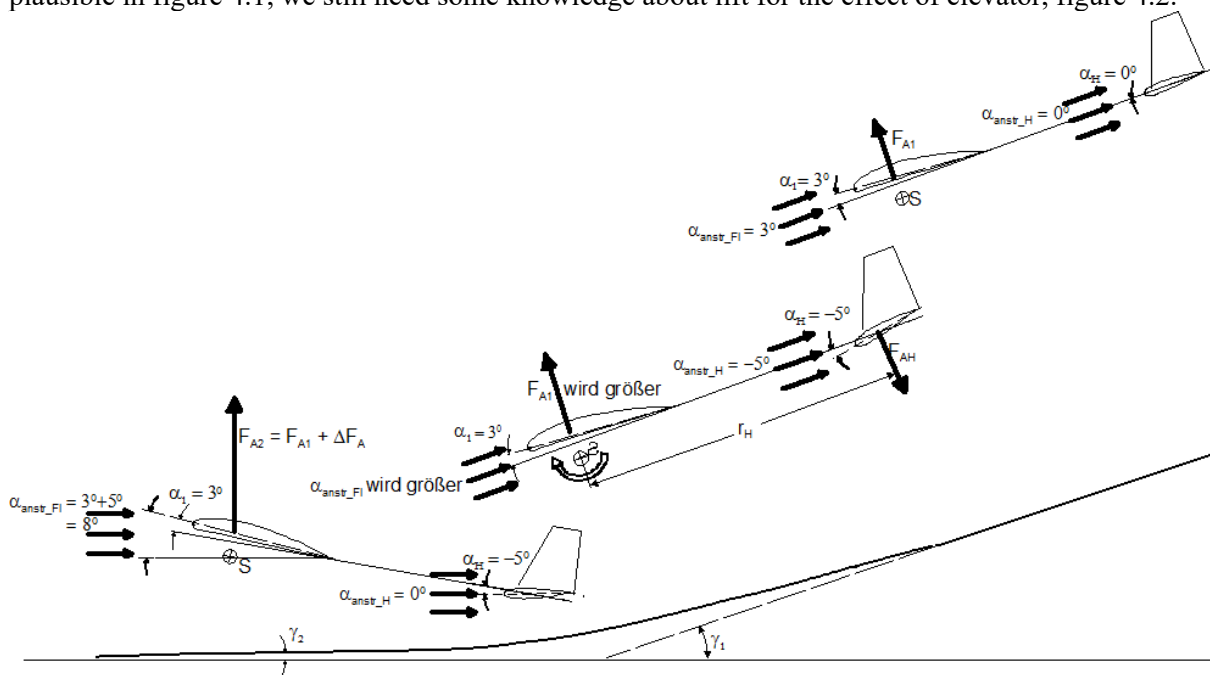
Fig. 4.2 Interception arc during landing. With "pull elevator" the down force F_{AH} causes a rotation around the center of gravity via the lever arm r_H. This continues until the angle of attack of the horizontal stabilizer $\alpha_{anstr\_H} = 0^0$ and thus its downforce has become zero. In the example shown, however, this causes the wing angle of attack to reach $\alpha_{anstr\_Fl} = 8^0$, the wing lift force increases, the model flies more slowly and touches down gently.

From the explanation for the development of the lift force F_L Figure 2.6, it is known that its magnitude depends on the inflow velocity v_{inflow}. However, the angle α at which the airfoil is approached also has an influence. Aerodynamicists gain knowledge about this in the wind tunnel, see Chapter 5 and here Figures 5.1a and b. Only this much should be said in advance: over a certain angle of attack range, the lift approximately follows a straight line; we will limit ourselves to this range here.

For the exemplary assumed angles of attack in figure 4.2, the top situation shows the model in stationary glide flight. With α_{hs} = 0deg and because of the symmetrical airfoil, the horizontal tail does not generate any lift, see figure 5.2a), top characteristic 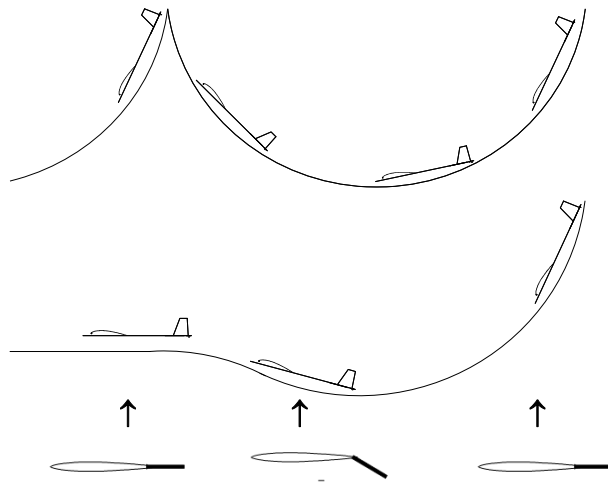curve. With the elevator angle in the middle situation, here exemplarily α_{hs} - 5deg, this produces a down force, see figure 5.2a, left straight line branch. This causes the model to rotate around the centre of gravity in such a way that it straightens up. As a result increases the wing angle of attack, the lift force on the wing increases up to the (practically impossible) limit case $F_R = F_L$, see figure 5.2b. The glide angle γ decreases, thus also the propulsive force F_T in figure 2.5 and the model lands at lower speed.

Fig. 4.3 A brief deflection at the elevator helps to bring the model back into normal flight

Figure 4.3, on the other hand, shows schematically how a critical situation, in which the longitudenal stability of the model can no longer do anything, can be remedied with a short depth rudder deflection. To do this, you have to catch the

right moment or the right flight path point: immediately after flying through the path minimum, you have to push down and the model resumes its glide path.

4.2 <u>Curve control</u>

For a properly steered turn, we operate all 3 rudders:
* with an aileron deflection we first "roll" the model around the longitudinal axis into an inclined position of our imagination;
*At the same time as the model takes up the bank angle, we add elevator "pull". This prevents the model from falling into a downward spiral. The greater the bank, the faster the model circles and the greater our elevator deflection must be so that it flies almost on a horizontal level;
*At the same time as the aileron deflection, we also add a slight rudder deflection, which supports the movement around the vertical axis, the yaw, according to the intended curve. Frequently experienced pilots often automate this process by adding a rudder deflection to the aileron deflection by programming their remote control system.

But before we fly full circles, we first practise corresponding partial circles: 90deg turns and 180deg turns. Already with the 90deg turn, we will notice that the recovery of the turn, i.e. the roll back from the banked position to the horizontal wing position, makes the model suddenly rise. This is a result of speed increase: Despite all efforts to pull the elevator, we cannot prevent a model from sinking slightly in the curve and therefore accelerating in its orbital speed. … and this excess speed is converted by each model into additional lift and thus into a short upward movement as soon as it returns to normal flight attitude with the wings horizontal. If you are not careful, this upward movement can even lead to a stall with subsequent "pumping", see figure 4.3, and it takes effort to return the model to normal flight. The remedy for this is again depth rudder deflection when the model comes out of the turn and starts to climb away..

However, explanations alone do not help. Quote Fritz Seidler for man-carrying flying [Seid62b]: "As in all fields, theory and practice must complement each other in flying. Neither the one who overemphasises theory nor the one who wants to do without it will achieve success."

Rudder adjustments on the tail unit
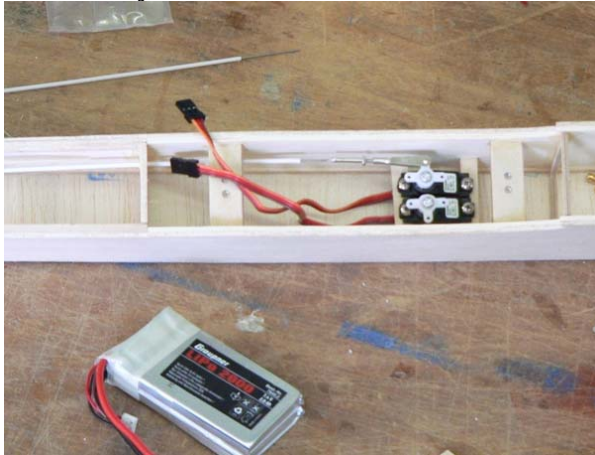
Now the positions Servo zero and Rudder zero must be brought into line. To do this we provisionally hang the Bowden cable in the servo and cut it back to the necessary length.
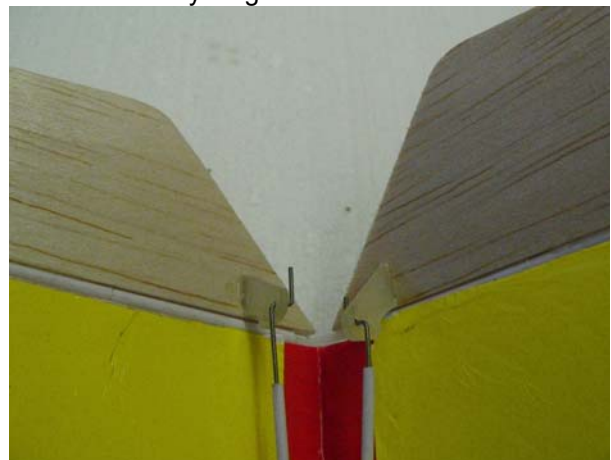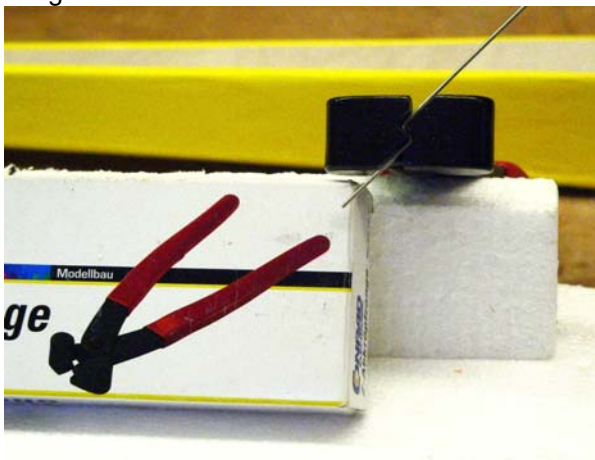
On the tail side we bend a "Z" into the steel wire with special pliers and hook it into the rudder horn.


On the servo side, the steel wire is tinned and soldered into the sleeve of the rudder clip.
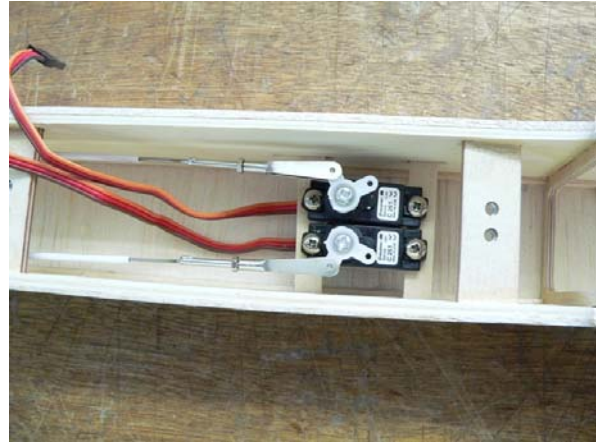
Then we set the appropriate length on the threaded rod of the rudder clip. The test shows: for the rudder deflections to be the same, the servo lever must be in the zero position at a different angle from 90 deg. We also cut off the unused levers so that they do not interfere with each other.

Continuing with the fuselage
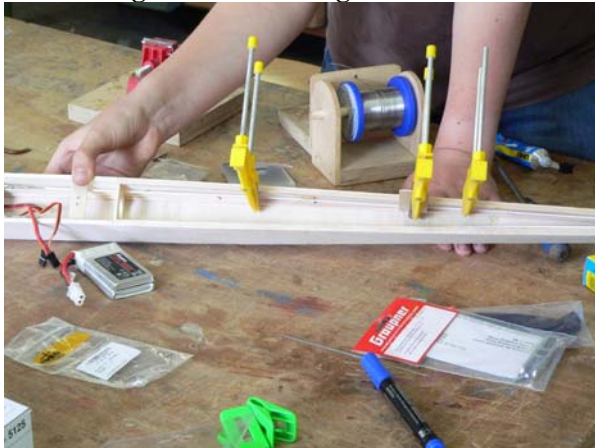
Now we glue the Bowden cables in several places in the fuselage and close it with balsa plates.
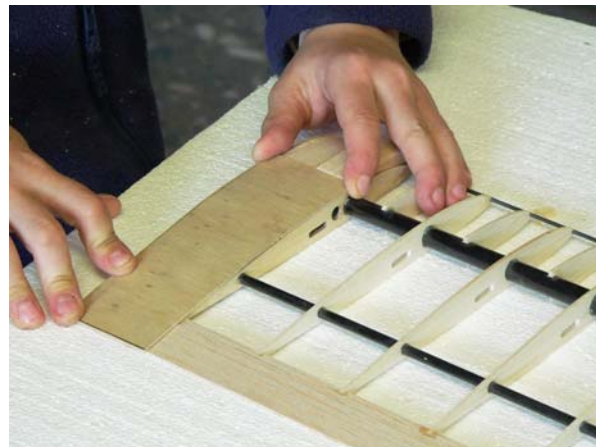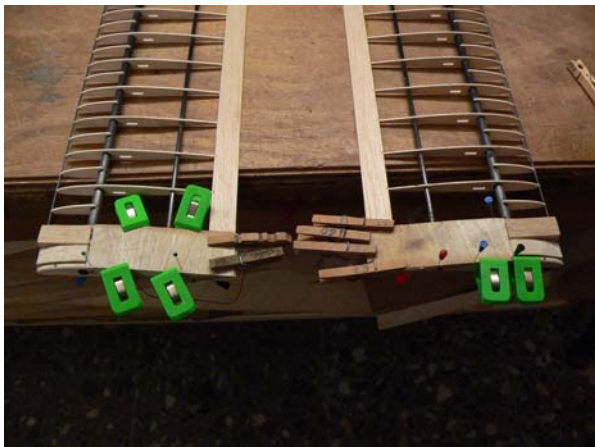
Although not planned in the construction plan, but nevertheless important: we reinforce the root area of the wing between the leading edge and the main spar with balsa blocks (not yet sanded to rib contour in the photos), between the main spar and the trailing edge with thin plywood planking. This gives more "grip-strength" for mounting and dismounting the model on the airfield.

Covering with iron-on foil

Now the wing is covered. This should form the airfoil shape given by the ribs along the entire span. The manufacturer has provided heat shrink film; it is coated on one side with a hot glue which melts and sticks when ironed on. First of all, the foil is only "tacked" to the end strip and ribs, then also to the leading edge strip ...

... starting at the bottom. Then the "smoothing" (the stretching of the foil) takes place, while the iron is slowly passed over the entire wing half.

The aileron is attached with adhesive tape.

The tail unit and the fuselage are also ironed

The temperature of the electric iron can be adjusted. First, we attach the film at about 120 deg celsius. If then want to tighten larger areas, we can increase to 140 deg Celsius.

Now we build a transport box

As soon as the model enters the "almost-ready" stage, a storage or transport box becomes necessary. It is made of corrugated cardboard. The dimensions are the result of considerations regarding the practical stacking of the model components.

The interior of the crate must be equipped in such a way, that the model is not damaged by rough transport procedures (falling over, dropping, etc.)

The box contains guide elements for threading the wing and fuselage made of impact-resistant EPP

The side walls of the fuselage tunnel are made of smooth cardboard so that the propeller does not get st[...]
when it is pulled out. The wings also get a (white) cover.

Closed fuselage tunnel, brackets for the wings. Now only the closing flap is missing

... and this is what the finished model looks like now!!!

5.0 What we can work out with the air forces

5.1 Calculation with coefficients

In Fig. 2.5 we learned about the forces acting on the flight model in stationary, i.e. in unaccelerated glide flight. Using a simple estimation for the aerodynamic quality E from flight altitude and flight distance, see Table 2.2, we were even able to make statements about the magnitude of the lift force F_L ≈ 0.64N and drag force F_D ≈ 0.11N acting on the model Jimmy. We can see that the drag force with F_D = F_L/E ≈ 0.64N/6 is much smaller than the lift force. This is just as well, because if this value were larger, E would be smaller and our Jimmy would not have flown so far at all.

But can the quantities F_L, F_D be obtained without flight measurements? Otto LILIENTHAL already made experiments with a circular run, Figure 5.1a. Later, wind tunnels were built in which airfoil models were installed and the forces lift and drag could be measured depending on the angle of attack α, Figure 5.1b.
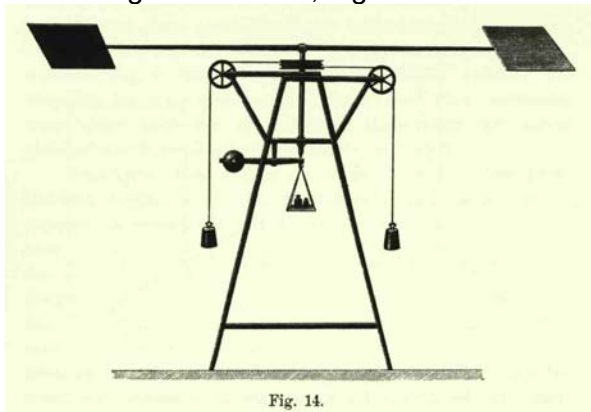

FIG. 5.1a: Roundabout of LILIENTHAL in 1873. The weights help the rotational movement; depending on the angle of attack α, the resulting lift force F_A can be measured with the help of the centrally located balance [Böl90].
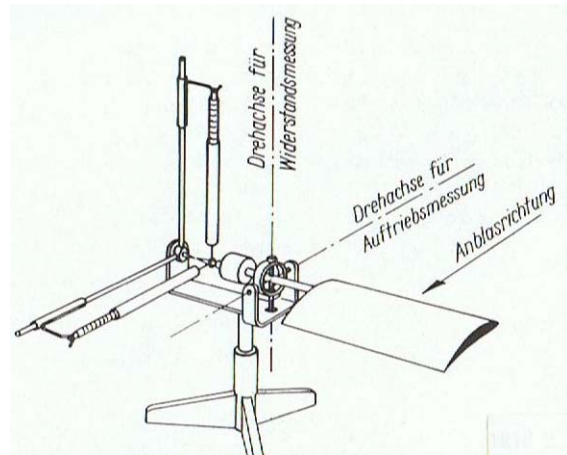
FIG. 5.1b: Air force measurement on the airfoil model mounted in the wind tunnel [SLZ77]. The wing position is maintained here by control, the measured value is generated via the force-deflection which is proportional of the balances (compensation principle).

However, it was soon recognized that the measurement results depend not only on the angle of attack and the airfoil shape flowing around the surface, but also on the surface size S_W and the inflow velocity v. For this reason, the dimensionless coefficients c_l for the lift coefficient and c_d for the drag coefficient were introduced, which the wind tunnel engineers determine from the force measurements. Conversely, every user can now calculate the forces to be expected for his aircraft or model aircraft on the basis of the measured coefficients [BB14].

$$F_L = \frac{\rho}{2} \cdot v^2 \cdot S \cdot c_l \tag{5.1}$$

und

$$F_D = \frac{\rho}{2} \cdot v^2 \cdot S \cdot c_d \tag{5.2}$$

In this

v : Air velocity (m/s)
ρ : Air density, ρ_{air} ≈ 1.23 kg/m^3 bei ϑ = 15^{0}C
S : Projection of the washed around area (m^2)
c_l : Lift coefficient of the surfae
c_d : Drag coefficient of the surfae

Results of such measurements for the coefficients on two airfoils are shown in Figures 5.2-a) and b). The difference between the two airfoils is the camber of the centre line: the NACA0012 has the camber f = 0%, the CLARK Y those of f = 3.6%. Both are the same thickness, d = 12%.
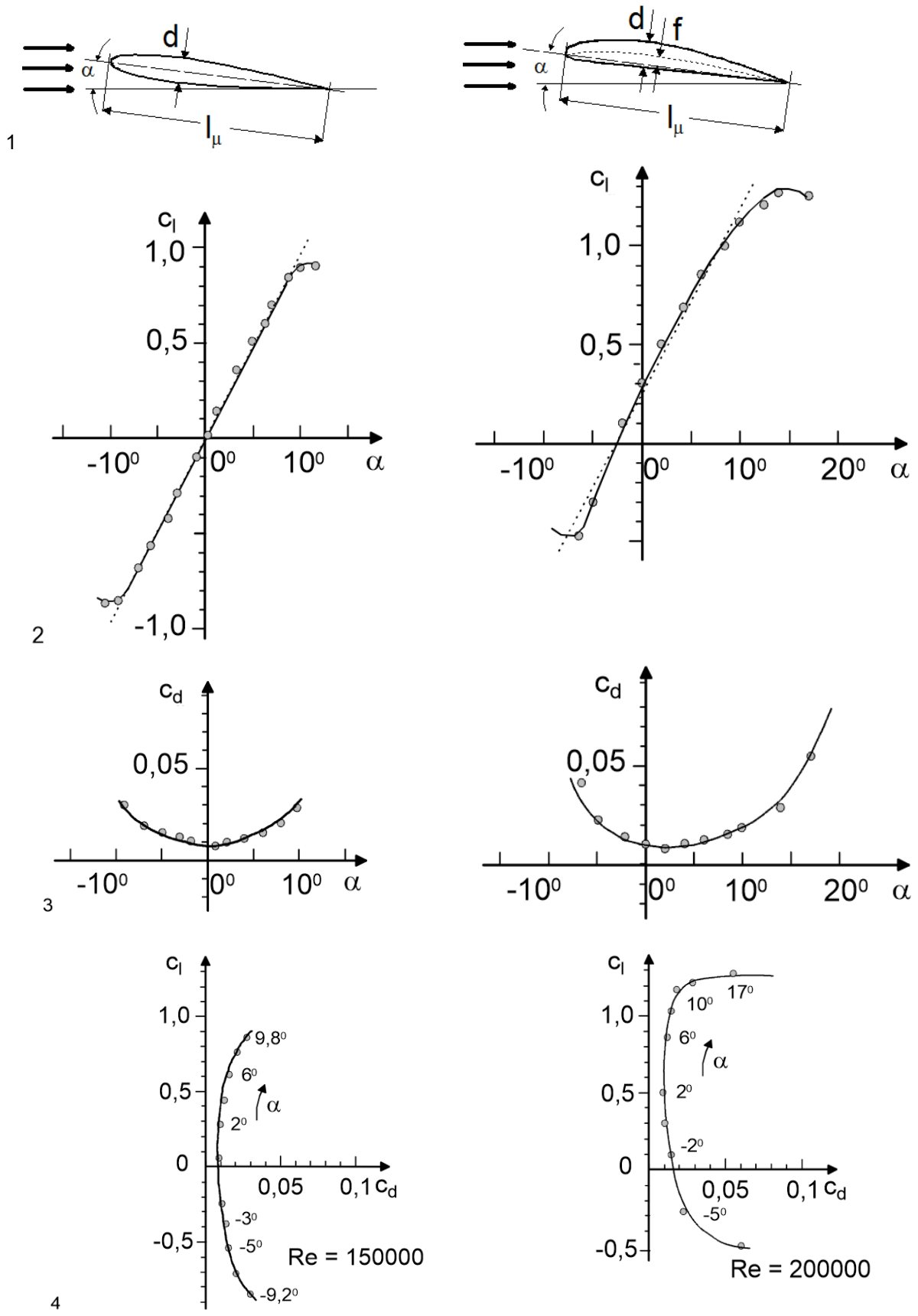
FIG. 5.2: The measured values of two airfoils in comparison [A80]
a) symmetrical: NACA 0012, $d/l_\mu = 0,12$; $f/l_\mu = 0$ b) cambered: Clark Y, $d/l_\mu = 0,12$; $f/l_\mu = 0,036$
We first look at diagram line_2. The course of the lift coefficient c_l over the angle of attack α resembles a straight line within a certain angle of attack range; better in the case of the symmetrical

airfoil, somewhat worse in the case of the curved (also called: asymmetrical) airfoil. With both, however, c_l does not grow arbitrarily far. Above a certain angular value, it even becomes smaller again.

It is also noticeable that the characteristic curve of the cambered airfoil is shifted towards higher c_l values; here, higher lift coefficients c_{l_max} can therefore be achieved with larger angles of attack than with a symmetrical profile.

The course of the drag coefficient, diagram line_3 over α, rather resembles a quadratic function. In the case of the symmetrical profile it reaches its minimum at $\alpha = 0$deg, in the case of the cambered airfoil at a somewhat more positive angle of attack, $\alpha = 2$deg. In both cases, however, the drag coefficient is small with $c_d \leq 0.03$ compared to $c_{l\_max} \approx 1$ in the angle of greatest lift.

The unification of lift and drag coefficient diagrams into a polar diagram with the angle of attack α as a running variable (line_4) also goes back to LILIENTHAL. We will show later how useful this representation is.

But what can we do with such diagram values? Let us first look at some examples of the maximum lift coefficient c_{l_max}.

Example 5.1 (see also pictures 5.3, 5.7 and 6.18)
a) The wing area of the slowflyer RL1 built of foam polystyrene is $S_f = 17{,}8$dm^2 , its mass is m = 140g. It flies (in cruise flight) at a speed of $v \approx 5$m/s fast. With what lift coefficient c_l does the model fly? From Eq(5.1) it follows with $F_L = m*g$

$$c_l = \frac{m \cdot g}{\frac{\rho}{2} \cdot v^2 \cdot S_f}$$

One calculates $c_l = 0.14$kg$*9.81*$m$*$s^{-2}/[$(\rho/2)*v^2*S_F$] = 1,37kgm$*$s^{-2}/[$0{,}5*1{,}23$kg$*$m$^{-3}*(5$m$*$s$^{-1})^2*0{,}178$m^2] = 0,5

b) The performance glider model RS3 developed in the Modellflugclub Rossendorf e.V. has the wing area $S_f = 68$dm* and the mass m = 2,4kg. During the test flights the following values were determined by on-board measurements [JW04]: v = 9m/s, E = 22. With which lift coefficient c_l did the model fly?
One calculates $c_l = 2{,}4$kg$*9.81*$m$*$s^{-2}/[$(\rho/2)*v^2*S_f$] = 23,54kgm$*$s^{-2}/[$0{,}5*1{,}23$kg$*$m$^{-3}*(9$m$*$s$^{-1})^2*0{,}68$m^2] = 0,69
Although we do not (yet) know the c_l curves of the installed airfoil in cases a,b, the c_l values seem plausible when compared with the diagrams Figure 5.2.
c) According to the data sheet [Jant78] the performance sailplane JANTAR 2b, first flight 1977, has the wing area $S_f = 14.25$m^2. The specific mass of the wing can be adjusted from B = 30.3kg/m^2 to 45.5kg/m^2 via the water ballast which can be carried along. The minimum permitted (stall) speed for $B_{max} = 45.5$kg/m^2 is vmin = 80km/h = 22.2m/s. What is the lift coefficient c_{l_max} at this speed?

$$c_{l\_max} = B_{max} \cdot \frac{g}{\frac{\rho}{2} \cdot v^2}$$

Mit $B_{max} = 45{,}5$kg/m^2 und g/[$(\rho/2)*v^2$] = 9,81$*$m$*$s^{-2}/[$0{,}5*1{,}23*$kg$*$m$^{-3}*(22{,}2*$m$*$s$^{-1})^2$] = 0,052 wird c_{amax}= 1,47. However, this lift coefficient is already slightly above the lift curves shown in diagram line_2.

d) At ICAO standard atmosphere: h = sea level; $\theta = 15$degC; p = 1013.25hPa; $\rightarrow \rho = 1.225$kg/m^3 the Airbus A320 needs a speed of $v_{lift} = 270$km/h = 75m/s for takeoff with maximum mass $m_{max} = 77000$kg. Its wing area is $S_f = 122.6$m^2 [A320_a] to [A320_c]. What lift coefficient c_{l_max} must the airfoil provide during lift-off, and what lift coefficient c_{a_min} is required during cruise flight at 10km altitude ($\rho = 0.41$ kg/m^3) with $v_{cruise} = 900$km/h = 250m/s?
The calculation results in $c_{l\_max} = 1.78$ for lift-off; $c_{l\_cruise} = 0.48$ for cruise flight.

The examples show that the maximum achievable lift coefficients of $c_{l\_max} = 1.47$ (Jantar) and 1.78 (A320) far exceed the maximum values shown in Fig. 5.2a), b). In practice, this is achieved by the fact that the camber of the airfoil and, in some cases, its wing area can be increased during flight, Fig 5.3
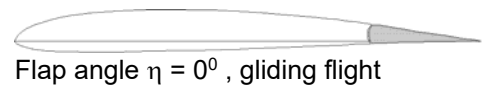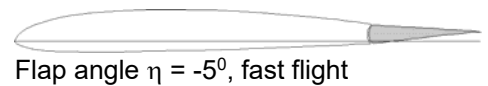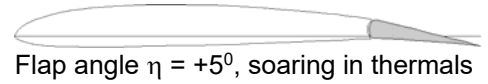
Aircraft	Airfoil geometry	c_l at v
Slowflyer RL1	classic rigid airfoil (Gö 417a) with high camber f = 5,8%	0,5 5m/s
Gliding model RS3	Flap angle η = 0⁰ , gliding flight Flap angle η = +5⁰, soaring in thermals Flap angle η = -5⁰, fast flight	0,69 9m/s
Glider Jantar 2b	Flap angle η = 0⁰ , gliding flight	0,86 29m/s
	Flap angle η = +16⁰, soaring in thermals	1,47 22m/s
	Flap angle η = -12⁰, fast flight	0,15 70m/s
Commercial aircraft A320	Slat and Flap retracted, cruise flight	cruise 0,48 250m/s
	Slat & Flap extended, takeoff & landing	take of 1,78 75m/s landing 1,92 72m/s
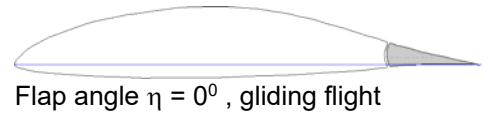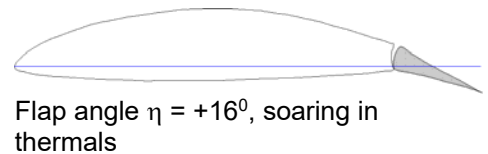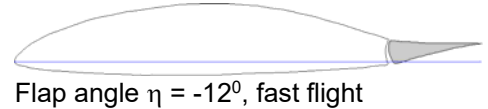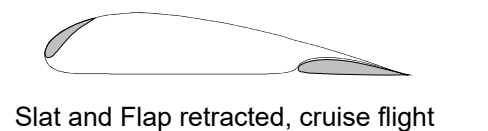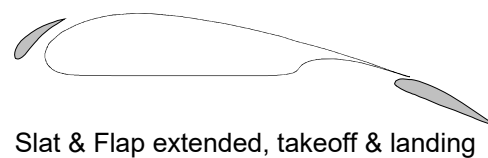
Fig. 5.3: Variable airfoil geometry and its effect on the lift coefficient

In specific cases, the following procedures are used for this purpose:
- a flap adjustable in its angle at the end of the airfoil causes an increase in camber or a camber reduction, see RS3 and JANTAR 2b;
- A flap at the end of the airfoil that can be extended downward and backward (fowler flap) leads to an increase in camber and a lengthening of the Airfoil chord, it also increases the lift area, see A320;
- the retractable leading edge flap (slat) prevents stall on the wing at high angles of attack by supplying high-energy air, see A320.

In the literature [Neu67] it is stated that lift coefficients up to $c_{l\_max} = 3.6$ can be achieved by combining slats and Fowler flaps.

In the field of model flight, however, only deflectable flaps have been used so far; there are also measurement results for them [A80], [Se89]. The flaps are used in soaring flight models (class F3J, example model type RS3), for which slow flight with the smallest possible curve radii is desired when circling in thermals. In the "royal class" F3B of RC gliding, on the other hand, a model must also complete the disciplines of cross-country flight and speed flight in addition to thermal flight. We have already seen from the example of A320 cruise flight that for high speeds only a small lift coefficient ca (i.e. a small camber) is necessary, because in the product equation Eq. 5.1 for FA then the speed v with its quadratic influence dominates. This is the reason why in F3B models "fast" airfoils (those with low camber) are built in as far as possible, which can then be induced to fly slowly by a positive camber.

It is possible that slats are also used in scale modeling (where lifelike reproduction is important); however, nothing is known about measurement results in the Reynolds number range of model flying.

5.2 The stationary flight states

Let's now take a closer look at the forces acting on the model/airplane in the flight conditions *glide*, *level flight*, *climb*. We will see that we can do even more with the lift and drag coefficients c_l, c_d.
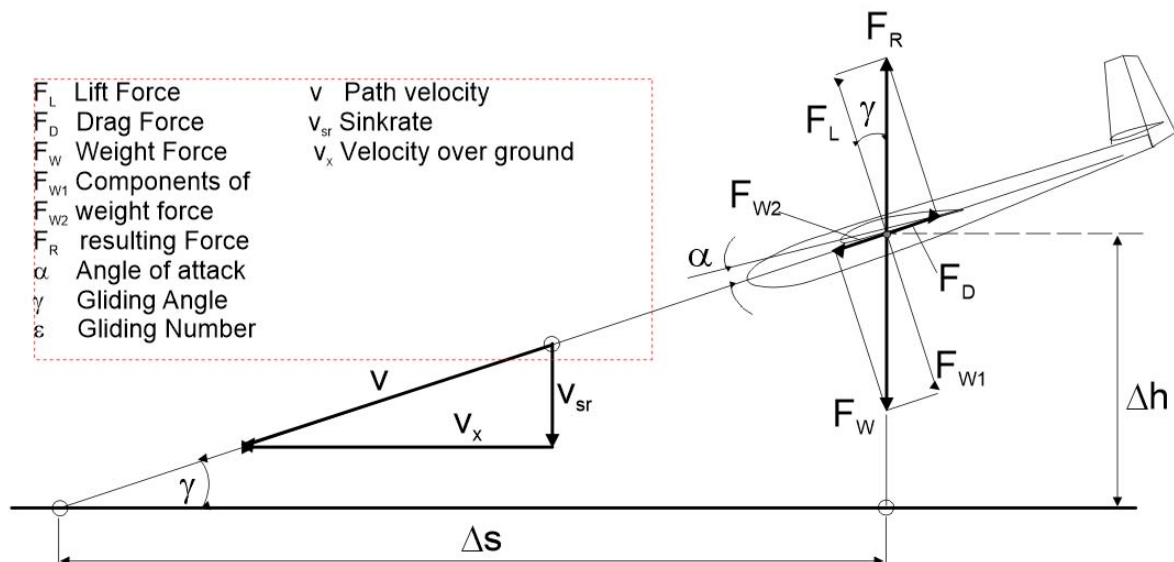

5.2-1 Gleitflug

Fig 5.4: Forces and speeds in unaccelerated gliding flight. The forces act at the centre of gravity of the model. The weight force F_W can be decomposed into the components $F_{W1} = F_W*\cos(\gamma)$ and $F_{W2} = F_W*\sin(\gamma)$. The path velocity v can be decomposed into $v_{sr} = v*\sin(\gamma)$ and $v_x = v*\cos(\gamma)$

The aim of our considerations is to obtain information on the path speed v and the sink rate v_{sr} of the model. For this purpose, we assume that the forces act at the centre of gravity.

A model without propulsion flies from an altitude Δh with a glide angle $\gamma > 0$ deg, i.e. with a constant loss of altitude over a distance Δs, Figure 5.4. It is driven by the thrust force $F_{W2} = F_W * \sin(\gamma)$, a component of the omnipresent weight force F_W. We can already see from this that a glide angle $\gamma = 0$ deg is not possible in propulsionless flight: because $\sin(\gamma=0) = 0$, the propulsive force would also be missing due to $F_{W2} = F_W * \sin(\gamma=0) = 0$.

The forces are in equilibrium, $F_L = F_{W1}$, $F_W = F_{W2}$, $F_R = F_W$. For the upper triangle of forces we apply the Pythagorean theorem:

$$F_R = F_W = \sqrt{F_L^2 + F_D^2}$$

If we use the relationships for lift and drag force according to equations (5.1) and (5.2), we can calculate the speed at which the model flies on its inclined path in unaccelerated glide flight:

$$v = \sqrt{\frac{m \cdot g}{S_w \cdot \frac{\rho}{2}} \cdot \frac{1}{\sqrt{c_l^2 + c_d^2}}} \tag{5.3}$$

But this also gives us an explanation for the "correct" use of force during the hand launch of our balsa glider JIMMY via a formula: due to its parameters (mass m, wing area S_w as well as lift and drag parameters c_l, c_d) there is a certain flight path speed v for each model with which it performs the unaccelerated steady glide flight. Values deviating from this, as they occur during manual take-off when too little or too much power is applied, lead either to a strong descent (curve b in fig 2.3) or to a climb and subsequent "festoon flight", (curve a in fig 2.3). In section 4.1/Longitudinal control we have already learned how we should react to such flight phases in RC flight, see figure 4.3.

But there is another insight: the airspeed in gliding flight is not determined by the model mass alone, but rather by the specific wing mass m/S_w.

From the above calculation approach, the rate of descent v_{sr} can also be given:

$$v_{sr} = \sqrt{\frac{m \cdot g}{S_w \cdot \frac{\rho}{2}} \cdot \frac{c_d^2}{\sqrt{(c_l^2 + c_d^2)^3}}} \tag{5.4}$$

We have heard the term glide ratio or aerodynamic quality before (Tabless 2.2 und 2.3):

$$\frac{1}{\varepsilon} = E = \frac{h}{s} = \frac{v_x}{v_{sr}} \tag{5.5a}$$

or for small glide angles γ :

$$\frac{1}{\varepsilon} = E = \frac{h}{s} \approx \frac{v}{v_{sr}} \tag{5.5b}$$

For the numerical estimation of the velocities, we go back to the coefficient curves in Figures 5.2 a) and b). We had noticed that the lift coefficient $c_l(\alpha)$ within a certain angle of attack range resembles a straight line, whereas the drag coefficient $c_d(\alpha)$ rather resembles a quadratic function. We want to make use of this and calculate the velocities approximately. As an approximation function[3] for the lift

---

[3] the use of approximation functions for the computational estimation of technical interrelationships is very expedient. Since it is not a matter of high accurcy, their solutions are referred to as a qualitative progression.

coefficient we write

$$(5.6a)$$

and for those of the drag coefficient

$$c_d(\alpha) = p \cdot (\alpha - \alpha_1)^2 + c_{d0} \qquad (5.6b)$$

Here we take from the courses for the CLARK_Y: $q = 0{,}092/\deg$ and $a_0 = -2{,}5^0$, $p = 0{,}65$ und $\alpha_1 = 2^0$, $c_{d0} = 0{,}008$.

However, it is not only the airfoil of the wing that creates drag. Rather, we must consider that as a result of the pressure difference between the upper side (negative pressure) and the lower side (positive pressure), a pressure equalisation takes place at the wing tips, compare Figure 2.7. This happens with the formation of a draggy vortex, a further drag is induced. The edge flow forms a vortex plait behind the wing tip; Figure 5.5 shows how this vortex[4] plait is to be interpreted as a continuation of the airfoil flow.
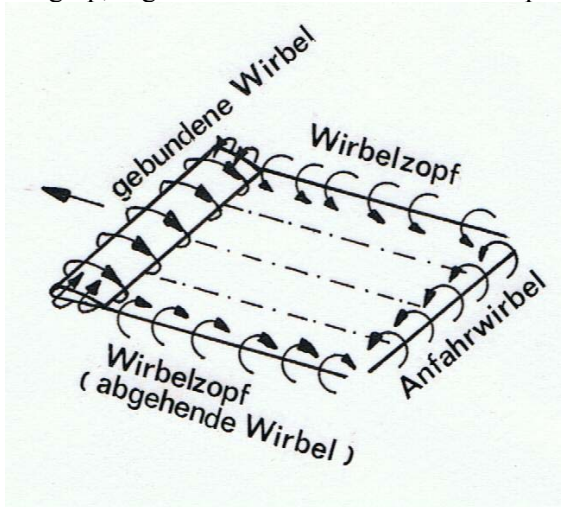

Fig 5.5: Vortex system of aerofoil in flight. Ludwig PRANDTL speaks of a horseshoe vertebra [Pra35]. The bundled vortex provides the lift.
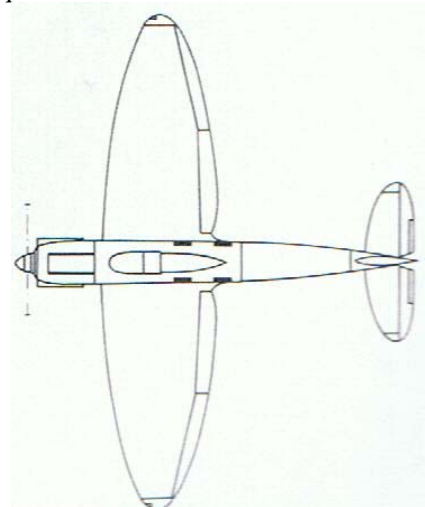
Fig 5.6: The German commercial aircraft Heinkel He 70 has an elliptical wing plan. Maiden flight of the prototype: December 1933, v = 370km/h. [KN77]

This *induced drag* is smaller the larger the span b is in relation to the wing chord length $l\mu$. The ratio is called wing aspect ratio A. Depending on the known size, see Figure 5.7, it is calculated as follows

$$A = \frac{b}{l_\mu} = \frac{S_w}{l_\mu^2} = \frac{b^2}{S_w} \qquad (5.7)$$

The coefficient of the induced resistance c_{di} obeys the relation
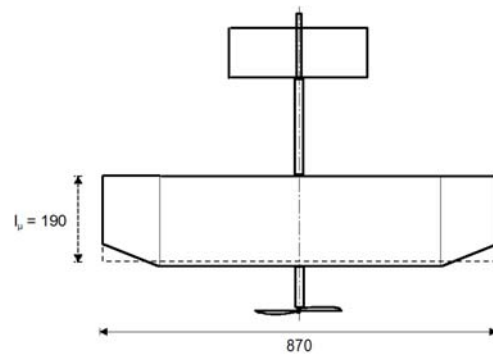
$$c_{di} = \frac{c_l^2}{\pi \cdot A} \qquad (5.8)$$

---

[4] Wild geese, for example, utilise the effect of the upward flow behind the wingtips when flying in wedge-shaped formations. This saves them energy.
On the other hand, the wake vortices caused by large commercial aircraft can be dangerous for smaller sports aircraft if they only follow at a distance of 1 to 2 kilometres.
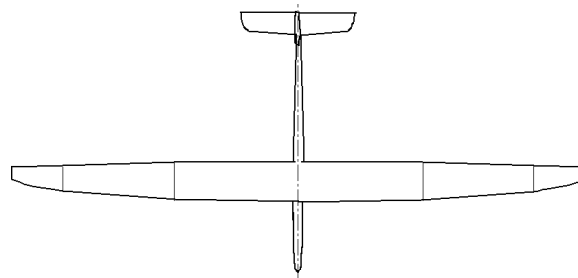
Aircraft		**Aspect ratio A**
Slowflyer RL1		$b = 8,7dm$ $S_w = 16.34dm^2$ $A = b/l_\mu = 870/190$ **A = 4,6**

$l_\mu = 190$

870

Gliding model RS3		$b = 34dm$ $S_w = 68dm^2$ $A = b^2/S_w$ **A = 17**
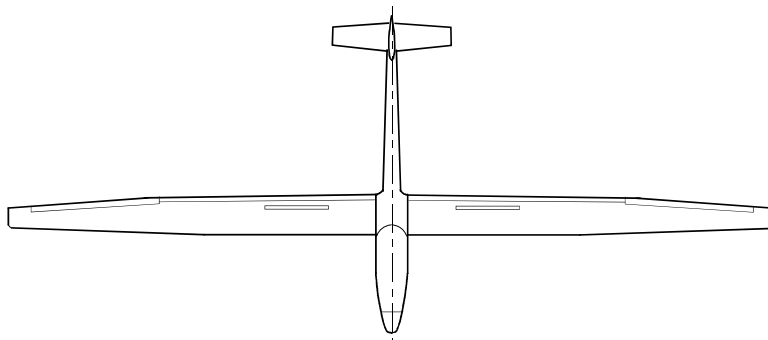
Glider Jantar 2b		$b = 20,5m$ $S_w = 14,25m^2$ **A = 29,4**
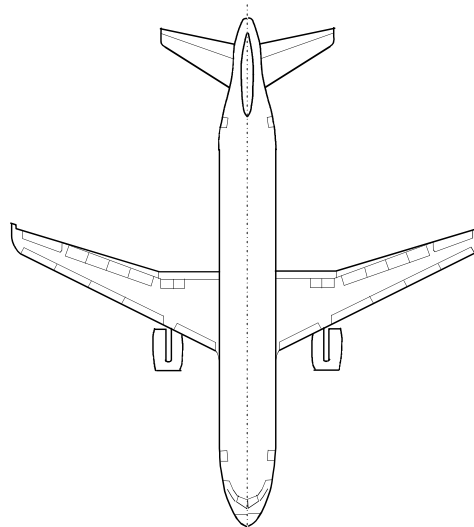
Commercial aircraft A320		$b = 33,9m$ $S_w = 122,6m^2$ **A = 9,4**

Fig 5.7: Wing aspect ratios A for different wing planforms. For gliders, large values are used in the interest of slow thermal circling; for powered aircraft, aspect ratio is designed according to economic considerations (range, speed in commercial flight) or according to manoeuvrability (aerobatics).

where the influence of the aspect ratio A becomes clear. Strictly speaking, this formula only applies to a wing plan with an elliptical shape, see Figure 5.6; this produces the lowest induced drag of all geometries. However, we continue to use it as an approximation.

Now, in addition to the wing, the fuselage/tail boom and the tail unit also belong to the aircraft/airplane model; both components are washed around by the air during flight and generate resistance. In the coefficient notation we take this into account with the so-called harmful resistance c_{dh} (although actually any kind of resistance is harmful). Thus the relationship for the total drag coefficient is now

$$c_d(\alpha) = p \cdot (\alpha - \alpha_1)^2 + c_{d0} + \frac{c_l^2}{\pi \cdot A} + c_{dh} \qquad (5.6c)$$

Now we can calculate the course of the airspeed and sink rate depending on the angle of attack according to equations (5.3), (5.4). As an example we use the mentioned glider model RS3 with the values $S_w = 68 dm^2$, $m = 2.4 kg$, $A = 17$ and $c_{ds} = 0.015$. We vary the wing angle of attack in the range $0 deg\, \alpha \le 10 deg$ by trimming the elevator, thus producing different glide angles γ. The results are shown in Figures 5.8a) to d).
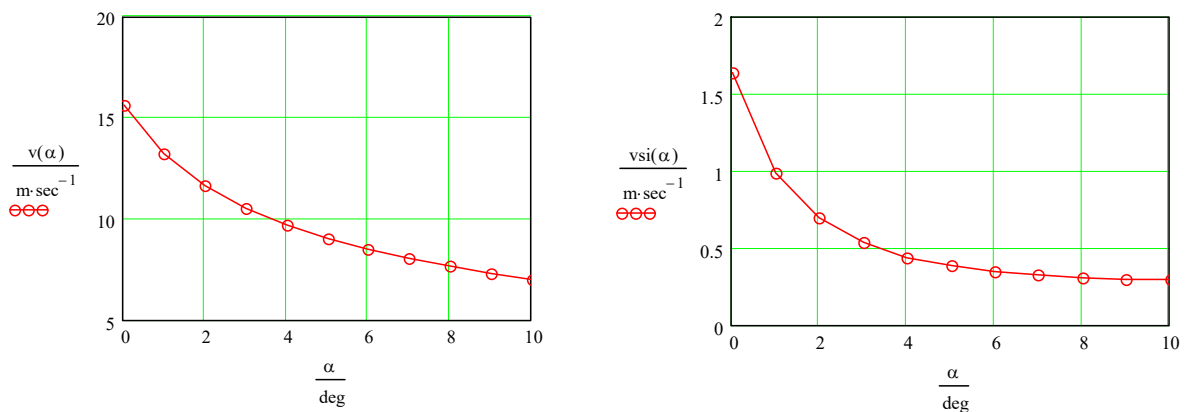
Fig 5.8: Speed ranges of a glider model in gliding flight. a) Path velocity v   b) Sink rate v_{sr}. The glide angle γ varies only slightly: from γ = 2deg (slow flight) to γ = 5deg (fast flight).
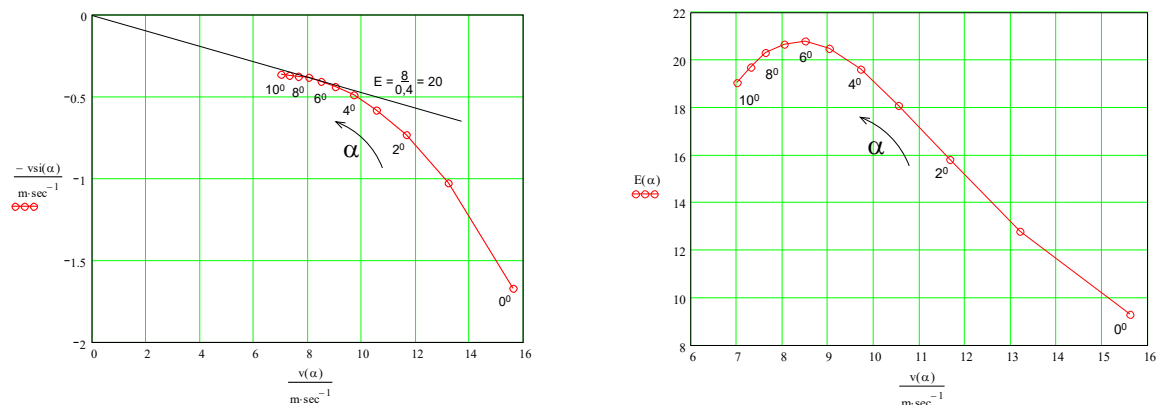
Fig 5.8: c) Velocity polar $v_{sr}(v)$ and derived from this d) the course of aerodynamic quality E(v) = 1/ε (v) The tangent point lies at the maximum E_{max} = E(α = 6deg)

We see that changing the angle of attack changes the orbital velocity of the model in the range $16 m/s \ge v \ge 7 m/s$, while the corresponding sink rate varies in the range $1.6 m/s \ge v_{sr} \ge 0.29 m/s$. Almost more interesting than the numerical values themselves, however, are the curves: one can see that the path velocity $v(\alpha)$ could very well be reduced by an even higher angle of attack (mathematically equivalent to a higher lift coefficient), but that the rate of descent $v_{sr}(\alpha)$ is heading towards a stationary final value.

Furthermore, for the evaluation of gliders it has become common to show the (negative) sink rate $v_{sr}(\alpha)$ above the airspeed $v(\alpha)$, Figure 5.8c. From this curve, called the speed polar curve, one not only recognises the minimum permissible path speed v_{min} and the corresponding minimum sink rate v_{sr_min}. Rather, the slope of a straight line between the origin of the coordinates and the tangent point also allows a statement to be made about the best possible glide ratio ε or aerodynamic quality $E = 1/\varepsilon$. It is also interesting to note that E_{max} with $\alpha = 6deg$ is achieved at a different angle of attack than the minimum sink rate v_{sr_min} at $\alpha = 10deg$. This plays a role in competition flights of gliders and glider models: for slow circling in thermals the lower speeds are needed, while for cross-country flight the best glide ratio is required.

The above calculation of characteristic values - and also the following ones - are intended to describe the basic procedure. However, due to the approximations, absolute values can only be determined with a certain tolerance; for example, the aerodynamic quality with $E_{max} = 25$ deviates by $\approx 10\%$ from the measured value $E = 22$, cf. example 5.1b). On the one hand, more accurate calculations require the use of airfoil polars measured in the Reynolds number range of the flight model, see chapter 7, on the other hand, measured values also have their tolerances, see section 8.5.

Figure 5.9 shows the calculated individual resistances of an example glider model for the flight modes slow flight a) and fast flight b). We see that in *slow flight* the *induced drag* dominates, in *fast flight* the *airfoil drag*.
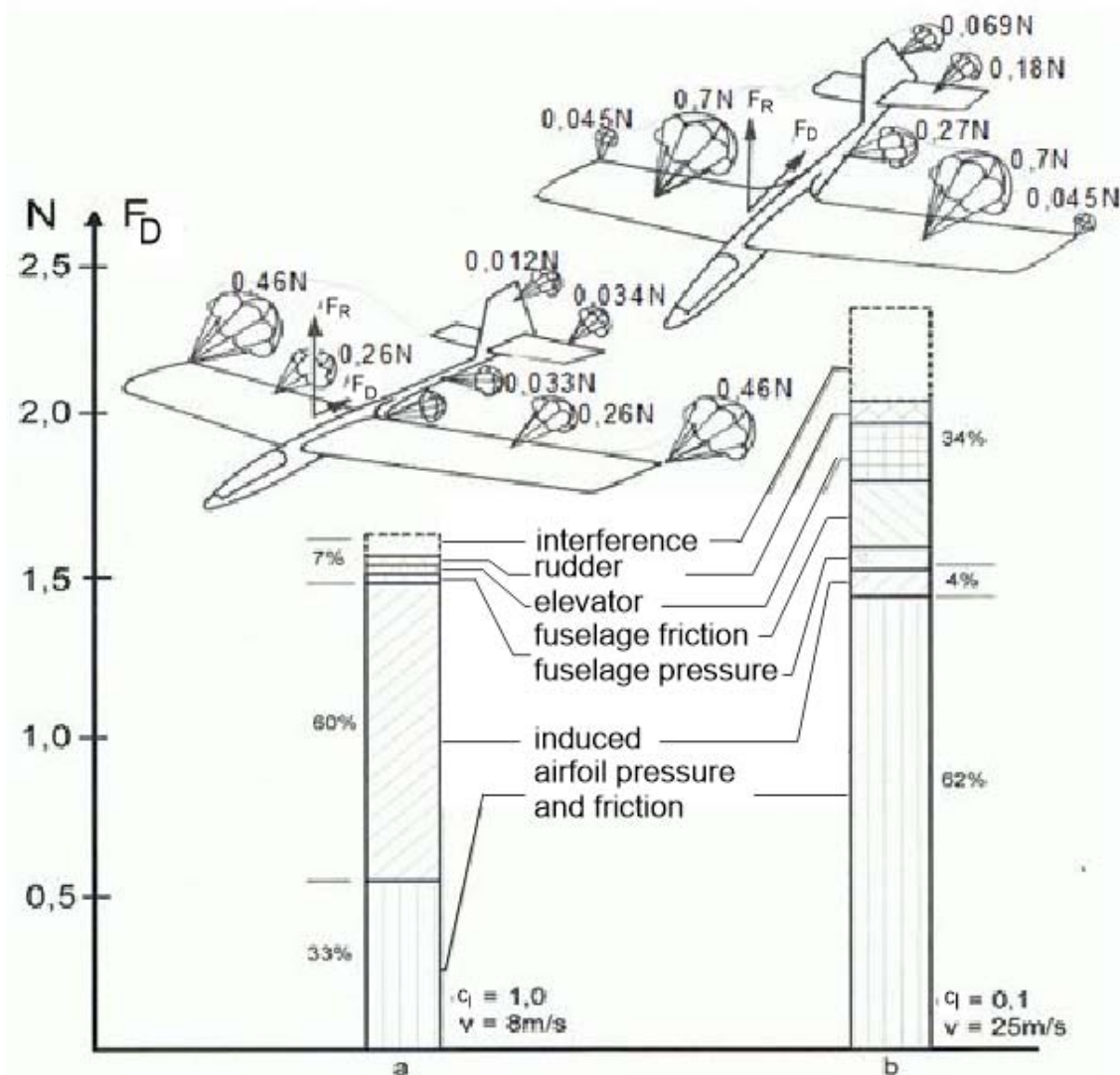

Fig. 5.9: Drag forces on a glider model a) with high, b) with low lift coefficient

5.2-2 Horizontal flight

Let us now look at stationary horizontal flight. This is caused by a thrust force F_T acting on the model due to an installed propulsion system (propeller, jet engine), Figure 5.10. Here, too, the forces are in equilibrium, $F_L = F_W$, $F_T = F_D$. With knowledge of Eq.(5.1), (5.2) we can write

Fig 5.10: Forces in stationary horizontal flight
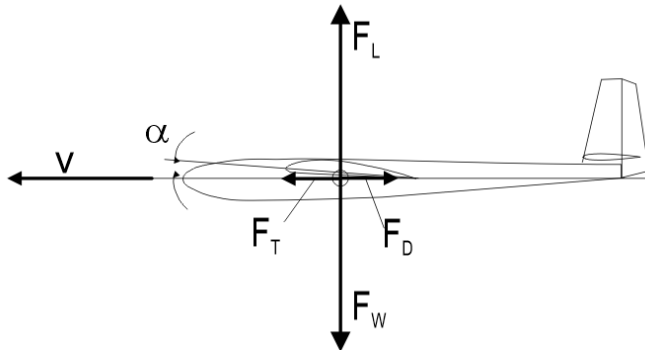
$$m \cdot g = \frac{\rho}{2} \cdot v^2 \cdot S_w \cdot c_l$$

$$F_T = \frac{\rho}{2} \cdot v^2 \cdot S_w \cdot c_d$$

These two equations are fulfilled for every speed. We can therefore solve for v^2 and equate it to determine the thrust force:

$$F_T(\alpha) = m \cdot g \cdot \frac{c_d(\alpha)}{c_l(\alpha)} \qquad (5.9)$$

and the velocity to

$$v(\alpha) = \sqrt{\frac{m \cdot g}{S_w \cdot \frac{\rho}{2}} \cdot \frac{1}{c_l(\alpha)}} \qquad (5.10)$$

In the figures Fig. 5.11 a) and b) these relations are evaluated for our example model RS3, which now has a higher mass of m = 3kg due to the motorisation. The results are shown on a semi-logarithmic scale in order to better recognise the respective minimum values; for the thrust force, for example, this is $F_T = 1.2N$ for α = 7deg.

It should be emphasised once again that the speed range of the model in *horizontal flight* is being investigated here. This results from the fact that for a given angle of attack range $\alpha_0 < \alpha \le 10$deg, both the thrust force F_T and the speed v are determined which are necessary to keep the model in horizontal flight, where the lift force is therefore always equal to the weight force $F_L = F_W$. Of course, the thrust force curve F_T conforms to the resistance force curve F_D, because only the latter must be in equilibrium with the thrust force for stationary horizontal flight.
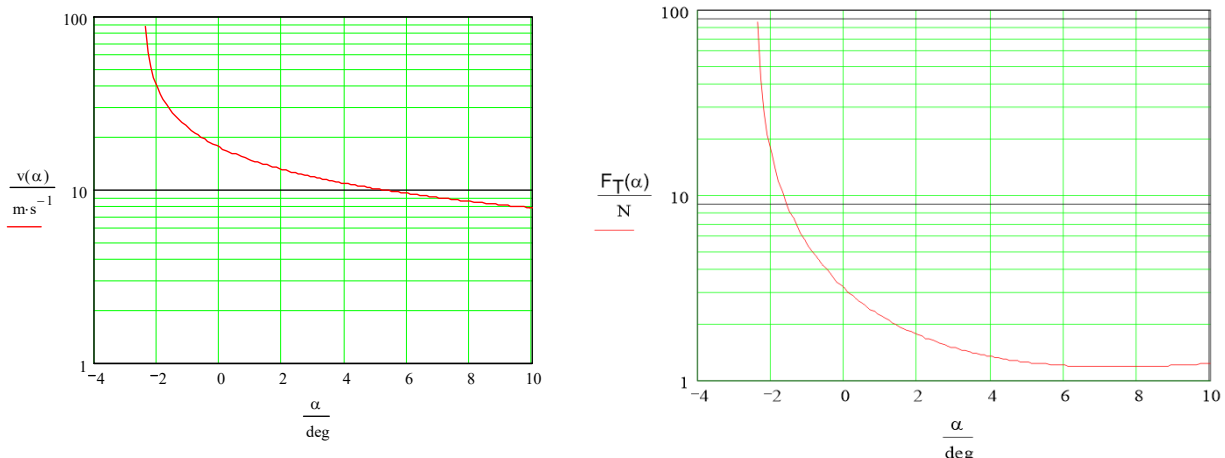

FIG. 5.11a) speed range and b) required thrust of a model for horizontal flight.

In our calculation example, according to figure 5.11, the speed for this is in the range $v_{min} = 7.8$m/s to $v_{max} = 87$m/s, for which a thrust of $F_{T\_min} = 1.2$N to $F_{T\_max} = 86$N must be available.

However, it should be noted that the maximum speed is a calculated value which cannot be realised in practice - another variable, the so-called *torque* around an imaginary axis in the aerofoil, wants to twist (torsion) the aerofoil counter-clockwise at small angles of attack and thus leads to oscillations (flutter) of the aerofoil, which can destroy it.


5.2-3 Climb flight

A first, very descriptive consideration [Br80], Figure 5.12, results from the following consideration: if a flying model flies without propulsion, it sinks in the time Δt by the height Δh1. The *sink rate* results from

$$v_{sr} = \frac{\Delta h1}{\Delta t}$$

If the motor is switched on, the airscrew generates the forward thrust force F_{th}. If this is equal to the drag force, $F_T = F_D$, then the model flies horizontally, see Figure 5.10. If the propulsive force is increased, $F_{th} > F_d$, then the model moves upwards at the *rate of climb*:

$$v_{cr} = \frac{\Delta h2}{\Delta t}$$
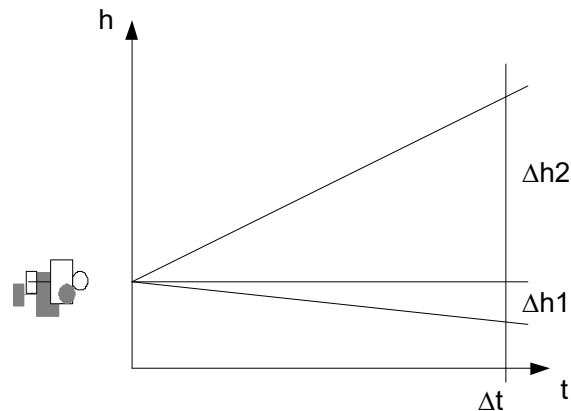
The propulsion system thus performs a lifting work in the climb with the force component weight force F_W = mass*g and the displacement components Altitude difference Δh = Δh1 + Δh2:

Fig12: In the case of small climbing angles, the required drive power can be determined from the lifting work.

$$W_{cr} = F_W * (\Delta h1 + \Delta h2)$$

From the lift work W_{cr} and the time interval Δt we can determine the desired output power P_{out} for the climb:

$$P_{out} = \frac{W_{cr}}{\Delta t}$$

$$P_{out} = F_W \cdot \left(\frac{\Delta h1 + \Delta h2}{\Delta t} \right)$$

$$P_{out} = m \cdot g (v_{sr} + v_{cr}) \tag{5.11}$$

This power must be delivered by the propeller to propel the model into the sky at a rate of climb v_{cr}. The sink rate v_{sr} must be known for this - either calculated according to Eq(5.4) or available as a measured value. However, we will soon see that this relationship only provides a sufficiently accurate result for small angles of climb $\gamma \leq 10$.

For calculation with arbitrary angles of climb we consider the forces according to figure 5.13.
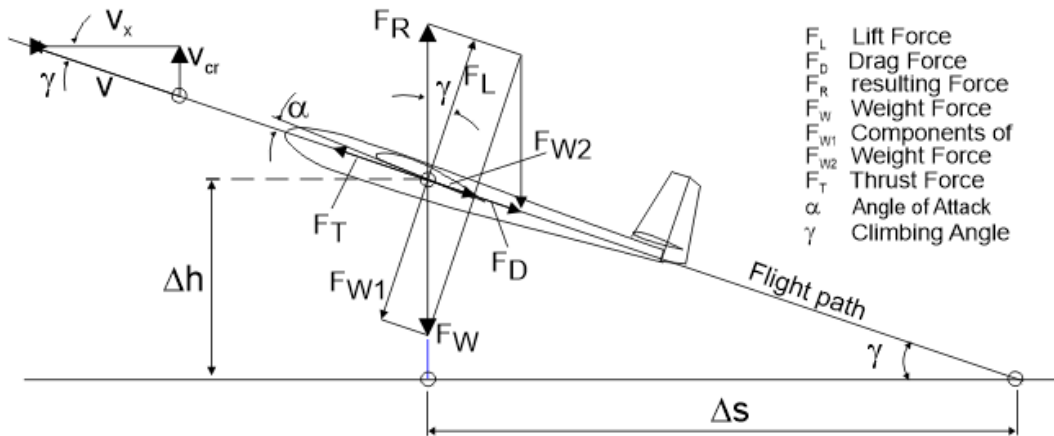
Fig 5.13: Forces in unaccelerated climb. The weight force FG is decomposed into the components
FG1 = FA = FG*cosγ, FG2 = FG*sinγ. Damit gilt FS = FG*sinγ + FW. Außerdem gilt vst = v*sin(γ)

Compared to horizontal flight (compare figure 5.10), the climb results from a greater thrust force F_{th} acting on the model/aircraft than is necessary to compensate for the drag force F_{th}. According to figure 5.13 the following forces are in equilibrium: $F_S = F_{G2} + F_W$, $F_A = F_{G1} = F_G*\cos\gamma$, $F_{G2} = F_G*\sin\gamma$

Again using the basic equations (5.1), (5.2) we can write

$$F_W \cdot \cos(\gamma) = \frac{\rho}{2} \cdot v^2 \cdot S_f \cdot c_a \tag{5.12a}$$

and for the shear force FS the sum of the weight force component FG2 and the resistance force FW according to (5.2) applies:

$$F_T = F_W \cdot \sin(\gamma) + \frac{\rho}{2} \cdot v^2 \cdot S \cdot c_d \tag{5.12b}$$

By solving both equations for v^2 and equating, we obtain for the thrust force

$$F_T(\alpha) = F_W \cdot \left[\frac{c_d(\alpha)}{c_l(\alpha)} \cdot \cos(\gamma) + \sin(\gamma) \right]$$

But since also applies

$$v_{cr} = v \cdot \sin(\gamma),$$

the necessary thrust force is

$$F_T(\alpha) = F_W \cdot \left[\frac{c_d(\alpha)}{c_j(\alpha)} \cdot \cos(\gamma) + \frac{v_{cr}}{v} \right]$$

and the required power

$$P_{out} = F_T(\alpha) \cdot v = F_W \cdot \left[\frac{c_d(\alpha)}{c_l(\alpha)} \cdot v \cdot \cos(\gamma) + v_{cr} \right]$$

For small gradient angles $\gamma \le 100$, the value of $\cos(\gamma) \ge 0.99 \approx 1$ remains; moreover, the following applies

$$\frac{c_w(\alpha)}{c_a(\alpha)} \cdot v \approx v_{si}$$

and thus in this case also

$$P_{out} \approx F_W \cdot \left(v_{sr} + v_{cr)}\right) .$$

This confirms our equation (5.11) obtained from the first observation.

For the larger angular range 0deg < γ < 89deg we calculate the velocities from (5.12a) according to

$$v(\alpha) = \sqrt{\frac{2 \cdot F_W \cdot \cos(\gamma)}{\rho \cdot S_w \cdot c_a(\alpha)}} \qquad (5.13)$$

and because of $v_{cr} = v \cdot \sin(\gamma)$

$$v_{cr}(\alpha) = \sin(\gamma) \cdot \sqrt{\frac{2 \cdot F_W \cdot \cos(\gamma)}{\rho \cdot S_w \cdot c_a(\alpha)}} \qquad (5.14)$$

But how do we determine the angle of climb γ and how can the thrust force F_T the included in the calculation? A closed solution is not possible here, rather iteration must help: For a chosen initial value γ_0 and the desired angle of attack α we calculate the path velocity v(α, γ_0) according to Eq. (5.13) and then the drag force F_T(α, γ0) with Eq. (5.2) and check with the help of the relation, cf. Fig. 5.13,

$$\gamma_1(\alpha) = \arcsin\left[\frac{F_T - F_D(\alpha, \gamma_0)}{F_W}\right] \qquad (5.15)$$

whether $\gamma_1 < \gamma_0$ or $\gamma_1 > \gamma_0$. According to the result, we increase or decrease the initial value γ_0 for the next round and calculate again ... until $\gamma_1 = \gamma_0 \pm \Delta$ is fulfilled (Δ = permitted deviation). We carry out this calculation for a desired thrust force in the entire angle of attack range; this is advantageously done by the PC in a mathematical programme.

Analogous to the *speed polar* of a glider model in gliding flight, Figure 5.8c, the so-called *climb polar* can be calculated in this way. This is done in Figure 5.14 a, b for the already mentioned model RS3 for two assumed thrust force values F_{th}.
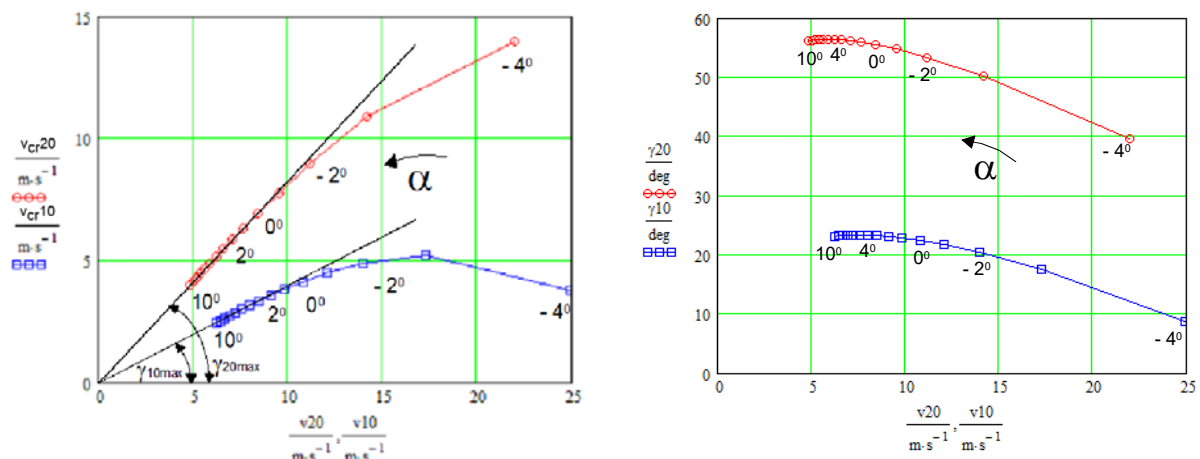
Fig. 5.14   a) Climbing polar of a model $v_{cr}(v)$ for two assumed thrust force values F_T = 20N und F_T =10N und b) associated angle of climb γ(v); run variable α = angle of attack. The tangent to the climb polar describes the maximum possible angle of climb: γ_{max} = arcsin(v_{cr}/v)

It can be seen that the maxima for the highest rate of climb v_{cr_max} are at higher path velocities v than those for the maximum angles of climb γ_{max}. For example, for F_T=10N the following results are obtained:

greatest rate of climb $v_{cr10max}$ = 5.3m/s at v = 17.3m/s and greatest angle of climb γ_{10max} = 23deg at v = 7.6m/s; for F_T = 20N: $v_{cr20max}$ = 14m/s at v = 22m/s; $\gamma_{20degmax}$ = 56deg at v = 5.9m/s.

However, we also see that the minimum path speed of the model for F_T = 20N with v = 5m/s falls below the minimum speed allowed for gliding flight v_{min} = 7m/s, compare figures 5.8a) to c). This is due to the fact that with increasing angle of climb γ the lift generated by the aerofoil is allowed to become smaller and smaller (and becomes smaller and smaller), because the thrust force F_T takes over the forward motion of the model more and more.

5.2-4 Hovern

For a long time, hovering flight in the model sector was reserved for helicopters. Due to the high torques of brushless motors, this is now also possible for fixed-wing models. Here, the propeller must deliver a thrust force that corresponds to the weight force of the model: $F_T \geq m*g$, see Figure 5.35 in Chapter 5.3-3 Drive Components / Motor and Propeller.

5.3 Propulsion

5.3-1 Thrust, power, efficiency

For the engine-driven flight phases (horizontal, climb), in addition to the knowledge of the thrust force F_{th} generated by the propeller, the output power P_{out} emitted by it is often of interest. We obtain this via the relations

$$W = F \cdot s, \qquad P = \frac{W}{t}, \qquad P = \frac{F \cdot s}{t}, \qquad P = F \cdot v$$

to
$$P_{out} = F_T \cdot v \tag{5.16}$$

For clarity, the power curves for the results of the horizontal flight, Figure 5.15a, and the climb, Figure 5.15b, are shown. This shows that in horizontal flight, an output power of Pout ≤ 10W is sufficient for the slow flight range v ≤ 10m/s, while for the - only theoretically possible - extreme fast flight of v ≈ 70m/s, a power of Pout ≈ 4kW would be required. In climb flight, the thrust F_T = 10N for the maximum rate of climb at v = 17.3m/s would have to be generated with a power P_{out_10} = 170W and the thrust F_T = 20N for the maximum rate of climb at v = 25m/s with P_{out_20} = 440W, Fig. 5.15b.

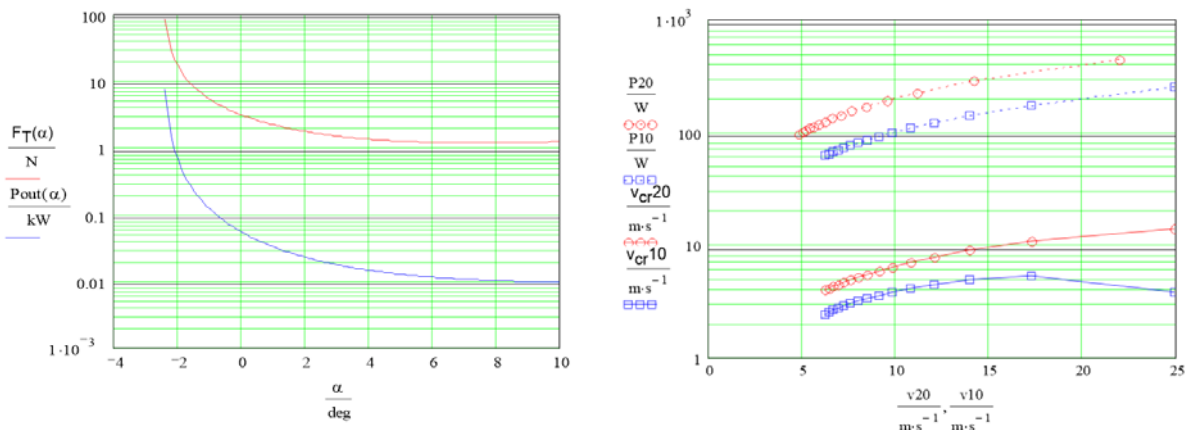Fig 5.15 a)　Necessary power output (blue) for horizontal flight and b) for the climb regimes according to Figure 5.14 (dotted)

In order to be able to infer the required input power backwards, one must include the efficiencies of the components involved in the drive, Figure 5.16. These multiply:

$$P_{out} = P_{in} \cdot \eta_{st} \cdot \eta_{mot} \cdot \eta_{getr} \cdot \eta_{prop},$$

so that for the necessary input power applies

$$P_{in} = \frac{P_{out}}{\eta_{st} \cdot \eta_{mot} \cdot \eta_{getr} \cdot \eta_{prop}} \qquad (5.17)$$
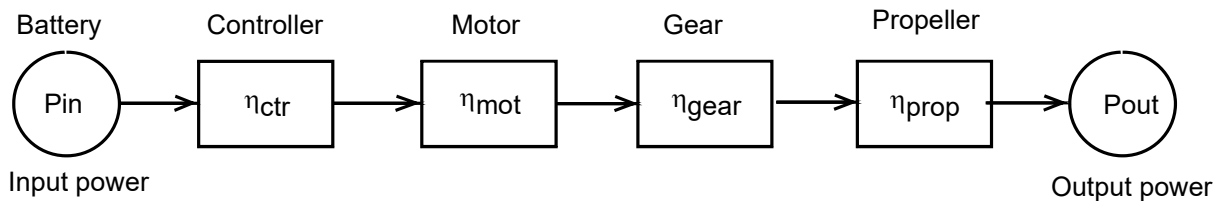

Fig 5.16   Chain of action of an electric drive with its efficiencies [Sche02].

Typical values for the individual components are in the range of

Controller: η_{ctr} = 0,85 … 0,95
Motor: η_{mot} = 0,7 …   0,9
Gearbox: η_{gear} = 0,85 … 0,95
Propeller: η_{prop} = 0,4 …   0,7

Example 5.2

a) the mass of the indoor training model pusher_tiefdecker (pu_td) is m = 170g when using a 360mAh battery. It is supposed to reach a speed of v ≥ 5m/s within a distance of s = 5m.
1. What propulsive force Fs is required for this? We consider the starting process approximately as a **uniformly accelerated movement**. After time t, the relationship s = (a*t^2)/2 applies to the distance travelled, from which it follows for the acceleration a = 2*s/t^2. The speed increases linearly over time t, v = a*t, thus a = v/t. By equating, we obtain the time after which the desired speed is reached: t = 2s/v = 2*5m/5m*s^{-1} = 2s. From this, the value for the acceleration is determined as a=2*5m/(2s)^2 = 2.5m/s^2. With Fs = m*a we obtain the required propulsive force as F_{th}= 170g*2.5m/s^2 = 0.43N.
   In chapter 8, under *Selected Topics*, it is shown which values were obtained by measurement: a = 2.3m/s2, F_{th} = 0.39N; the model took off after a distance s ≈ 7m at a time of t = 2.5s, the velocity was v = 5.4m/s. This case also shows how useful an estimation with the help of approximation relations can be. That one can also calculate more precisely is shown in section 8.8. There, air resistance and rolling friction are taken into account.
2. The final speed of the pu_td was measured at v = 11.5m/s. It is assumed that the equilibrium state $F_{th} = F_d$ according to Figure 5.10 is reached, i.e. a **uniform movement** is present. What output power is required for this speed and what efficiency of the drive results if P_{el} = 2.8A*7.4V ≈ 21W was measured as the power input?
   From Eq. (5.10) the lift coefficient is c_l = m*2g/(v^2*Af*ρ) = 0.125; from the polar diagram in Fig. 8.3 the associated drag coefficient is c_{dp} = 0.04. Together with the "harmful resistance coefficient" c_{ds} = 0.01, the result is c_{dges} = c_p+c_{ds} = 0.05. From equ (5.9), the resistance force is F_d = m*g*c_{d_ges}/ca = 0.67N. Since $F_d = F_{th}$, the power output of the propeller is P_{out} = v*F_T = 11.5m/s*0.67N = 7.7W. The efficiency of the drive is therefore η = P_{out}/P_{el} = 7.7W/20.7W = 0.37.

b) What input power is required to drive the RS3 motor glider if it is to
1. reach a maximum horizontal speed of v = 20m/s, so that it can move forward even in a strong headwind?
   According to fig 5.11a) v = 20m/s is achieved with an angle of attack of α = - 0.5deg; according to figure 5.15a) the propeller must deliver a power P_{out}(-0,5deg) ≈ 100W;
2. reach a rate of climb v_{cr} = 10m/s? According to Fig. 5.15b) this rate of climb is reached at
   v = 17m/s, the propeller must deliver a power Pout ≈ 300W.
   We assume the following values for the efficiencies: η_{ctr} = 0.9; η_{mot} = 0.8; η_{gear} = 1 (no gearbox present); η_{prop} = 0.4. Thus, according to Equ(5.17), for the larger value of the output power of 300W, the input power become P_{el} = 300W/(0,9*0,8*1*0,4) = 1042W = 1,042kW.
   This power can be generated, for example, by 5 LiPo cells, corresponding to a voltage level of U_{Akku} = 5*3.7V = 18.5V and a motor that can handle a current of I_{max} = 1.042kW/18.5V = 56.3 ≈ 60A for a short time. This drive configuration was realised in model for photographyRS3_fotfly [EK07]. The evaluation of flights with different propellers resulted in an overall efficiency range P_{out}/P_{el} of 0.40 ≤ η ≤ 0.44.

The model RS3_fotfly [EK07] during a test flight on the Elbe meadows in Steutz 2007

c) The Airbus A320 requires the speed v_{lift} = 270km/h = 75m/s for take-off.

1. what thrust F_T must the two jet engines generate during take-off to reach this speed over a distance of s = 1500m in t = 35s? The mass is m = 77000kg. From the acceleration $a = 2*s/t^2 = 2*1500m/(35s)^2 = 2.45m/s^2$ we calculate $F_T = m*a$ = 187kN; according to the data sheet [A320_b] the engines generate: 2x 118kN.

2. what thrust must the two jet engines generate during cruise?
   In forums [A320_c] a glide ratio of E = 20 is mentioned for the A320. This gives us for the drag force $F_d = F_L/E = m*g/E = (77000kg*9.81*m/s^2)/20$ = 37.8kN. But because $F_D = F_T$, cf. figure 5.10, the required total thrust is $F_T \approx 38$kN.

3. What is the efficiency of the jet engines if, according to the data sheet, the kerosene consumption (fuel_flow) at cruising altitude is K_{fuel} = 2700 litres/hr?
   The cruising speed is v_{cruise} = 900km/h = 250m/s, cf. example 5.1d). Thus the output power generated by both engines becomes $P_{out} = F_T*v_{cruise}$ = 38kN*250m/s = 9.5MW.
   The density of kerosene is 0.8kg/litre, so the fuel consumption is K_{fuel} = 0.8*2700 = 2160kg/hr. The calorific value of kerosene is C_{fuel}=11.9kW*hr/kg. This gives the power of the burnt kerosene as $P_{ker} = K_{fuel}*C_{fuel}$ = 2160kg/hr*11.9kW*hr/kg = 25.7MW. The efficiency of both jets is thus $\eta = P_{out}/P_{ker}$ = 9.5MW/25.7MW = 0.37.

5.3-2 Drive components / rechargeable battery (Accumulator)

Although drive tests with electric motors for model aircraft were already carried out in the 1970s by F. Militky and G. Bruß, it took until about 1990 before suitable batteries for direct current motors were available in the form of the nickel-cadmium chemical system. Also promoted by the development progress in mobile radio technology, these were replaced around the turn of the millennium by lithium-ion or lithium-polymer batteries with a higher energy density.
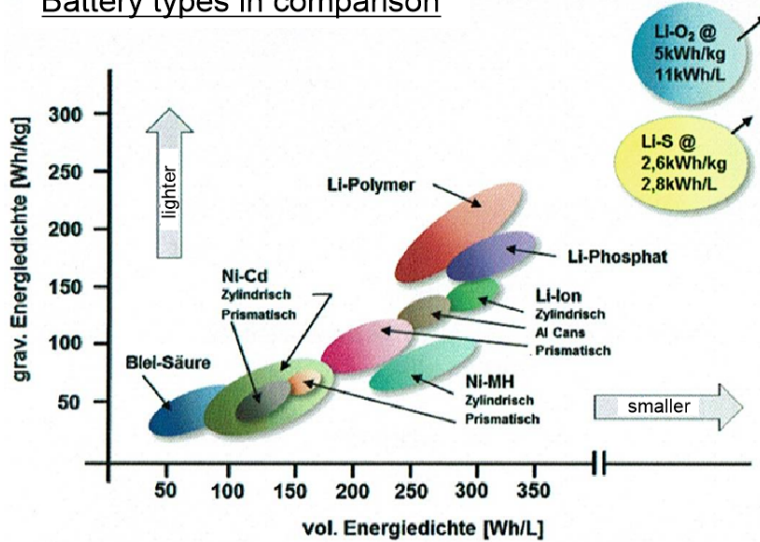
Fig 5.17 Mass and volume-related energy density of batteries under development [NaWi14]

Just for comparison: the energy density of petrol is 43MJ/kg = 12kWh/kg, that of the best LiPo batteries 240Wh/kg; so there is still the "small" difference of a factor of 50 here! Current developments, however, allow us to look optimistically into the future: Lithium systems in combination with sulphur or oxygen have at least such a magnitude already in their sights, Figure 5.17.

The relationship between current yield and duration of current "delivery" of a rechargeable battery is given by its charge capacity C:

$$C = I \cdot t$$

In the case of a constant discharge current Io, this can flow during the discharge time

$$t_D = \frac{C}{I_o} \tag{5.18}$$

The magnitude of the discharge current Io, which can be drawn, and the duration of the discharge t_D called discharge time in technical jargon, are thus inversely related, Figures 5.18a and b.
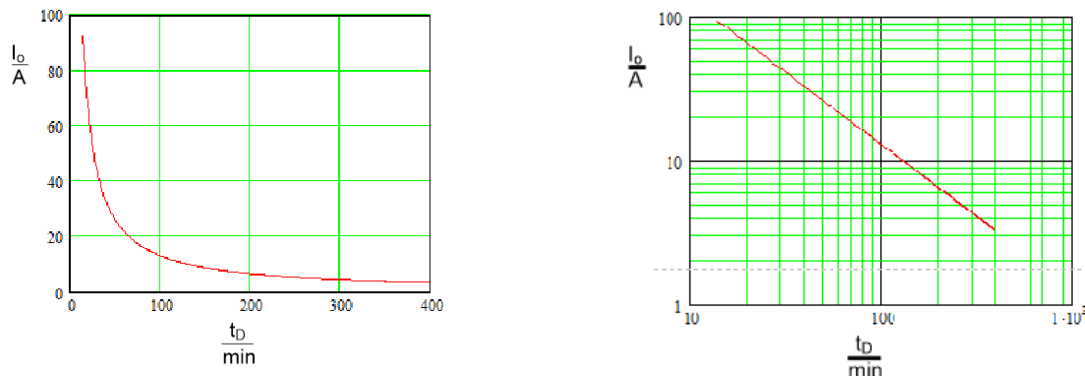
Fig 5.18 Theoretical discharge current available depending on the discharge duration t_D
a) shown on a linear scale, the result is   b) on a double logarithmic scale shown results in
   a hyperbola   a straight line

This relationship is evaluated below for two specific batteries: one with a capacity of C = 1000mAh and one with C = 360mAh, see Fig. 5.19. Here, the table values in the middle column indicate how long a desired current Io can flow during the discharge time t_D according to calculation Eq. (5.18) and, on the other hand, which times resulted from the measurements, right column. The state "battery empty" was defined by the level U_{min} = 3.3V/cell, to which the battery voltage drops during the discharge process, see the following discharge diagrams.

Io/A	t_D/min theoretisch	t_D/min gemessen
1	60	60,1
2,5	24	23,4
5	12	11,85
10	6	------

Io/A	t_D/min theoretisch	t_D/min gemessen
1	21,6	15
2	10,8	6
2,5	8,6	1,7
3	7,2	0,8
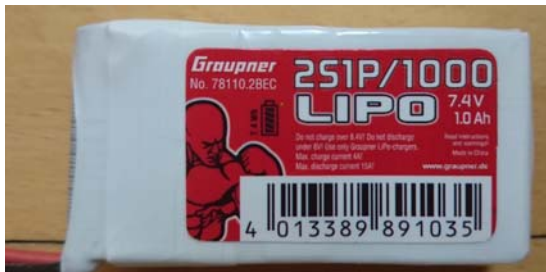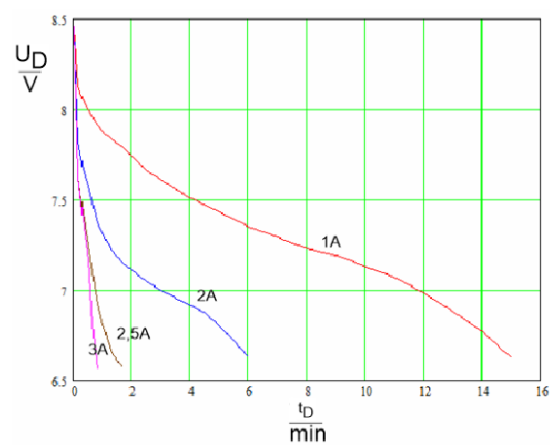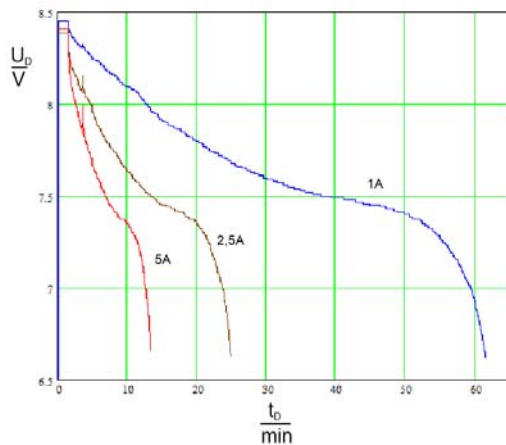
Fig 5.19 Two batteries with 2 cells each with regard to their discharge times t_D in comparison:
a) brand new, C = 1000mAh, Ri = 30mΩ;   b) "worn out" C = 360mAh, Ri = 300mΩ

We can see that a new battery can be calculated very well according to Eq (5.18). However, the capacity decreases with the number of charging cycles, so that only low operating times are achieved with an "aging battery", right column in table of Fig. 5.19b. The 360mAh battery was usually used by the author during indoor RC training with the model pusher_td.

$$U_L = U_i - I_L \cdot R_i$$
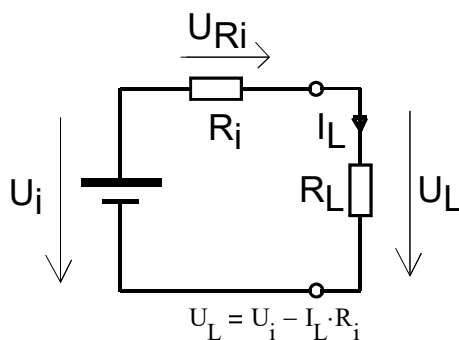
Fig. 5.20 Battery equivalent circuit

Apart from the capacity C of a battery, its internal resistance Ri is a further "invisible" parameter, Figure 5.20.
This parameter can also increase many times (up to 10 times!) over the course of the charging cycles of a brand-new battery. In addition, however, a low ambient temperature also noticeably increases the internal resistance. In such cases, it is recommended to keep the battery warm until it is used in the model. An increased internal resistance means that only a reduced proportion of the internal voltage U_i is available for connected load, even in the "battery full" state.
Example: Ri = 0.3Ω, Io = 3A results in a voltage drop U_{Ri} = 0.9V. Related to the nominal voltage $U_{ratings}$ = 3.7V, this is a voltage loss of about 25%.

Information on the care and safe use of LiPo's is given at the end of this chapter. The labels on the batteries are explained below. Here the manufacturer provides information on the size of the charging and discharging current, which must be observed. In most cases, these are printed on the battery in plain text. In other cases, it can be taken from the somewhat misleading *C-rate* value, see the following examples in Fig 5.21.

2S = 2 cells =>7,4V; capacity C = 0,8Ahr, this results in "1C" => 0,8A

max continous current: 25A =>25*0.8 = 20A;
max short burst current: 40C => 40*0,8A = 32A

2-1000: 2 cells =>7,4V; C = 1000mAhr
capacity C = 1Ah, from that „1C" => 1A
max charge current: 3A => 3C
max continous current 3A = 3C
max short burst current 6A = 6C

2S1P/1000: 2 cells in series, no parallel connection /1000mAhr
capacity C = 1Ah, from that „1C" => 1A
max charge current: 4A
max continous current 15A

```
            Lipo 2S 1C 5000mAh 25/50C              Lipo 2S 1P/ 1000mAh
                 ↑ ↑      ↑      ↑  ↑                    ↑   ↑
            2 cells |     |      |  |              2 cells in series    |
      max charge curr. 5A => 1C  |  |                  no cells connected in parallel
               capacity => 5Ah   |  |
         max discharge 125A = 5A*25C      |     and a final designation example:
                      ≈ 5Min  |                     Lipo 3S  2P/ 2400mAh
         max short burst current 250A => 5*50C          ↑    ↑
                           1… 5s              3 cells in series   |
                                                  2 cells connected in parallel each
```

Fig 5.21 Designation examples for LiPo batteries and their meaning

The Li-Po batteries mentioned so far are preferably used in model aviation to supply power to drive motors and receivers. A second category, the NiMH batteries, are more commonly used in transmitters. Figure 5.22 shows the Graupner mx-16 as an example. When it is switched on, a constant current Io = 200mA flows, which means that with the specified capacity of 2000mAhr, an operating time of t_D = 2Ah/0.2A = 10hr can be expected. Here, too, practice shows that this time is not exhausted. In fact, the manufacturer has already set the alarm signal "battery low" at 4.6V - corresponding to 1.15V/cell - which results in an operating time of around t_D = 7hr. The measured discharge characteristic curve for this is shown in Figure 5.24.

Modern chargers offer special charging methods for both types, which must be used; otherwise there is a risk of damage or even destruction of the battery. The charging of a LiPo is done according to the so-called constant current/constant voltage method: Until the final charging voltage of 4.20V is reached, the constant current set on the charger flows. When the voltage value is reached, the charger successively reduces the current towards zero.

It switches off and signals "battery full" when the charging current has dropped to about 10% of the set value, see Fig. 5.24. Incidentally, it follows from this charging method that batteries with increased Ri should be charged with a reduced charging current, as they switch off reduced by the voltage drop URi and are charged less fully at the nominal charging current.

Fig 5.22 Power supply of the Graupner HoTT mx16 transmitter with NiMH battery pack; 4,8V; 2000mAhr

The charging process for NiMH batteries is different: when the final voltage is reached, a slight gas development occurs, which in turn leads to a voltage reduction due to an increase in pressure. This reduction is used for a sudden current cut-off; in the case of the Graupner Ultramat 16S charger at the value $\Delta U = -20mV$, see Figs. 5.23b and 5.24.
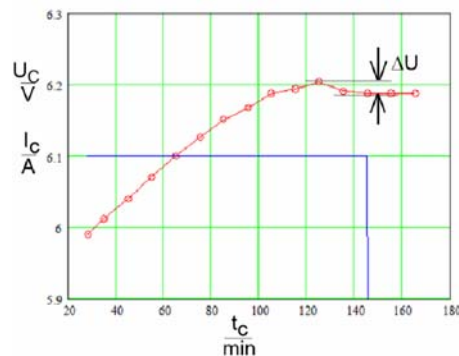

Bild 5.23 Modern chargers offer the charging procedures required for LiPo and NiMH
a) The Ultramat 16S charges/discharges not only NiCd, NiMH and LiPo, four other Li types. The data can be read out on the PC.

b) In delta-peak method, the unit disconnect abrupt the charging current of the NiMH battery when there is a voltage drop of $\Delta U = 20mV$.

In addition, follow the instructions for the safe and careful handling of batteries, [Gie15], [AS19]:
- Only charge LiPos with chargers with balancers designed for this purpose;
- First charges with a maximum of 1C charge current, i.e. 1500mAhr capacity => 1.5A,
  charging with 0.5C to 0.8C is more gentle;
- Do not charge the LiPo battery higher than 4.2V per cell, end the charge of the NiMH battery with the
  Delta-peak method;
- for charging/discharging, the optimum temperature range of the LiPo battery is 20 ... 300C,
  $\rightarrow$ On a cool flying day, keep the battery at "comfortable" temperature until immediately before use;
  $\rightarrow$ let the battery cool down to "hand warmth" before charging;
- If possible, do not use more than 80% of the specified capacity; i.e. set the cut-off voltage of the
  regulator to 3.3V, where possible to 3.4V;
- Do not overload the battery, it must not become hot; from T ≥ 60°C it would be permanently damaged;
- put the battery in a protective bag while charging and never leave it unattended;
- If the battery is to be stored for a longer period - which is already the case after 2 to 3 days - set the
  battery to the charge or discharge to the "storage voltage" 3.8V per cell;
- Do not continue to use the battery after a crash;
- Batteries with a "bloated belly" have developed gas and are dangerous - store and dispose of them
  safely;
- Always dispose of batteries properly: in discharged condition, with insulated contacts, at recycling
  centres.

chemical system	Nikel-Metall-Hydrid (NiMH)	Li-Polymer (Li-Po)
Energy density		
MJ/kg	80 to 61	140 to 153
Wh/kg	60 to 100	130 to 240
typical voltage values at single cell	U_{min} = 1,0 (empty: <1.1V) $U_{ratings}$ = 1,2V; U_{max} = not defined *)	U_{min} = 2,8V (empty: $\leq$ 3,0V) $U_{ratings}$ = 3,7V; $\Delta U \leq$ 50mV U_{max} = 4,2V (full: > 4,15V)
Self-discharge	0,5 …1 % per day 50% per month	
Temperature range	$5^0C \leq \vartheta \leq 30^0C$	$10^0C \leq \vartheta \leq 60^0C$
suitable for	Transmitter	Drive and receiver
Lifetime	500 charge/discharge-cycles *) measured: 1,2V bis 1,55V	150 bis 200 charge/discharge-cycles

charge, Strom $I_C(t)$

|-----I_C=const------------------↑---I_C=0
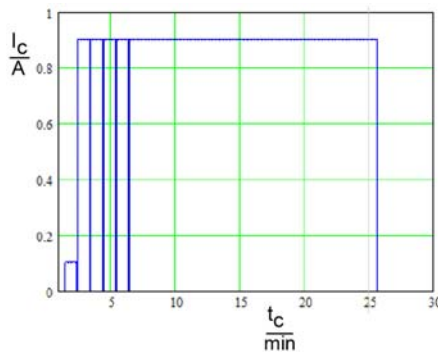
Charging current switched of when ...

|----I_C= const----------→↑--I_C→0--|
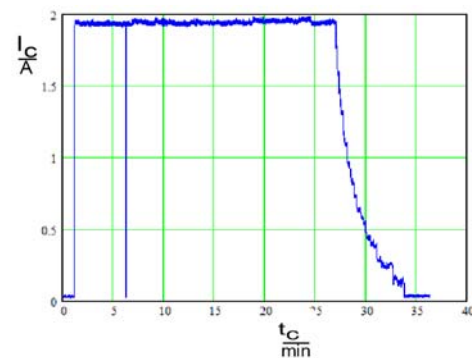
Charging current is reduced to 0A …

charge, Voltage $U_C(t)$
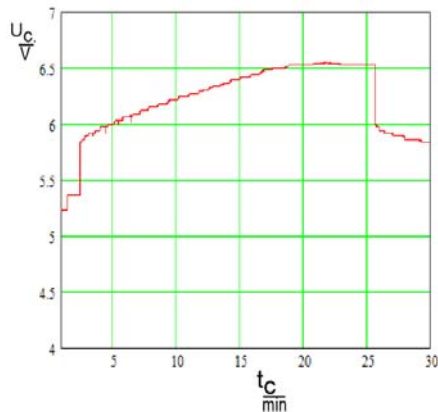
…   voltage drops $\Delta U \geq 20mV$↑
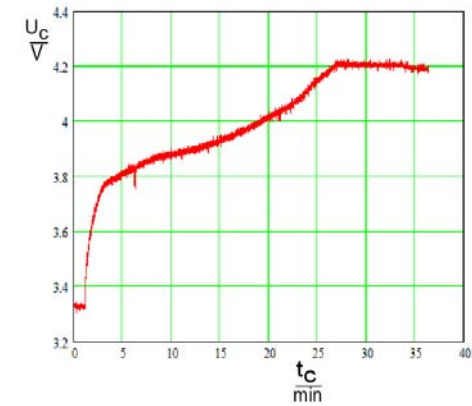
….   when reached ↑ U = U_{max}

discharge, Voltage $U_D(t)$
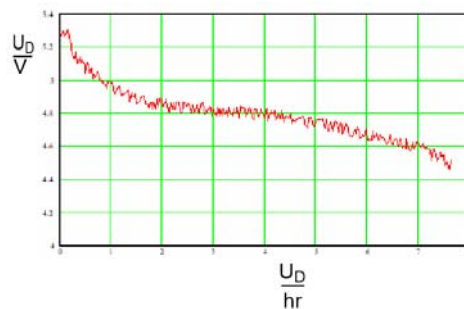
Graupner mx16: 4NH-2000mAhr. The discharge current of Io = 0.2A results in a transmitter operating time of t_D = 7hr
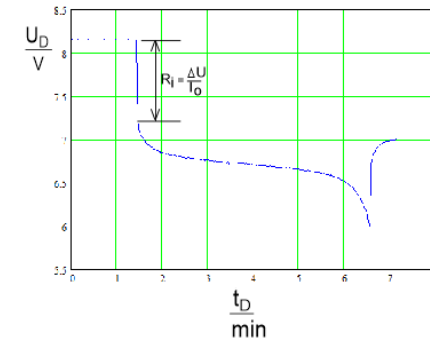
LiPo 2S450mAh; disch. currrent Io= 4A, Ri = 200mΩ, cut-off voltage U = 6V, corresponding to 3V/Zelle

Fig 5.24 Battery types used in model flying and their characteristics

5.3-3 Drive components / motor and propeller

The electric motor is an electromechanical converter: it converts electrical energy (Wh) or electrical power (W) into mechanical energy (Nm) or mechanical power (Nm/s).

The DC motor in the classical sense is shown in Figure 5.25. A magnetic field is built up by the field magnet (permanent magnet or electromagnet). An electromagnet - the armature - is rotatably mounted in this field. It receives its current from a power source via sliding contacts, usually designed as carbon brushes. The current flow in the coil of the armature builds up a magnetic field, which creates forces between the field magnet and the armature. Equal magnetic poles repel each other, unequal magnetic poles attract each other. These repulsive and attractive forces between the magnetic poles cause the armature to rotate.
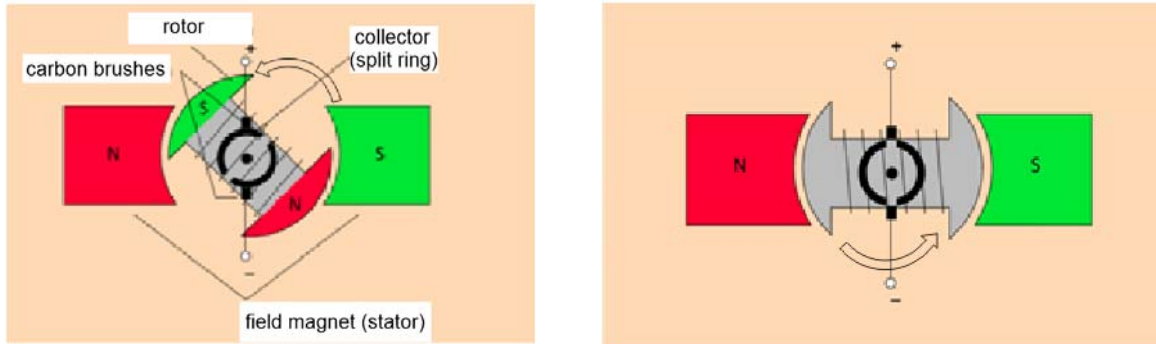
Bild 5.25 Design principle of a classic DC motor [LH]
a) In this position the coil is supplied with current via the collector
b) The armature overcomes such a "gap" position due to mechanical inertia

The process is explained in detail using the motor with only one armature and only one stator: In the illustration Fig. 5.25a), the coil wound continuously over the armature body is soldered with the end near the south pole to the upper left slip ring half, with the end near the north pole to the lower right; the motor rotates to the left. If the armature has rotated so far that the north and south poles are opposite each other, Figure 5.25 b), the slider is between the slip rings and no current can flow through the coil, the movement would stop. Now, however, the mechanical inertia takes effect: the armature "has momentum" and rotates a little further, whereby the other polarity of the current source is connected to the coil ends. The current now flows in the opposite direction, the magnetic field of the armature reverses polarity, the attraction/repulsion force that arises again turns the armature further. This is a mechanical reversal of polarity, also called mechanical commutation. In practice, motors are designed with several field magnets and a collector divided into a corresponding number of segments. In this way, the motor runs "smoothly" and start-up problems are avoided. Note: a brushed motor has only two connections.

In the case of today's brushless motors, Figure 5.26, the control is contactless via a 3-phase voltage signal generated by a controller and shifted by 120deg. The motor would not run with DC voltage. Compared to the classic DC motor, the brushless motor is characterised by a high torque.
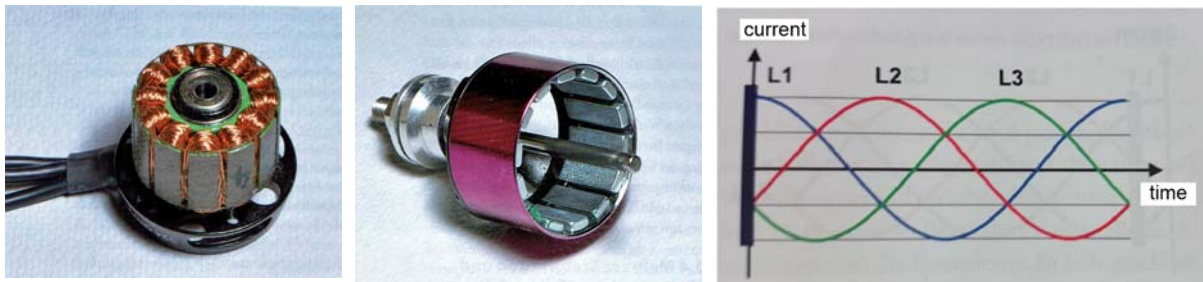
Bild 5.26 Example of a "brushless" external rotor motor [Bü11]
a) The stator consists of 12 armature windings
b) 14 permanent magnets rotate around the windings
c) 3-phase current signal, shifted by 120deg for each of the 3 coil groups.

Figure 5.27 shows the Hacker motor A10-13L used in the Motorglider *Strolch*. The power supply is three-core, as required by the rotating field. The end shield carries the mounting cross, the copper-coloured part including the shaft form the body of rotation. The propeller is rigidly connected to the shaft by a clamping device.


Power range   max.   75W (15 sec)
No-load current at 8,4V Io = 0,39 A
Internal resistance   R = 0,28 Ohm
Idle revs per volt   kv = 1300/Vmin
Weight   20gm
Outer diameter   21 mm
Length   25 mm
Number of poles   12-poliges out runner
Controller recommendation 4A to 7A Brushless
recommended timing 20deg to 25deg

Fig 5.27 Brushless out runner motor A10-13L and technical data specified by manufacturer [Hack19].
Note: a brushless motor needs three connections.

For the mathematical consideration, it is expedient to start from the power balance [MB10]. On the input side is supplied the electrical power $P_{el} = U \cdot I$ (we neglect the "intermediate function" of the controller, which generates the signal backlash for the rotating field from the DC voltage of the battery). At the shaft, the motor "responds" with power components, which are composed of the electrical dissipation power $P_{dis} = I^2 \cdot R$, which may cause the armature winding to become warm, and the mechanical power $P_{mech} = c \cdot I \cdot 2 \cdot \pi \cdot n$:

$$U \cdot I = I^2 \cdot R + c \cdot I \cdot 2 \cdot \pi \cdot n \qquad (5.19)$$

Here U, I: motor voltage in V and current in A, R: ohmic part of the armature winding in Ω, c: Machine constant in Vs, n: rate of revolutions (revs) in 1/s.

The mechanical power, in turn, consists of the power that can be tapped at the motor shaft $P_{sh} = M \cdot \omega = M \cdot 2 \cdot \pi \cdot n$ and of a mechanical power loss due to friction. M describes the torque of the motor in Nm. The friction can be seen from the fact that even for no-load operation, where no load is picked up at the rotating shaft, a no-load current Io is necessary to compensate for the friction losses of the motor. This value for the motor according to Figure 5.27 is $I_o = 0,34A$ at U = 7,4V.

Dividing equation (5.19) by the current I, the speed can be determined with the manufacturer's specification $kv = \dfrac{1}{c \cdot 2 \cdot \pi}$ at a known current, e.g. a measured value, as follows

$$n = (U - I \cdot R) \cdot kv \qquad (5.20)$$

Figure 5.28 a) shows the curve of the speed versus the motor current n(I). The curve begins with the idling speed $n(Io) = n_o = 10450/min$. If we load the motor, e.g. with a propeller, the rate of revolutions (revs) will decrease; a certain revs will be reached at a certain current. If we increase the load so much that the shaft finally stops turning, e.g. because we hold it firmly, the current flowing through the windings reaches its maximum value, the stall current $I_{st} = U/R = 11A$. The useful power in this case is also $P_{sh} = 0$ as in the case of no-load current. This relationship is described by the equation for shaft power

$$P_{sh} = (U - I \cdot R) \cdot (I - I_o), \qquad (5.21)$$

whose graphical course $P_{sh}(I)$ is shown in Figure 5.28 b). Also shown is the efficiency curve, which results from the ratio of shaft power to electrical input power:

$$\eta = \frac{P_{sh}}{P_{el}}$$ (5.22)
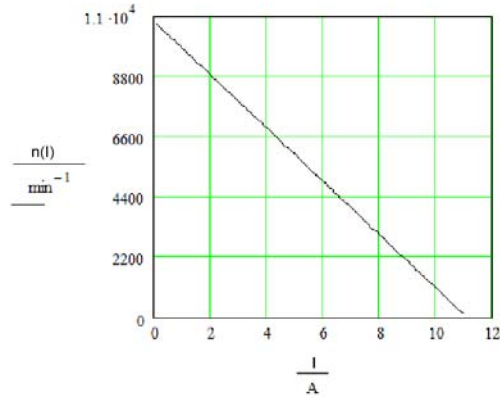
Fig 5.28 a) Curve of revolutions n(I) vs. current I
of the A10-13L; U = 7,0V
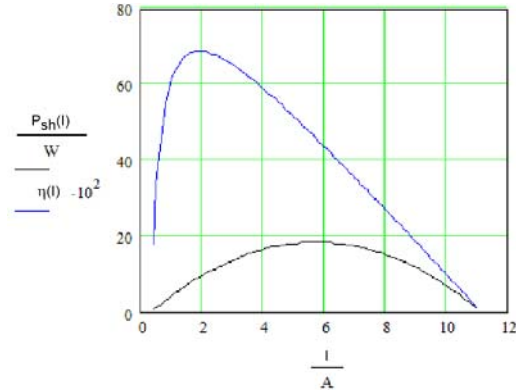
b) Shaft power $P_{sh}(I)$ and efficiency η(I) vs. current
of the A10-13L; U = 7V

The maximum shaft power is here with P_{sh_max} = 18,3W at about $I(P_{sh\_max})$ = 5,7A, the maximum of the efficiency with η_{max} = 0,69 bei $I(\eta_{max})$ = 1,9A.

At this point we need to familiarise ourselves with the propeller. Figure 5.29 shows the analogy of a screw thread to the propelle "thread". We see that with the parameters diameter D and pitch H the blade angle of the propeller is also defined:

$$\beta = a\tan\left(\frac{H}{D \cdot \pi}\right)$$ (5.23)
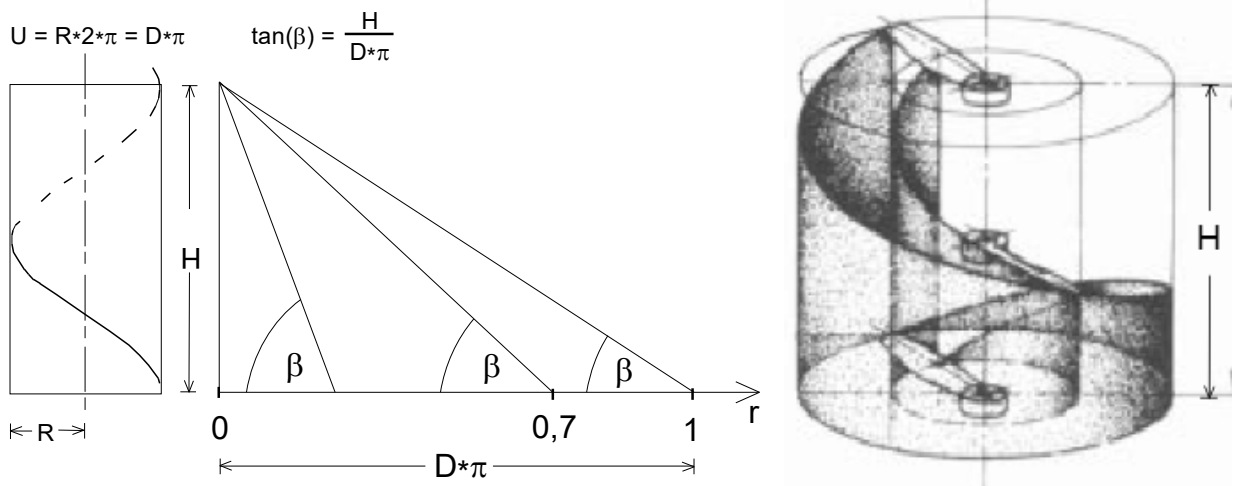
Fig 5.29 a) A helix is created by winding a wedge onto a cylinder of the diametre D. [Sche07].
b) During one revolution the propeller covers the pitch H.

However, this angle remains constant over the radius only for special helicopter rotors. Usually it changes from a large value close to the radius stadion r = 0*R to a very small one at the end of the leaf, i.e. at r = 1*R, Figure 5.29. Therefore, that angle β is considered for the slope H which is measurable at the radius station r = 0.7*R.

You can also imagine - in a very simplified way - that the propeller pushes a column of air of length H backwards per revolution. This makes it possible to estimate the speed at which the column of air leaves the propeller:

$$v_{pr} \approx n \cdot H \tag{5.24}$$

The modelling industry now offers a wide range of propellers: from miniature propellers with a diameter of about D = 3cm up to D = 100cm, the pitch vary within a similar large range. For the aforementioned engine, the literature lists as possible propeller sizes 7″x 4″, 8″x 4″, 9″x 5″ where: 1″ (say: 1 inch) = 2,54cm. These three variables were therefore examined by the author with regard to their effect on the engine during stationary operation.

Bild 5.30: CFK- propeller from Aeronaut, varying in diameter D and pitch H.
From left: DxH = 9"x5"; 8"x4"; 7"x4"

For this purpose, the parameters current consumption, speed and static thrust have been recorded and shown in the diagrams in Fig. 5.31. It can be seen that the values of revolution n(I) fit well into a straight line[5]. In addition to the current values, those for the other parameters of interest can also be read from this, see Table 5.1.
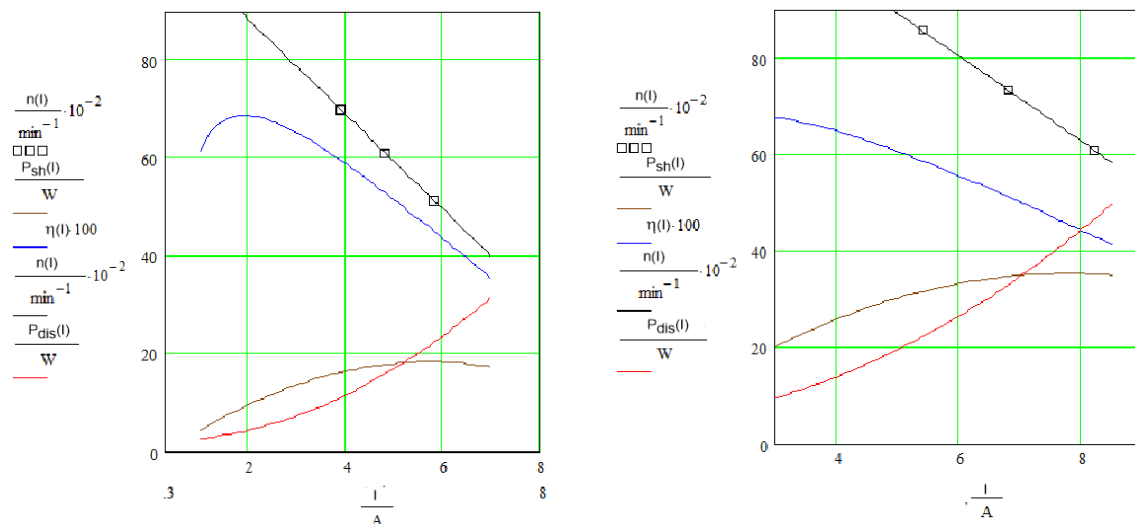
Fig 5.31 a) U = 7V; Measured revolutions values vs. current; Prop 7x4/8x4/9x4

b) U = 10,5V[6]; Measured revolutions values vs. current; Prop 7x4/8x4/9x4

---

[5] This is the case for R_7 = 0,63 Ohm / kv_7 = 1540/Vmin; R_10 = 0,66 Ohm / kv_10 = 1335/Vmin
[6] Instead of 7,4V (2S) und 11,1V(3S) the values 7V and 10,5V are common as test voltages

The assessment of these values shall be made on the basis of a practical application: it shall be estimated whether the motor is suitable for the motor glider *Strolch*, Figure 5.37. Example 5.3 will show that a shaft power P_{sh} = 15W is sufficient for this.

In table 5.1 we see that for a 2S battery (7V) the 8x4 or 9x5 propeller would be a good choice: the required shaft power is slightly exceeded and the power loss remains within limits with max. 16W to 22W. If we were to use a 3S battery (10.5V), a 7x4 prop would already deliver twice the required shaft power of ≈30W, but also with a larger electrical power input P_{el} = 54W. However, this value of around 70% would still be well below the maximum permitted, see the information in Figure 5.27.

Propeller	7x4	8x4	9x5	7x4	8x4	9x5
	U = 7V			U = 10,5V		
param						
n/min^{-1}	6984	6086	5143	8579	7350	6103
I/A	3,9	4,8	5,8	5,4	6,8	8,2
P_{el}/W	27,3	33,6	40,6	54	68	82
P_{sh}/W	16,24	17,8	18,32	31,7	34,8	35,5
η/%	59,5	53	45,12	58,7	43,1	45,1
P_{dis}/W	11,1	15,8	22,3	22,3	33,2	46,6
F_T/gm	120	160	200	200	250	300
F_T/N	1,18	1,57	1,96	1,96	2,45	2,94
β/deg	10,31	9,04	10,03	10,31	9,04	10,03
v_{pr}/m·s^{-1}	11,6	10,1	10,7	14,3	12,25	12,72

Table 5.1 Measured values for speed n, current I and static thrust F_T, which were obtained when the A-13L was loaded with the above-mentioned propellers in stationary operation. Values for power and efficiency were from the diagrams Figure 5.31 a) and b).

Bild 5.32: *peakTech_1560*, Adjustable power supply unit 0-32V/30A as "battery replacement'

However, the effort for such a metrological investigation is not small: a power supply unit, which in the present case supplies adjustable voltages 7V/10.5V and output currents up to 15A, figure 5.32, as well as a reliably working tachometer, are prerequisites.

But can you also find the right propeller by calculation? To do this, you need to know how much power a propeller can absorb. Aeronaut publishes a diagram from which the measured values $P_{pr}(n)$ for different sizes of their propeller families can be taken, see figure 5.33. One can see, for example, that the power P_{pr} = 50W can be absorbed by a propeller 9x5 at a speed n = 7000/min; a propeller of size 10x7, however, manages this at n = 5900/min. The larger the propeller diameter D, the more shaft power it can absorb. For the concrete example, however, we also see a sufficiently exact match with the shaft powers P_{th} highlighted in green in table 5.1: for the propeller sizes 8x4 with n ≈ 6300 and 9x5 with n ≈ 5200, values Ppr ≈ 20W can be estimated from the graph.

The logarithmic ordinate scaling of the graph now already indicates a non-linear dependence on the speed. Analytically, this becomes clearer: for the power consumption of a propeller at static thrust, the following relationship applies [Sch03]

$$P_{pr}(n) = c_p \cdot \rho \cdot n^3 \cdot D^5 \tag{5.25}$$

Here, c_p: power coefficient of the propeller, ρ: air density, n: Speed and D: Diameter of the propeller. We see that the speed is included in the power consumption to the third power, the diameter even to the fifth power.
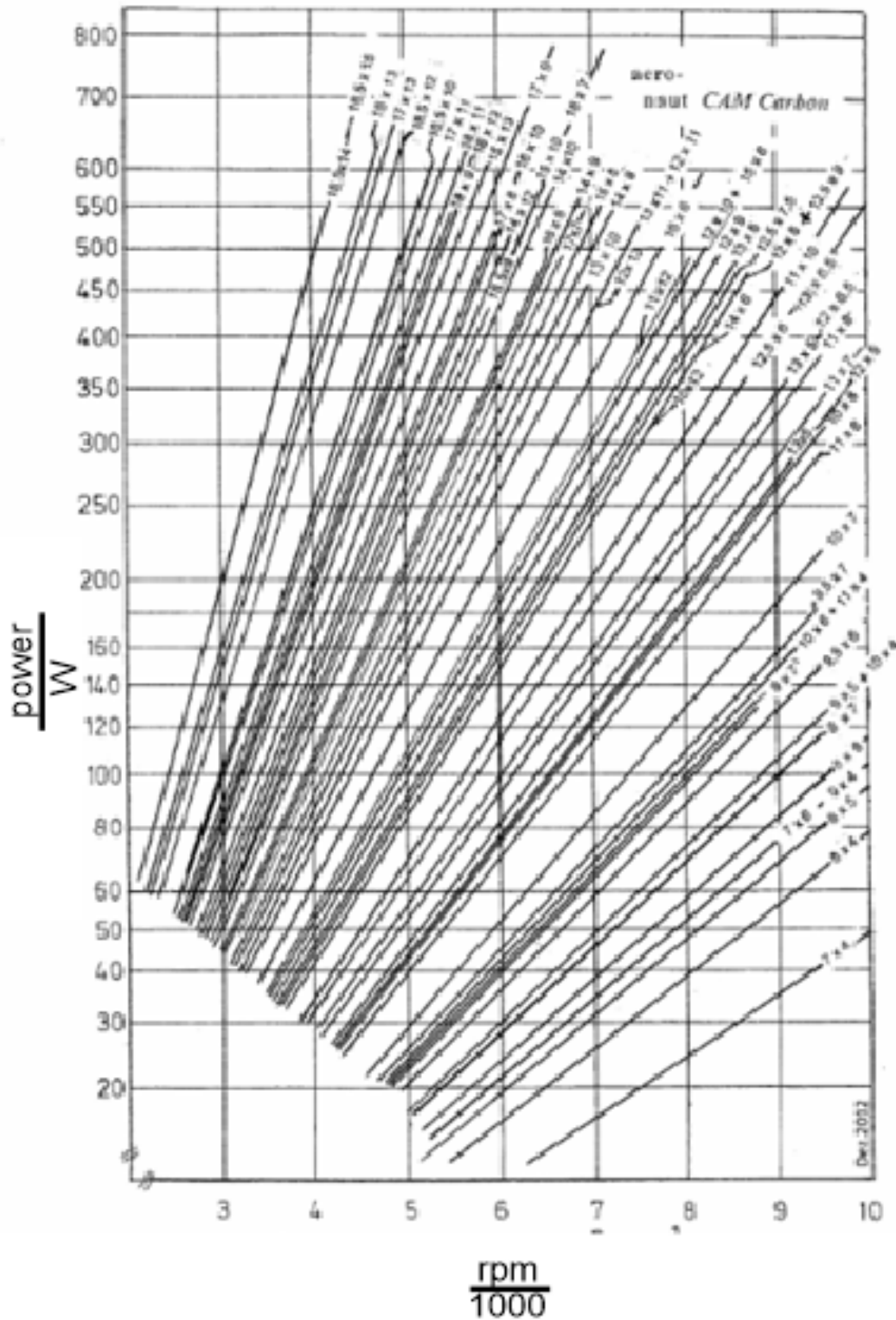
Fig 5.33: On the power consumption of propellers $P_{pr}(n)$ according to [Aer19]

For the Aeronaut propeller family there is the approximation formula in the same bibliography

$$c_p \approx 0{,}833 \cdot \frac{H}{D} - 0{,}0116 \tag{5.26}$$

so that with (5.26) in (5.25) the power consumption $P_{pr}(n)$ can be calculated.

The different propellers installed on our example engine will now each take up a speed that results from the balance of offered shaft power P_{sh} and absorbed power P_{pr}. Because the speed of the motor and propeller is the same,

$$n_w = n_{pr},$$

and because also applies $\qquad P_w = P_{pr}$

$$(U - I \cdot R) \cdot (I - I_o) = c_p \cdot \rho \cdot n^3 \cdot D^5$$

one can also calculate the speed for which this equation applies. That is, the zeros of the 3rd degree function must be determined in order to find those values of the current $I(n)$ for which the speed n is equal to:

$$(U - I \cdot R) \cdot (I - I_o) - c_p \cdot \rho \cdot \left[(U - I \cdot R) \cdot kv\right]^3 \cdot D^5 = 0 \tag{5.27}$$

The solution can only be achieved numerically, advantageously again with the help of a mathematical program. In the graphical representation, the current zeros result as intersections of the characteristic curves of output shaft power P_{sh} and input propeller power P_{pr}, see Table 5.2 and Figure 5.34. With the help of these power values, values for the thrust force F_T can now also be estimated:

$$F_T = 0{,}67 \cdot \sqrt[3]{\frac{\rho}{2} \cdot \pi \cdot D^2 \cdot P_{sh}^{\,2}} \tag{5.28}$$

Compared to the measured values, the calculated ones meet with useful low tolerances. However, one must not forget that the essential basis for this was laid with the measured values n(I), which resulted in correction values for kv and R, see footnote 5.

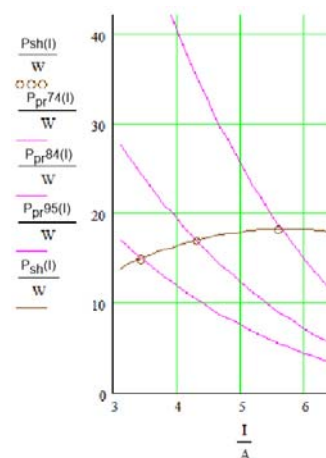| Prop param.	calculated values U=7V			difference-values U=7V		
	7x4	8x4	9x5	7x4	8x4	9x5
				meassured − calculated		
n/min^{-1}	7443	6601	5297	459	515	154
Δ				+6,6%	+8,5%	-3%
I/A	3,43	4,3	5,6	0,47	0,5	0,2
Δ				12%	10%	3,4%
P$_{sh}$/W	15	17,0	18,3	1,24	0,8	0,02
Δ				7,6%	4,5%	9,1%
F$_T$/N	1,61	1,75	2,17	0,43	0,18	0,21
Δ				26%	11%	11%

Tabelle 5.2 Values calculated from Eq(5.25) and their deviation from the measured values listed in Table 5.1

Fig 5.34: The propeller curves $P_{pr}(I)$ intersect the power curve $P_{sh}(I)$

It has now been pointed out several times that the thrust values are those for static thrust. These values are interesting for the operation of aerobatic models, which have the so-called torquing or hovering in their programme, or for the operation of drones, Figure 5.35. In these cases the thrust $F_T \geq (2...3)*F_w$ should be designed, [Bü10].

Fig 5.35 a) Here A. Scheffler "hangs" his aerobatic model on the propeller - for that the static thrust is required

b) The DJI Mavic Mini drone is designed as a quadrocopter see the [DJ20]

The situation is different with a fixed-wing model. In flight, the difference between the jet velocity v_{pr} generated by the propeller and the airspeed v is smaller, and thus the thrust force F_T is also smaller than when stationary. In the literature, the degree of progress J is used in this case, a factor that relates the ratio of the airspeed v to the circumferential speed of the propeller v_u [Sche07], [Hep18]:

$$J = \frac{v \cdot 60}{D \cdot n} \tag{5.29}$$

The diameter D is determined from a widely scattering range of $0.4 \leq J \leq 0.8$. Further dimensioning methods are presented in section 7.5 / Selection of the drive.

Here we will first show that it is also possible to calculate with measurement results obtained from static measurements, as long as the flow at the propeller does not break off, i.e. the propeller angle of attack remains $\beta \leq 12$deg, compare Figure 5.2b and Table 5.1.
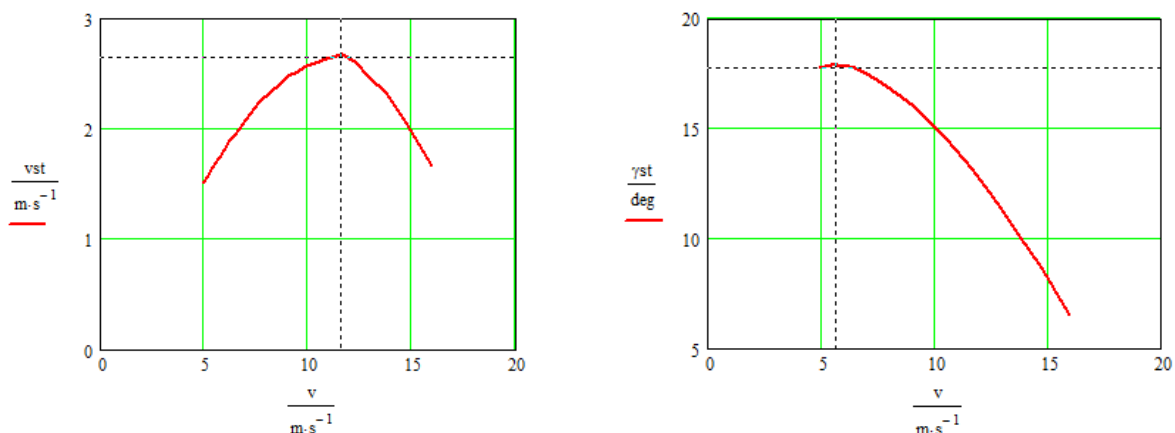
Fig 5.36 Climbing polar curve of the 300g model Strolch. With a thrust of $F_T = 1$N it reaches
a) a <u>max rate of climb</u> $v_{cr} = 2,7$m/s at v = 11,6m/s;   b) a <u>max angle of climb</u> $\gamma_{cr} = 18^0$ at v = 5,7m/s;
   the angle of climb is $\gamma_{cr} = 13^0$ and the wing-angel   the rate of climb is $v_{cr} = 1,7$m/s and the wing-
   of attac is $\alpha = -2,8^0$.   angel of attac $\alpha = 4^0$.

Measurements on two projects worked on in connection with GTA_Modellflug show that for motor gliders of the class discussed here, a halving of the static thrust F_T can well be assumed for the thrust value in flight, see also sections 8.1 and 8.2 in the chapter *Selected Topics*. With the thrust specification $F_T = 0.5*1.96N$, the angle of climb γ_{cr} and the rate of climb v_{cr} are calculated for the Strolch model according to chapter 5.2-3 *Climb*. It can be seen that the maximum values are reached at very different airspeeds v of the model, figure 5.36; these must be flown via elevator trim.

Climbing measurements finally confirmed the calculated prediction of the required rate of climb v_{cr}, see Figs. 5.37. A practical application of the topic is described in Example 5.3.
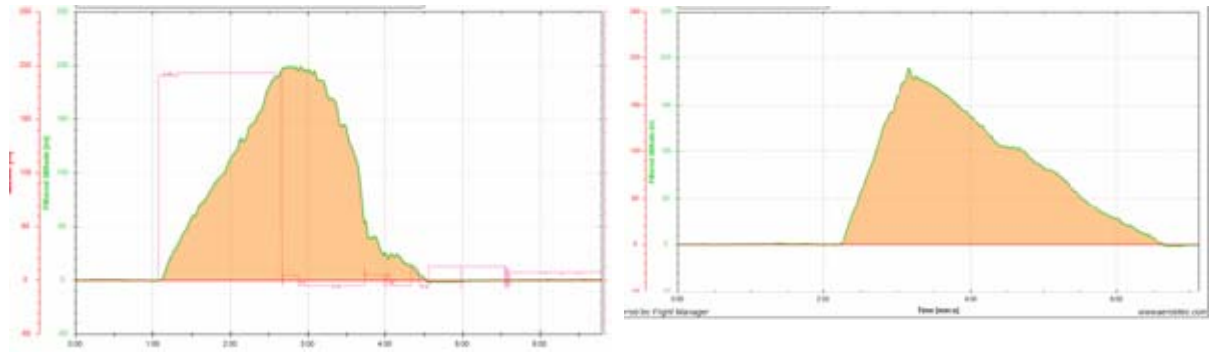
Fig 5.37 Climb performance of the *Strolch* with 2S battery. Onboard measurement ALTIS 4+   [Alt20]
a) Propeller 8x4 givs v_{cr} = 2,1m/s   b) Propeller 9x5 givs v_{cr} = 3,4m/s
With the *Aerobtec Flight Manager* the stored data can be read out

Fig 5.37c)   Motorglider Strolch with Graupner mx16 R/C gear in instructor-pupil function.

5.3-4 Drive components / speed controller

This electronic component generates the aforementioned signals for the rotating field. A microprocessor controls the output stages in such a way that current flows through 2 groups of the 3 armature windings. Voltage signals for the speed and position of the armature are obtained from the 3rd group, which lead to a phase shift of the current signals in case of deviations. From this point of view, it is justified to speak of a speed controller.

When selecting the controller, it is important to take into account the requirements of the motor. For example, the motor should require a maximum of 80% of the continuous current specified for the controller. If, on the other hand, the model aircraft is to be flown at "half throttle" for a longer period of time - in the so-called partial load range - it must also be taken into account that this produces the greatest power loss in the controller output stage, i.e. the greatest heat generation. In this case, you should choose a controller with a nominal current that corresponds to twice the maximum motor current.
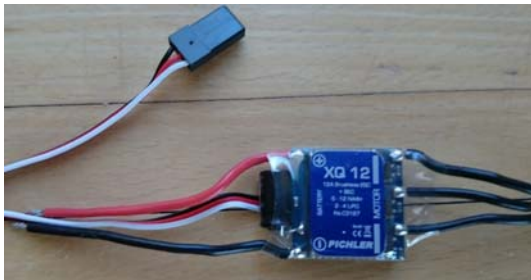
2 bis 3 Lipo
Imax_continous = 12A
Imax_short burst = 16A
BEC 5V/1A
programmable via transmitter or XQCard
LiPo-Abschaltspannun 3,0/ 3,2V einstellbar
Masse 5g

Bild 5.38 Brushless-Regler XQ12 und seine Technischen Daten [Pi16]

In most cases, the controller also supplies the 5V voltage for the receiver, referred to as the BEC output (**B**attery **E**liminator **C**ircuit). Here, too, there are power considerations to take into account, hardly because of the few mA for the receiver, but rather the servo currents.

If only two servos with a total current of ≤ 0.5A are to be supplied, then in the case of a linear LDO (**L**ow-**D**rop-**O**ut) voltage regulator, even with a 3S battery, the power loss of ≈ 3W remains within a tolerable range. When utilising the maximum current of 1A - as is possible with the controller mentioned here - a 3S battery, however, already produces 6W of power loss, which can cause the tiny IC to become hot. It is not without reason that for larger models (e.g. a glider with 6 servos) the power supply for the receiver is employed with a separate - usually NiMH - battery recommended. In the case of the XQ12 controller, however, a switching regulator is installed which, due to its principle, only generates minimal power loss.
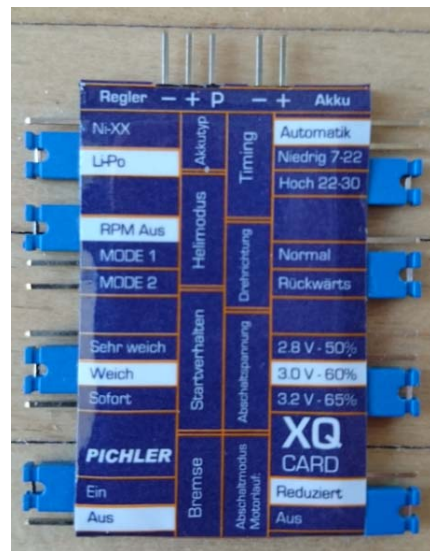
Bild 5.39 Programming card [Pi16]

Other interesting features of a controller are:
- **Selectable cut-off level** for the drive battery, for example 3.4V/cell for Lipo
- **Reversing the polarity of the motor running direction**, important if the controller-motor wiring has already been completed.
- Adjustment of an **engine brake** to avoid "free spinning" of the propeller after switching off.
- **Timing in degrees** ≈ 2xnumber of poles of the motor; Example: Hacker: 12-pole external rotor ⇒ 24deg ; recommended timing: 20deg to 25deg

These parameters can be set (programmed) for each controller via the transmitter, whereby a prescribed sequence of (mostly throttle) stick movements must be adhered to - the controller acknowledges with beeps of varying lengths. Of course, it is more convenient to use a programming card, such as the XQ card from Pichler in Fig. 5.39; the function is self-explanatory and you do not have to "bend your ears" to catch every single note.

Example 5.3
A popular competition task of our club was borrowed from the UHU Cup, a model aircraft competition of DAeC youth competitions: The climb phase of a motor glider with a maximum climb time of t_{cr} = 60s is followed by a glide phase, which is to be completed with a flight time of t_{sr} = 180sec along a landing line. The altitude to be reached is equal to the altitude from which the glide should follow:

$$v_{cr} \cdot t_{cr} = v_{sr} \cdot t_{sr}$$

This results in the rate of climb to

$$v_{cr} = v_{sr} \cdot \frac{t_{sr}}{t_{st}}$$

Assuming a descent rate of vsi = 0.5m/s, the rate of climb must then be at least

$$v_{st} = 0,5 \cdot \frac{m}{s} \cdot \frac{180 \cdot s}{60 \cdot s} = 1,5 \cdot \frac{m}{s}$$

According to Eq. (5.11), the necessary propeller output power results in

$$P_{out} = 0,3 \cdot kg \cdot 9,81 \cdot \frac{m}{s^2} \cdot 2 \cdot \frac{m}{s} \approx 6 \cdot W$$

With an assumed propeller efficiency of ηpr = 0.4, a shaft power P_{sh} = 15W is required. The values for shaft power measured in table 5.1 confirm this estimate.

5.3-5 Drive components / selection criteria for the model aircraft drive system

Rule _1: One should follow the suggestions of the engine manufacturers. As an example, Table 5.3 gives details for the Hacker A10 series, of which the A10-L13 is covered in detail on the previous pages.

Motor	A10-S		A10-L			*Motor*
Leistungsbereich	max. 55W (15sec.)		max. 75W (15sec.)			Powerrange
E-Segler	bis 300g / up to 10,5oz		bis 500g / up to 17,5oz			Electric-Sailplane
Sport- und Scale	bis 250g / up to 8,8oz		bis 400g / up to 14oz			Sport and Scale
Kunstflug und 3D	bis 170g / 5,9oz		bis 200g / up to 7oz			Pattern and 3D
Windungszahl	12	15	7	9	13	*Turns*
Empf. Prop-Größe	6x3	7x4	7x3,5	8x4,3	8x4,3	Recommended Prop Range
Zellenzahl	2 LiPo	2 LiPo	2 LiPo	2 LiPo	3 LiPo	No. of Cells
zulässiger Dauerstrom [A]	4A	4A	5,5A	5,5A	7 A	Continuous Current [A]
kurzzeitiger Strom (15Sec) [A]	6A	6A	8A	8A	9 A	Max. Burst Current (15s) [A]
Leerlaufstrom (Io) @8,4V [A]	1,0	0,63	1,1	0,72	0,39	Idle Current (Io) @8,4 V [A]
Innenwiderstand (Ri) [Ohm]	0,185	0,289	0,11	0,18	0,28	Resistance (Ri) [Ohm]
RPM/Volt (Kv)	2900	2320	2200	1700	1200	RPM/Volt (Kv)
Rückwandbefestigung komplett	✓					Backmount complete
Prop-Adapter	APC and GWS					Prop-Adaptor
Befestigungsschrauben	☐					Screws

Tabelle 5.3 Manufacturer's instructions for A10 motors

Rule _2: One must be clear about the type of model for which the drive is to be configured. For this purpose, findings from formulae (5.24), 5.28) and table 5.1 can also be used:
*an increased diameter D results in an increased thrust F_T;
*an increased pitch H results in an increased propeller jet speed v_{pr}.

In a series of contributions by Müller [Mü14], observations on parameters of drive configurations of different model types are recorded, which are explained below. They are also given in short form in Tab 5.4.

<u>Motor glider</u>: Model climbs with motor assistance to the height where thermals are expected. After switching off the motor, the model becomes a pure glider and remains in the air for a longer or shorter time, depending on the thermal situation. The engine running time is low compared to the gliding time; the engine can cool down again during the gliding phase. Under these circumstances, it is permissible for the model to climb with the specified short-term (usually 15sec) maximum current.

<u>Parkflyer</u>: Light and small model (b ≤ 1.20m), which is controlled at low altitude in circles and loops. The motor usually runs for the entire flight time (10...15)Min. Here the drive must be configured so that the power loss remains small enough so that the motor does not overheat, or it must be cooled accordingly. Motor temperatures of 80ºC can damage the magnets. But the power dissipation/heat generation of the controller must also be taken into account here, because especially with this type of model the partial load operation described above is predominant - plumes of smoke have already been observed on the flying model.

<u>Trainer</u>: Model with a larger wingspan (b ≈ 2.50m), with which either thermal flight or simple aerobatics are practised. In the latter case, attention must also be paid to possible heating.

<u>3D aerobatics</u>: the motor must be able to pull the model vertically upwards in certain manoeuvres (300W/kg) or to torqued; in the latter case it must be noted that the cooling by the airstream is missing. Since the downward manoeuvres are mostly flown at idle, the motor will not reach its power limit on average.

<u>Glider tow</u>: Model with powerful engine and high static thrust, which can take off after a short taxiing time.

<u>Pylon racing</u>: a model designed for this purpose must be able to fly fast, its drive must still generate sufficient thrust at high speeds. This is achieved with a large pitch propeller, e.g. 5x5; speed pilots calculate with airspeed 85% of jet speed; $v \approx 0.85 * v_{pr}$.

<u>Drone</u>: For good-natured controllability, as required e.g. for camera flights, the ratio of thrust to weight force $F_{th}/F_w = 2:1$ is recommended. For drones with aerobatic characteristics, the ratio should be 3:1 or slightly higher.

Parameter / model type	power to model mass W/kg	static thrust to weight force F_T/F_w	climb rate v_{sr} m/sec	prop sped v_{pr} m/s	propeller pitch to Diameter H/D
Parkflyer	100	≥ 0,4	0,5…1	≤ 15	
Motor glider	140 ..170	≥ 0,4	2…3	10…25	0,6…0,8
Hotliner	500…1500		5…10	≥20	1; i.e. 16x16
Trainer	100 …150	≥ 0,6	3…5	14…25	
dynam.acrobatic	250	≥1,2		15…30	0,6…0,8
3D-acrobatic	350…400	≥ 2	5	14…22	0,5; z.B.13x6,5
Seglerschlepp	3000		3..4		
slow oldtimer	200				≤0,3; z.B. 13x4
Pylon racing	250…600		2	≥ 40	1; z.B. 5x5
Drone		≈ 2			small

Tabelle 5.4 Statistically recorded parameters on drive configurations [Mü14]

6.0 Strength

Material	Density ρ ($\frac{gm}{cm^3}$)	tensile strength σ_{ts} ($\frac{N}{mm^2}$)	compressible strength σ_{ps} ($\frac{N}{mm^2}$)	bending strength σ_{bs} ($\frac{N}{mm^2}$)	E-modulus E ($\frac{10^3 N}{mm^2}$)	breaking length σ_{bl} (km)	ultimate strain ε_{us} (%)	temperature coefficient T_C (ppm)
Styropor	0.015 … 0.02							
Balsa soft middle hard	0.6 … 0.15 … 0.25 0.25 … 0.4			8 …12.5 12…20 20…40	2 5 8	12 15 17		pos.
Pine middle hard	0.4 … 0.6 0.6 … 0.8	70 … 100 100 …150		40…60 60..200	10 20	15 18	0.7	pos.
Plywood				70	8		1	pos.
Polyester resin	1.24	50…70		60			1…3	pos.
Epoxy resin		70…90		80			1…4	pos.
Glass fiber roving fabric	1.7…2.5	800…1000 300		300…450 150…200	30…50 20	50…70	2.5 3.5	pos.
Carbon fiber roving fabric	1.4…1.7	900…1200		459…650	90…130 40	60…50 40	1 1.3	neg.
Synthetic fiber roving fabric	1.25…1.4	130000	40000		60…70	75…65	2.5	
Aluminium AlCuMg2 2024-T4	2.8	300		100	70	16	20	pos.
spring strip steel 55SiMn7	7.8	1320		650	200	25…30		pos.

Table 6.1 Parameters of materials that are interesting for model aircraft construction marked in grey. values apply for the resin composite

conversions: $10 MPa = \frac{1kN}{cm^2} = \frac{10N}{mm^2}$

6.1 Strength parameters

In addition to the materials traditionally used for model aircraft construction, such as balsa and pine wood as well as covering paper, today covering foil, products made of glass and carbon fibres (fabrics, rovings), polyester and epoxy resin as well as foams (PUR, expanded polystyrene/styrofoam) are common. Most of the materials were used in the construction of gliders and large aircraft. Some materials have also been "discovered" by model sports enthusiasts from other fields for their needs. The covering foil was even developed especially for model aircraft construction.

Section 6.2 deals with the individual load cases on the flight model. In order to use the materials sensibly against these loads, it is good to know their most important properties. They are listed in table 6.1. Here are a few remarks: The *density* ρ gives information about the mass contained per unit volume; it is given in gm/cm^3 ($1gm/cm^3 = 1kg/dm^3 = 1000kg/m^3$). The *tensile strength* indicates at which tensile stress the material loses its strength. The *compressive strength* indicates the compressive stress at which the material is compressed. The unit of measurement for both quantities is N/mm^2 (we apply the force of 1N when we hold a mass of exactly 101.97gm in our hand and do not drop it). As can be seen from the table, wood can be loaded about twice as much in tension as in compression.

If a workpiece clamped on one side, e.g. a wooden beam, is loaded with a weight, it bends. This bending causes a stress σ in the beam, it is maximum in the edge fibres: one as tensile stress (above), the other as compressive stress (below), see Fig.8b. The *bending stress* σ_b now gives an indication of the maximum load-bearing capacity σ_{bmax} at which the bent workpiece breaks or bends (yielding). In terms of value, it lies between tensile and compressive stress. The still *permissible bending* stress is lower by a safety factor, for example $\sigma_{b\_perm} = \dfrac{\sigma_{b\max}}{1.5}$. The unit of measurement is again N/mm^2.

6.2 Load cases

In a first approximation the wing[7] counteracts the weight force F_w of the model with its lift F_L. In the case of stationary gliding flight, this weight force is identical with the gravitational effect $F_w = m*g$. Other conditions arise in manoeuvre flight (turning, interception). In the case of a glider model, there is also the case of a rope take-off, see Fig 6.4.

First, the expected manoeuvre loads are to be estimated. If a model flies a loop with the speed v, the lift force F_L must compensate for the *centrifugal force* F_C in addition to the weight force F_w, Figure 6.1:

$$F_L = F_W + F_C$$

Compared to stationary gliding flight, the lift force is therefore higher by a certain factor, this is called the load factor or load multiple lv:

$$F_L = lv \cdot F_W$$
$$lv \cdot F_W = F_w + F_C$$

With $F_C = \dfrac{m \cdot v^2}{r}$ we obtain

$$lv = 1 + \frac{v^2}{r \cdot g} \tag{6.1}$$

---

[7] To be precise, the wing mass m_w does not play a role in load multiplier considerations, since the wing is self-supporting, so to speak. However, the total model mass is often used

While the "entry" velocity v can be determined according to Eq. (5.3), we have to estimate the looping radius r. An example may give a first impression of the size: v = 10m/s, r = 5m. We get

$$lv = 1 + \frac{\left(10\frac{m}{s}\right)^2}{5m \cdot 9.81\frac{m}{s^2}} = 3{,}04$$

The wing must therefore withstand a weight force of the model FG that is greater by factor 3 without breaking.
However, we can also determine the load that arises when the model is intercepted with the maximum possible lift F_{Amax} from a steeply inclined flight path. In this case

$$lv = \frac{F_{L\max}}{F_W} \tag{6.2}$$

and with the maximum lift corresponding to Gl. (5.1) $F_{Lmax} = (\rho/2)*v^2*S*c_{lmax}$ erhalten wir

$$lv = \frac{\rho}{2 \cdot g} \cdot \frac{c_{l\max}}{\frac{m}{S}} \cdot v^2 \tag{6.3}$$

If we now use Eq(5.3) for the velocity v that the model would assume at a selected clmin, we obtain

$$lv = \frac{c_{l\max}}{\sqrt{c_{l\min}{}^2 + c_{d\min}{}^2}} \tag{6.4}$$

The relationship (6.3) is evaluated in Figure 6.2 for different area loads mass/S_w and for a c_{amax} = 1.1. It can be seen that, for example, with a surface load of 40g/dm2 a load multiple of l_v = 13 occurs, if a model flying with speed v = 28m/s in path inclination flight is intercepted with c_{lmax} = 1.1. Or more clearly: for a model with a fuselage mass of m_f = 1.2kg, about 13*1.2kg*9.81m/s2 = 153N "pull" on the wing-fuselage connections when you pull it around from a nosedive with c_{lmin} = 0.084 by "fully pulling" the elevator.
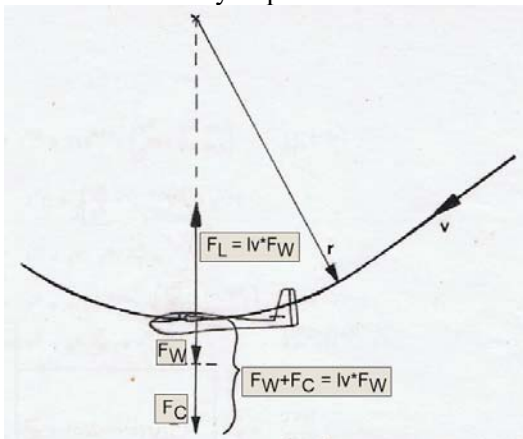
Fig 6.1: When intercepting, the airfoil must in addition to the weight force F_W also absorb the centrifugal force F_C
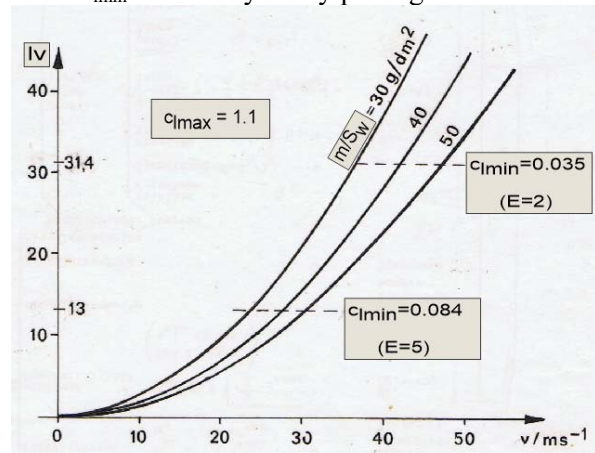
Fig 6.2: Load multiple lv, which arises during the interception on c_{lmax} of a model with speed v.

However, this situation is present in the turn in F3B speed flight (four distances, i.e. the glide ratio is at best still ε = 1:5, i.e. E ≈ 5). If we also consider the F3B competition practice of accelerating the model in a dive immediately before releasing the winch, we can expect load multiples of lv ≈ 40 according to figure 6.2!

But the wing is also loaded in the classic launching with cable (towline), see the following pictures.
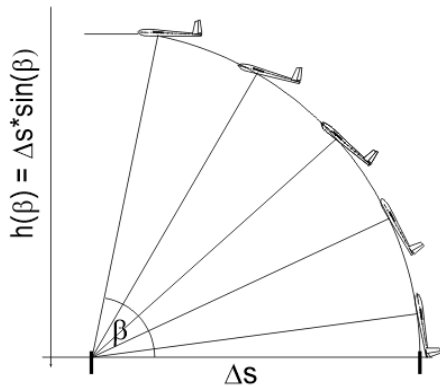
Fig 6.3a) Towline high launch. Assumption: the towline is anchored and the wind drives the model upwards. Theoretically achievable is $h_{max} = \Delta s \cdot \sin(\beta)$

Fig 6.3b) High launch of RES models with bungee cord. Comparison flying 2020, mfcR airfield.
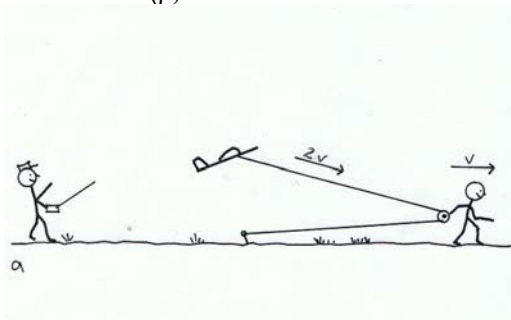
Fig 6.4a) Hand tow with loose pulley. If the person is running at speed v, the model is moved at 2*v. [La91]
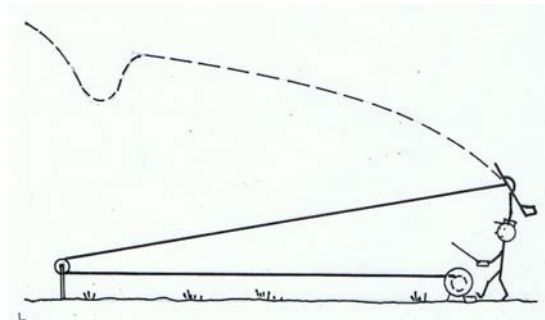
Fig 6.4 b) Winch launch with fixed pulley. In contrast to man-launched gliding, the winch here is in the pilot's position.

From considerations of the acting forces and velocities, Figs. 6.5a, b [Ho81], [La91], the following result for the lift force F_L to be applied by the wing, which must essentially be absorbed by the spar, and for the model velocity

$$F_L(\beta) \approx F_W + F_S \cdot \sin(\beta) \cdot \frac{\cos(\beta)}{\cos(\delta)} \quad (6.5)$$

$$v(\beta) = v_S \cdot \frac{\cos(\beta)}{\cos(\beta - \delta)} \quad (6.6)$$
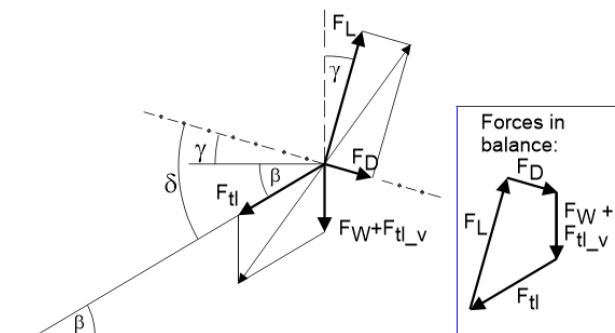
Fig 6.5a): On the effect of tensile force in the towline launch. F_{tl_H}, F_{tl_V} : horizontal and vertical components of the tensile force F_{tl} , [Ho81].
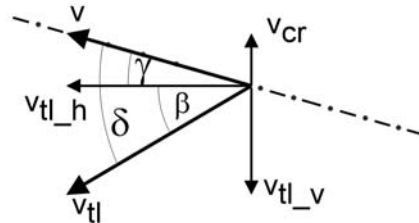
Fig 6.5b): Decomposition into velocity vectors [La91]. δ = const, = 65deg: Angle between launch hook and fuselage longitudinal axis

During the take off process the towline angle β changes . Figures 6.6a, b show how the lift force F_L and the model velocity v change depending on this. Here F_{tl} is the estimated or measured towline pull force. The lift force F_L reaches its maximum value ($dF_L/d\beta = 0$) for a towline angle $\beta \approx 45^0$. Incidentally, the author still remembers well the sudden exertion required of the person dragging after the first few - still fast-running - metres!
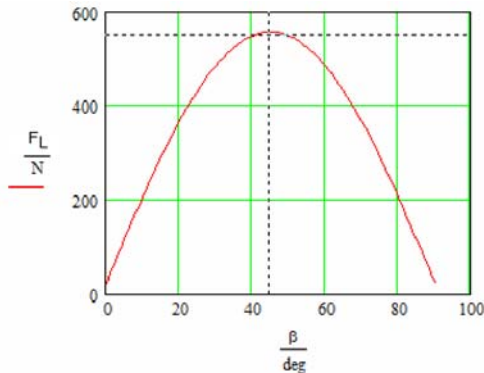
Fig 6.6 a): Course of the lift force F_L over the towline angle β. At maximum, the wing must withstand $F_L = 557N$ if $F_{tl} = 400N$.
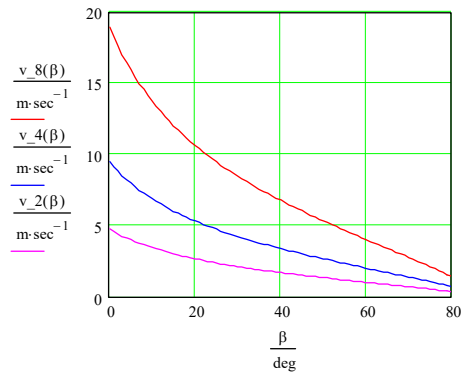
Fig 6.6 b): Model speed v over the towline angle β when the towline is pulled with v = 2m/s, 4m/s and 8m/s

For the example of the F3J model RS3 developed in the mfcR, Figure 6.7a, the data gives:
$F_W = 2.4kg*9.81m/s^2 = 23N$, towline pull force $F_S = 400N$ (see measured value in Figure 6.7b), $\delta = 65deg$, the maximum lift force of 557N (corresponding to lv $\approx$ 24). The fact that the buoyancy force exceeds the towline pull force can already be seen qualitatively in Fig. 6.5a): the pointer length for the lift force F_L is clearly greater than that for the towline pull force F_{tl}. This is due to the different angles at which both forces act on the centre of gravity.

However, common competition practice deviates greatly from the classic high take-off model. For example, many F3J pilots do not steer their model upwards in a straight course, but build an S-shaped course into the flight path. And with this "sideways turn" the perlon towline is stretched again, which ultimately translates into additional height gain. In the force curve, this manifests itself in a "peak halfway", Figure 6.7b. The purpose of the measurement was to determine the maximum towline tensile force.

Fig 6.7a): F3J model RS3, which was designed and built with the significant participation of young club members of the mfcR; m = 2,4kg, S_W = 68dm^2 [JW04]
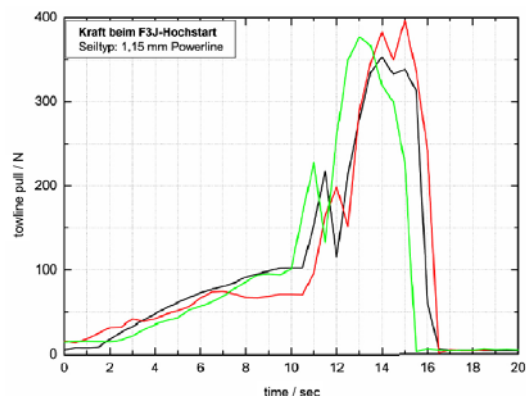
Fig 6.7b) Measured towline pull F_{tl}, three launching operations according to Fig. 6.4a). The load cell is mounted between the ground anchor and the towline [JW04]

6.3 Forces in the wing

Now the consequences resulting from the estimated loading cases for the required wing strength are to be considered. Assuming a symmetrical and quasi-rectangular lift distribution, Fig 6.8a, the strength model of the clamped beam applies to each wing half, Fig 6.8b. This is bent under the influence of the lift forces.

Over the half span the bending moment M(x) iscalculated as

$$M(x) = \frac{1}{2} \cdot \frac{lv \cdot m_F \cdot g}{2} \cdot \frac{b}{2}\left(1 - \frac{x}{\frac{b}{2}}\right)^2 \qquad (6.7)$$

and its course shows graphic Figure 6.8c. It is largest at the clamping point M(x=0):

$$M_{max} = lv \cdot m_F \cdot g \cdot b \cdot \frac{1}{8} \qquad (6.8)$$

The bending strength of the wing is essentially determined by its spar. For its design, it follows from the course of the bending moment that its cross-section at the wing root must be chosen large enough to withstand the moment Mmax.. It can be tapered towards the wing tip.

The curved beam (spar) is subjected to compression on the upper side and tension on the lower side. The neutral line runs through the middle. The highest tensile and compressive stresses are therefore present in the edge fibres. It follows that the spar caps should be placed far outwards and chosen to be flat in cross-section. This allows a lot of material to reach the outside, see Fig 6.9. It is advisable to first select the width B of the (upper) spar cap so that it fits as well as possible into the airfoil contour. Its thickness which results from 0.5*(H - h), is then calculated according to Mmax.

Fig 6.8 The bending moment decreases towards the wing tip
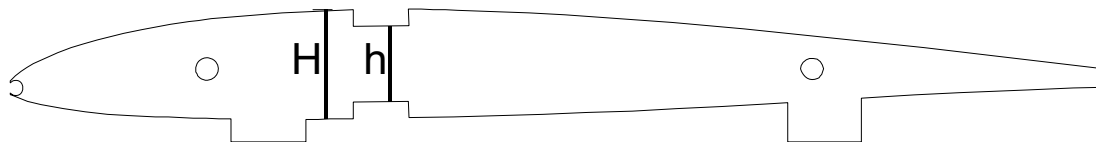
Fig 6.9 Spar arrangement in the wing of the motor glider *Strolch*, airfoil S7012. The calculated value for the thickness of the top boom is d = 0.86mm ≈ 1mm; selected d = 2mm, see example 6.1. The superstructure aids ("protrusions" downwards) will be sanded away later, Fig. 6.11a).

For this purpose, we assume that the bending stress σ_{b_perm} of the material used must not be exceeded by the maximum occurring bending moment M_{max}:

$$\sigma_{b\_perm} \geq \frac{M_{max}}{W_{spar}} \qquad (6.9a)$$

From this we obtain the minimum necessary value for the section modulus W of the intended spar type,

$$W_{spar} \geq \frac{M_{max}}{\sigma_{b\_perm}} \qquad (6.9b)$$

which we now have to dimension according to the specifications in Figure 6.10.

Rechteck (Balken)	Doppel-T	Kasten	Rundrohr	Rundstab
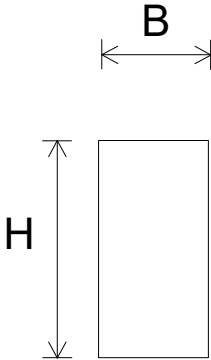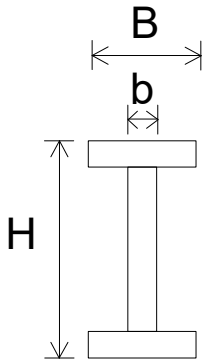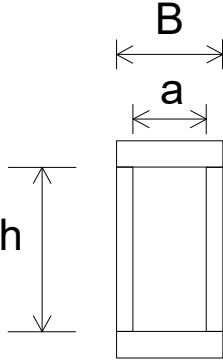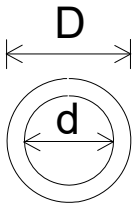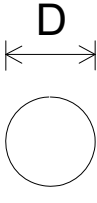
$$\frac{B \cdot H^2}{6} \qquad \frac{B \cdot H^3 - (B-b) \cdot h^3}{6 \cdot H} \qquad \frac{B \cdot H^3 - a \cdot h^3}{6 \cdot H} \qquad \frac{\pi \cdot (D^4 - d^4)}{32 \cdot D} \qquad \frac{\pi \cdot D^3}{32}$$

Fig 6.10 Moment of resistance W_{spar} of spar types

The procedure can be explained with three examples

Example 6.1

The mass of the Motorglider S*trolch* is m = 0.3kg; of this the fuselage mass is m_f = 0.226kg, the wingspan is b = 11.2dm. The steep banked flight is performed with [c_{l_min}=0.1; c_{d_min}=0.02], the interception with c_{l_max}=1. According to Eq. (6.4), lv ≈ 10, with Eq. (6.8) M_{max} ≈ 40 Nm.

Because the spar caps is to be made of pine chords, we select the value σ_{b_perm} = 40N/mm² for the top chord loaded in compression and bending according to Table 6.1. According to Eq. 6.9b, this gives the required section modulus to W_{bar} ≥ 40Ndm/40Nmm^{-2} = 100mm³, which must be applied by the spar construction. The box spar is selected with the characteristic a = B, which results in the necessary required chord spacing

$$h = \sqrt[3]{H^3 - \frac{M_{max}}{\sigma_{b\_perm}} \cdot \frac{6 \cdot H}{B}} \qquad (6.9c)$$

With the further numerical values B = 7mm, H = 14.5mm (airfoil S7012), you get the inner belt distance h = 12mm, which results in a spar cap thickness of 0.5*(H-h) = 1.25mm. Since wooden slats with a thickness of ≈ 1mm are difficult to handle, the dimensions (7x2)mm² are chosen for both belts.

The practical spar construction is now done in such a way that balsa webs are glued between the chords, which - decreasing in thickness - roughly follow the hyperbolic course of the bending stress Fig. 6.8c: starting with 7mm thick balsa for the first panels (therefore a = B!) the thickness decreases to 2mm towards the end of the wing. Jumps in strength are thus avoided and the spar does not become unnecessarily heavy. The balsa webs are milled in such a way that their grain is perpendicular between the chords. In this way they secure the flat chords against buckling and also counteract the shear stress,

see figure 6.8b. If the web grain ran in the direction of the span, there would be a danger of it splitting when the wing bends. The ribbed wing in the shell and in the (almost) finished model are shown in pictures 6.11.
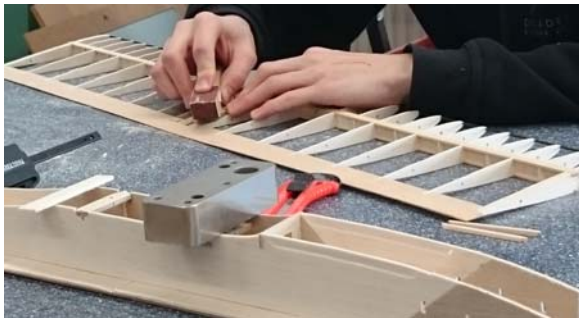
Fig 6.11a) The superstructure aids on the ribs of the wing shell are sanded away. The reinforcement between the spar chords is also clearly visible.. b) Almost finished model motor glider *Strolch*

The consequences of an incorrect spar design can be seen in figure 6.12b. An originally assembled kit model did not survive its first thermal afternoon. The following models in the GTA range were then
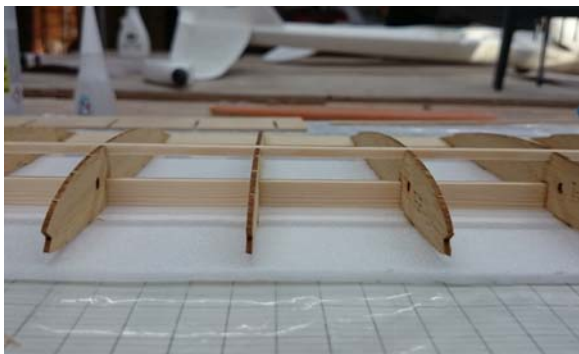
Fig 6.12 A wrongly designed double-T spar made of pine slats in a construction kit model
a) Belt above 3x3, belt below 3x8 standing. The weaker slat would have belonged at the bottom, the stronger belt - installed flat - at the top.
b) The model was controlled out of a thermal in moderately steep path flight. The wing broke during the interception.

constructed with intermediate spar reinforcements: Balsa intermediate webs in the entire middle section and additional planking on both sides in the root area with plywood 0.6mm, Figure 6.13.

The poplar plywood for the fuselage was also replaced by 3mm balsa. The take-off mass of the model was reduced by 200gm to 500gm without any loss of robustness..

For larger models, spar composite materials are often used. In these cases, care must be taken to ensure that their breaking stress is achieved at as equal an elongation as possible. From this point of view, wood and carbon fibres, would be the most suitable, Table 6.1 However, the temperature coefficient of wood is positive, that

Fig 6.13 Continuous webs, double-sided spar planking in the middle area, linearly decreasing: bending stress jumps are minimised in this way.

of carbon fibre negative, so that additional stresses can arise. However, this effect is weakened in the bond with epoxy resin.

Example 6.2

On larger (electric) glider models, wings are usually designed to be plugged together for transport reasons. The centre section is connected to "ears" of roughly comparable span, Figure 6.14. Carbon rods/tubes, which are available in various dimensions, are used as connectors [R&G20]. In this specific case, the carbon shell wing of the RS3 is to be replaced by a lighter ribbed wing with the AG25 airfoil. The data are b = 34dm, fuselage mass mR = 1.26kg, load multiple lv=10. The spar calculation for the wing centre section with the maximum occurring bending moment Mmax ≈ 525 Ndm, Figure 6.8a, and the value given for carbon σ_{b_per} = 500N/mm2 results in CFK chords of dimension 10mm x 1mm.

The seperation should be at x1 = 7.3dm (first red mark at the centre piece end, Figure 6.14). According to Eq(6.7) the bending moment at this point is M(x1) = 172Ndm, see Figure 6.16a. It is to be determined graphically and mathematically which V-angle (dihedral) is possible. In analogy to Eq. (6.9c) we obtain the minimum strength of a carbon bar to be

$$D = \sqrt[3]{\frac{M(x1)}{\sigma_{b\_perm}} \cdot \frac{32}{\pi}}$$ (6.9d)

This results in a diameter D = 7mm, selected D = 8mm, as 7mm is not included in the delivery programme. The graph shows that only a V-angle $\phi \le$ 3deg can be realised, Figure 6.16b.
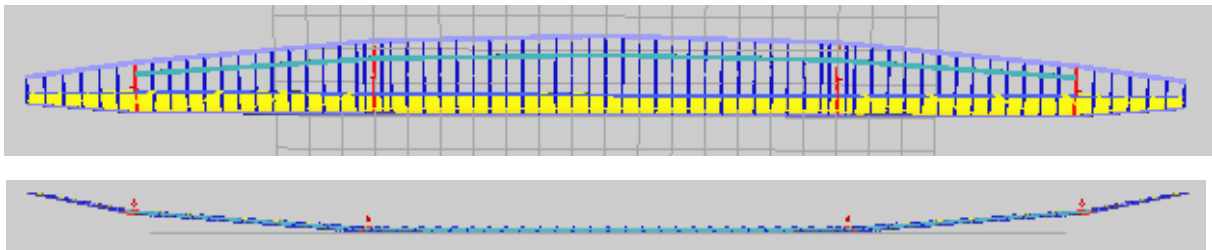
Fig 6.14 Planned ribbed wing for the RS3_electric, assembled from 3 parts

Fig 6.15 Root airfoil AG25 of the wing centre section. The 1.5mm balsa planking extends over the carbon bars. For the spar calculation the heights H =15mm and h = 13mm apply.
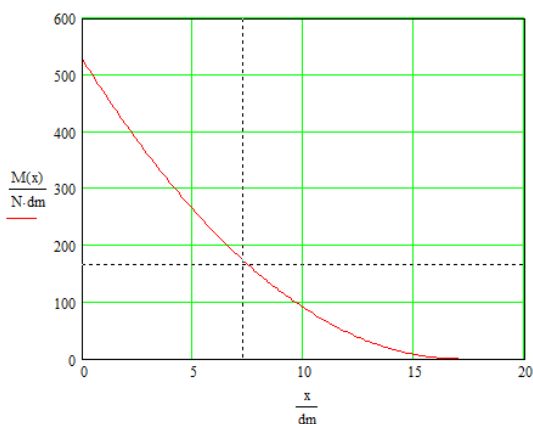
Fig 6.16 a) Bending stress curve in the wing centre section. At the bending point x1 = 7.3dm is the moment M(x1) = 172 Ndm. The round bar must withstand this.
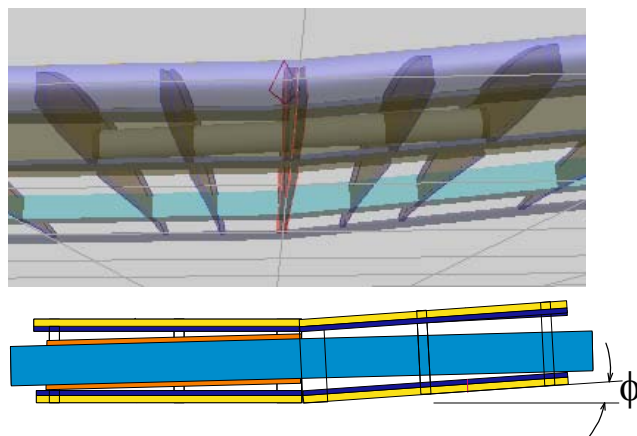
b) carbon rod (blue), D = 8mm, in carbon sleeve (orange) 8/10mm. At the bending point h = 11.7mm. It can be seen that only a dihedral -angle $\phi \le$ 3deg is feasible.

<u>Example 6.3</u>

The pusher low-wing model (pusher_td) was used by many generations of pupils for learning RC-flying in teacher-pupil operation in the hall. It is exposed to two main types of load: the impact on the wall of the hall with subsequent uncontrolled spin and the aerodynamic load of a steep turn to prevent it from hitting the wall. But it must also be possible to intercept the glider after an unexpected engine stop during climb.

For the unavoidable wall stops during training, the construction type "protected motor" has proven itself; the EPP nose absorbs the stop force very well. The landing gear proved to be susceptible to breakage; however, in the event of damage, training operations could always be continued with the help of manual take-offs.

The wing made of 3mm thick Depron cannot withstand the aerodynamic loads without reinforcement. It is to be proven that only two carbon bar caps with a cross-section of 3mm x 0.5mm, (σ_{b_perm} = 500N/mm^2) glued on the upper and lower side at the same distance from the leading edge produce sufficient strength, Figure 6.17.
The data are:
Wing span b = 8.7dm, wing area S_w = 17dm^2; its airfoil is "curved plate", similar to Gö417a. mass m_pusher = 170g, of which the fuselage weighs 114g. If we insert the coefficients for slow and fast flight c_{lmax} = 0.94 and [c_{lmin} = 0.13; c_{dmin} = 0.05], see Eq(6.4), we get

$$lv = \frac{0,94}{\sqrt{0,13^2 + 0,05^2}} \approx 7$$

The bending moment is maximum in the centre of the wing, according to Eq. 6.8 it is calculated as M_{max} = 1.3Nm. With the specified permissible bending stress, the moment of resistance W_{b_perm} = M_{max}/σ_{b_perm} = 2.54mm^3. This moment must be absorbed by the two spar caps. The calculation model is the spar type box, Figure 6.10, with the particularity a = B and the values B = 3mm, H = 4mm, h = 3mm:

$$W_{spar} = \frac{B \cdot (H^3 - h^3)}{6 \cdot H} = \frac{3mm \cdot (4^3 - 3^3)mm^3}{6 \cdot 4mm} = 4,6mm^3$$

also   4,6mm$^3 \geq$ 2,54mm^3
and thus $W_{spar} \geq W_{b\_perm}$ fulfilled
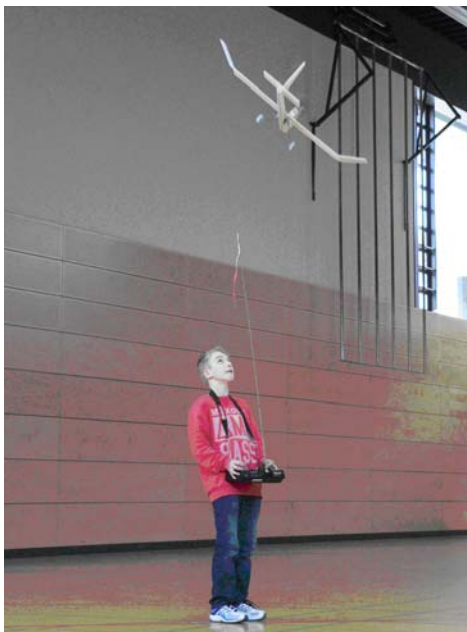
Fig 6.17 The "curved plate" (Gö417a) of Depron, 3mm thick, was used in all beginner's training models the airfoil. Although very simple, the spar "construction" makes the wing overdimensionally stiff.

Development steps Indoor flight training model

The pusher_low-wing model, Figure 6.17, was the result of several development stages, which resulted from the training experiences in the hall. The result was the low-wing pusher_Tandem2, a robust and yet slow-flying model. A classification in the speed range is shown in Figure 6.19.
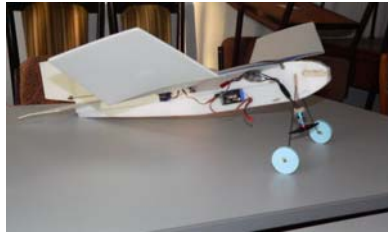
Front-drive high-wing aircraft: slow but sensitive to impact ......

pusher_ high-wing: (*Ogar* bond), more robust against wall impact but no longer slow

pusher_low-wing: robust against impact, not yet slow enough

Low-wing pusher_tandem1: Slow, but poor curve stability

Low-wing pusher_tandem2: slow and good curve stability

Fig 6.18 Development result: slow-flying, on/upstroke robust, good controllability

Fig 6.19 Relationship between minimum achievable air speed and wing load $v_{min}(m/S_f)$, [La16]. Even in the practised depron construction method, it should be possible to achieve v = 2,5m/s: mit S_w = 25dm^2; b_w = 11dm; A_w = 5; m = 88g.

7.0 Design of a model airplane

In the simplest case, a model aircraft is designed "over one's thumb". According to personal taste - and the outsider has no idea how much of this can be put into the appearance of a model - wings, fuselage and tailplane are proportioned to each other and given "sleek" outlines.

The qualified practitioner looks around at competitions or informs himself in model sport magazines. In doing so, he will choose the model that is closest to his aesthetic sensibilities from among the models that have been placed. In both cases, there is a chance that he will produce a model that flies. It is almost not possible to construct a flying model so badly that it does not fly at all.

However, there is also the possibility of designing a model using rules that are laid down in a scheme. These are to be applied to the design of a beginner's motor glider.

7.1 Intended purpose

For a beginner model, performance considerations play a subordinate role. In the foreground are constructional and aeronautical aspects:

*simple construction with consideration of only little existing technological knowledge; robust construction because of presumably hard landings;

*non-critical flight characteristics, i.e. largely self-stable flying, good-natured reaction to control errors.

7.2 Wing geometry (span/ aspect ratio/ area/ angle of attack)

The size of a model aircraft usually refers to its wingspan. The motor glider to be designed here should have a manageable size $b_w \geq 1m$, chosen $b_w = 11dm$. The wing width - i.e. the airfoil length $l\mu$ - now depends on the chosen wing aspect ratio A_w; in the case of the rectangular wing it is $l\mu = b_w/S_w$, see Eq. (5.7) and Fig. 7.1b).

Fig. 7.1a) Design Sketch *Strolch*   b) Moment replacement surfaces of wing and
                                               Tailplane - see example 9.1 in the appendix

This is where the Reynolds number Re comes into play: In contrast to the simplified representation in Figure 5.2 for the profiles NACA 0012 and ClarkY with only one Re number each, the diagrams turn out differently for lower and higher Re numbers in aerodynamic reality, see Figures 7.2a) to c). We can clearly see in diagrams b) and c) that the curves are shift towards higher drag values at lower Re numbers.

Fig. 7.2) Beiwerte-Verläufe des Profils S7012 für Re = 200000; 100000; 50000   [Se89]
| a) $c_l = f(\alpha)$; Proximity line: | b) $c_d = f(\alpha)$ | c) $c_l = f(c_d)$; variable: α

$$ca(\alpha) = (\alpha - \alpha o)\cdot q; \quad \alpha o = -1.75\cdot\deg; \quad q = 0.12\cdot\deg^{-1} \quad |$$

The Reynolds number is directly proportional to the product of airfoil length and speed. For the field of model flight it can be quickly determined with a "fist" formula:

$$R_e \approx v \cdot l_\mu \cdot 70 \tag{7.1}$$

where the airspeed v is entered in m/s and the chord length of the model lμ in mm. First of all, it is important that the Re-number estimated according to Eq(7.1) is not smaller than the smallest Re-number given for a selected airfoil; it can hardly be assumed how much the airfoil drag deteriorates further towards smaller Re-numbers. On the other hand, this means that for a given wing span b_w the aspect ratio A_w must not be arbitrarily large and that v_{min} must be used for the speed calculated according to Eq. 5.3.

For estimation we need the expected model size in the form of the parameters b_w, S_w, A_w, m, whereby Figure 7.3 can be helpful for mass estimation. There, the masses of motor gliders built in *Modellflugclub Rossendorf* are recorded as points $m(S_w)$ depending on the area S_w; a regression line calculated from these points "squints" between them. For the wing area $15\,dm^2 \le S_w \le 20\,dm^2$ envisaged for the planed Model *Strolch*, a mass $0.25\,kg \le m \le 0.5\,kg$ was thus estimated, resulting in a reassuring value $Re_{min} = 56000$ with regard to the selected profile S7012: the polars show $Re_{min} = 50000$.

$$x(A_f) = 0.19\,kg + 0.024\frac{kg}{dm^2}\cdot A_f$$

$\rho = 1{,}23\,kg \qquad S_w = 16{,}1\,dm^2$

$m_{low} = 250\,gm \qquad m_{high} = 500\,gm$

$c_l = 1 \qquad c_d = 0{,}1 \qquad l\mu = 160\,mm$

$$v_{min\_low} = \sqrt{\frac{m_{low}\cdot g}{S_w \cdot \frac{\rho}{2}}\cdot\frac{1}{\sqrt{c_l^2 + c_d^2}}}$$

$$v_{min\_low} \approx 5\,m/sec$$

$$Re_{low} = v_{min\_low}\cdot l\mu \cdot 70 = 56000$$

Fig. 7.3) Mass over wing area of realised Motor gliders in the Rossendorf model flying club

If we wanted to design a performance model, an optimisation calculation would be made at this point with regard to the best wing aspect ratio. Optimisation criteria are the parameters *best glide* and *least sink*, [Br/Frie98]. In the present case of the beginner model, however, we should not reduce the Re-number any further and be satisfied with the aspect ratio $A = b^2/S_w = 7.5$.

Nevertheless, it makes sense to determine the total polar curve of the model and to derive the mentioned parameters from it. To do this, we must formulate the approximate curve $c_{dp}(Re)$ of the airfoil S7012 for each lift coefficient in the range $0 \leq c_l \leq 1.1$ and, using the predefined parameters of aspect ratio and flight mass, iteratively determine that speed which corresponds to the valid Re number within the polar field. The mathematical details of this will not be discussed here. As a result, the black curve (marked with circles) in Figure 7.4 describes the dynamic polar curve of the airfoil determined in this way, i.e. the course of the lift and drag coefficients through the polar field of the airfoil according to Figure 7.2c, and we obtain the model polar, solid red curve in Fig. 7.4), which has now taken into account the total resistance according to Eq(7.2)

$$c_{dtot}(c_a) = c_{dp}(c_l, Re) + c_{di}(c_l, A_w) + c_{dh} \tag{7.2}$$

However, the wing aspect ratio A_w also influences the angle of attack required for a desired lift coefficient: the smaller the aspect ratio, the larger it must be selected in order to achieve the same c_l value as for the wing with infinite aspect ratio according to Figure 7.2:

$$\alpha_A = \alpha + c_l \cdot \frac{57,3\,\text{deg}}{\pi \cdot A} \tag{7.3}$$

These correction values for the angle of attack are visible in Figure 7.4 (pink curve, marked with squares): the angle values for the model polar are larger than those for the infinite aspect ratio.
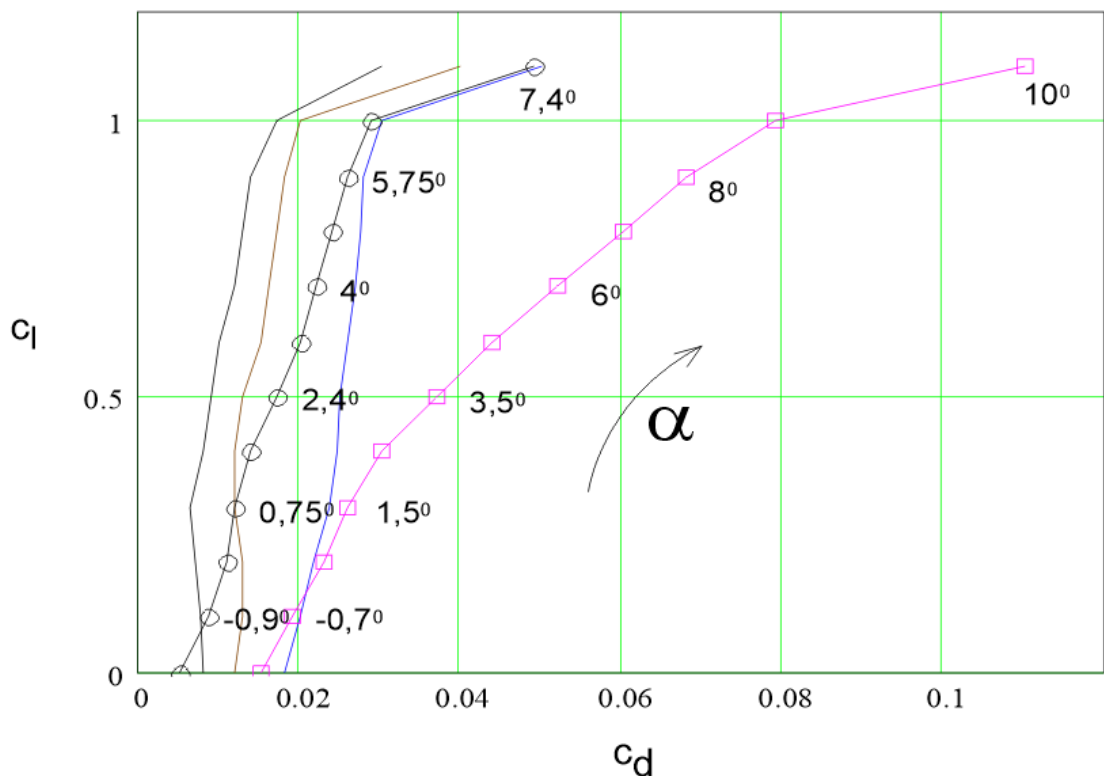

Fig. 7.4: Polar field for the airfoil at Re = 200000; 100000; 50000 (without marking). With the specified model target data, the dynamic profile polar ⊖⊖⊖ and the model polar ⊟⊟⊟; calculated from this. Run variable: Angle of attack α. The larger angle values at the model polar curve take into account the finite aspect ratio A_w = 7.5.

When calculating the model polars, the parameters of best glide and lowest sink are naturally also included: for each c_l and c_d value, the path speed already had to be determined, so it is easy to also output the sink rate v_{sr} and the glide ratio ε or $E = 1/\varepsilon$ in each case. Figure 7.5 shows the velocity polars calculated in this way. If we compare these with the curves shown in Figure 5.8c, d for a larger and heavier model - and without a dependency $c_{dp}(Re)$ having been taken into account there - it can be seen that the values for the lowest sink rate and the best glide are also at different path velocities here.
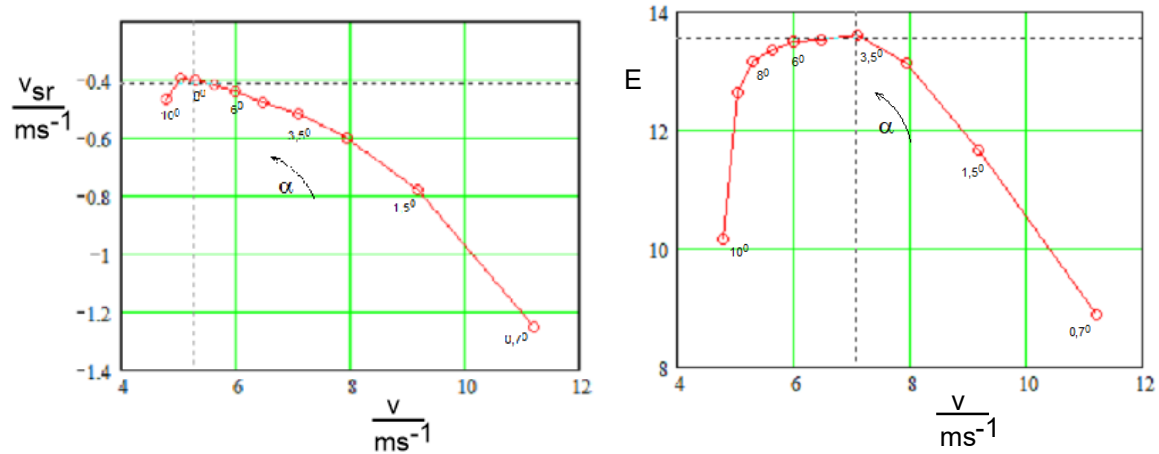

Fig. 7.5a Speed polar $v_{si}(v)$ and   b) course of the best glide $E(v)=1/\varepsilon(v)$ of the *Strolch* model. The *minimum sink rate* v_{sr} is reached at the path velocitie $v = 5.3$m/s (according to $c_l = 0.9$), the *best glide* $E = 1/\varepsilon$ at $v = 7$m/s ($c_a = 0,5$).

This circumstance is interesting for the respective trim settings: when cranking out a thermal bubble, the model should fly as slowly as possible, with the minimum possible sink rate. If, on the other hand, the sky is scanned for thermal bubbles, this should be done as quickly as possible with little loss of altitude, i.e. in the regime of the best glide ratio or slightly faster.

The two trim positions could be found, for example, with the help of a time measurement when flying over a defined distance, whereby the 30m long landing lines used in the mfcR competitions could be used as a basis. The time intervals $\Delta t_{sr} = 5.7s \approx 6s$ and $\Delta t_E = 4.3s \approx 4s$ should be measurable. However, stationary flight conditions must be ensured - for example, an flyover after interception from a higher altitude would provide falsified results.

7.3 <u>Angle of setting EWD</u>
Figure 5.2 has already illustrated the difference between a symmetrical and cambered profile. In addition to the higher maximum lift coefficient, the cambered profile also has the special feature that it already generates lift at an angle of attack $\alpha = 0$deg and only reaches the lift coefficient $c_l = 0$ at a negative angle value, the so-called zero lift angle α_0. Figure 7.6d) shows this relationship on a wing with an infinite span, here $\alpha_0 = -1.75$deg.

a) $\alpha = 3.5$deg ; angle generates $c_l = 0.6$

b) $\alpha = 0$deg ; angle generates $c_l = 0.2$

c) $\alpha = \alpha_0 = -1.75$deg ; angle generates $c_l = 0$ d) Proximity characteristic curve $c_l(\alpha)$ of S7012 f0r Aspect Ratio $A_w = \infty$
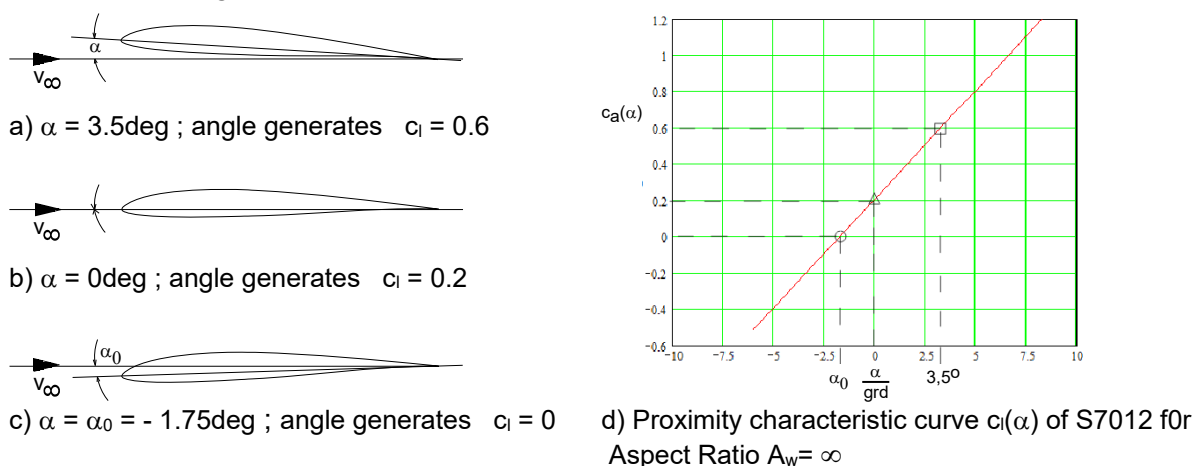
Fig. 7.6 Angle of attack examples for $c_l = f(\alpha)$ of a cambered airfoil

We now consider the combination of wing and tailplane and initially assume that the airflow v_∞, as shown in Figure 7.7a, remains parallel to the longitudinal axis of the fuselage. It is easy to see that the angle difference between the wing and the horizontal stabilizer is equal to the angle of attack of the wing, i.e. EWD = α_w. And because the elevator has a symmetrical airfoil, it will generate neither lift nor down force.

However, the circulation flow shown in Figure 2.6 also acts on the free flow in front of and behind the wing, so that the horizontal tail plane is actually subjected to a downward flow, the so-called downwash. If the horizontal tail plane is not to generate lift or down force, it must be set to the downwash angle $\alpha_{hs} = \chi_0$, Figure 7.7b. In this case, the setting angle difference is EWD = α_w- χ_0. The same effect can be achieved if the EWD is kept the same by setting the angle of attack of the tail plane back to zero, i.e. $\alpha_{hs} = 0\deg$, and reducing the angle of attack of the wing by χ_0, Figure 7.7c. In terms of construction, this has the advantage that the tail plane can be installed parallel to the longitudinal axis of the fuselage, in this case parallel to the underside of the fuselage, Figure 7.8. As a result, the fuselage will be inclined tail-heavy in flight by the angle smaller than χ_0, but this is of no interest here. In performance models, care is taken to ensure that the fuselage flies as aerodynamically favourable as possible; in commercial aircraft, the arrangement is chosen so that the fuselage is horizontal in cruising flight.
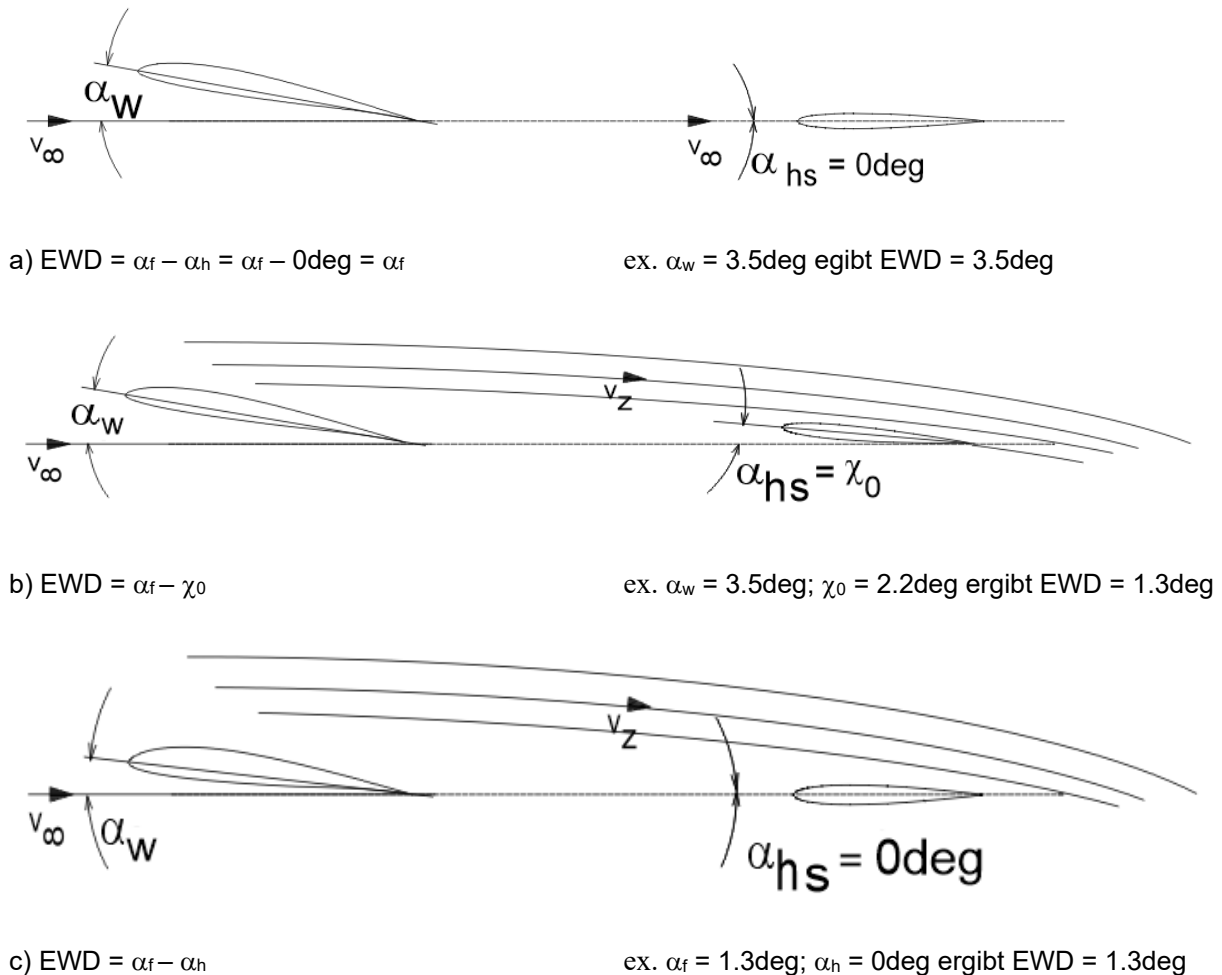

a) EWD = α_f − α_h = α_f − 0deg = α_f ex. α_w = 3.5deg egibt EWD = 3.5deg

b) EWD = α_f − χ_0 ex. α_w = 3.5deg; χ_0 = 2.2deg ergibt EWD = 1.3deg

c) EWD = α_f − α_h ex. α_f = 1.3deg; α_h = 0deg ergibt EWD = 1.3deg

Fig. 7.7 To explain longitudinal difference of angle wing - horizontal stabilizer

The angle χ_0 is calculated as follows [Jä40]:

$$\chi_0 = \alpha_0 \cdot (1-\xi) + \alpha_A \cdot \xi \quad (7.4a) \quad \text{where} \quad \xi = 1 - \frac{0{,}73}{A_w} \cdot \left[1 + \sqrt{1 + \left(\frac{b_w}{2 \cdot rh} \right)} \right] \quad (7.4b)$$

Using the numerical values from Figure 7.1b and the angle values α_0 = -1.75deg the following is obtained
* for the *lowest sink rate*: α_A = 8deg, see Fig 7.5a, χ_0 = 5.6deg und α_w = EWD = 8deg – 5.6deg = 2.4deg.
* for the *best glide*: α_A = 3.5deg, see Fig 7.5b, χ_0 = 2.2deg and α_w = EWD = 3.5deg – 2.2deg = 1.3deg.
The tailplane is installed as intended with a value of α_w = 0deg to the longitudinal axis of the fuselage; however, unlike a performance model, a wing angle of attack for the phase of least sinking, i.e. α_w = EWD = 2.4deg, is provided for the beginner model. The phase of best glide can be found via the trim setting of the tailplane if you have the appropriate flying skills.
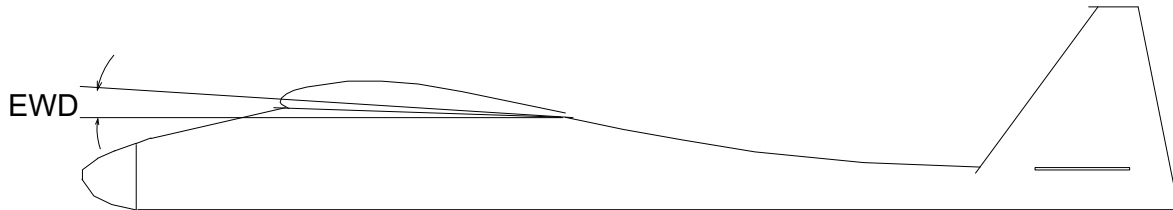

Fig. 7.8 Installed in the *Strolch* model: angle of setting EWD = α_w = 2.4^0; α_{el} = 0^0

7.4 <u>Aerodynamic center and centre of gravity position, longitudinal stability</u>
We now complete the wing-tail plane configuration with the centre of gravity CG, Figure 7.9. A body in space always rotates around its centre of gravity. As shown in Figure 4.1, it is the point through which the three imaginary axes of an aeroplane pass.
Here, however, we are only considering the rotation around the transverse axis, also known as pitching. We can define a neutral point N.P. with the position x_N on both the aerofoil and the horizontal stabilizer: it is located on the aerofoil at $x_{Nw} \approx 0.25 \cdot l_{\mu w}$, and on the horizontal tail plane at due to the symmetrical airfoil at $x_{Nhs} = 0{,}25 \cdot l_{\mu hs}$. It is characterised by the fact that a change in angle of attack $\Delta\alpha$ results only in a change in force ΔF_L at this point; a torque $cm_{0.25}$ also present around this point remains constant.
Let us now consider the effect of an upward gust $\Delta\alpha$ on the combination of wing and horizontal stabiliser. As a result of an additional force ΔF_{Lw}, a clockwise moment around the centre of gravity will occur on the wing, $M_w = \Delta F_{Lw} \cdot (x_S - x_{Nw})$, the model wants to rear up; the additional force ΔF_{Lhs} on the horizontal stabilizer generates the torque $\Delta F_{Lhs} \cdot (rh + x_{Nw} - x_S)$, however, it rotates anti-clockwise, and with a comparatively longer lever arm. Whereas for stationary flight, the two moments acting in opposite directions of rotation are equal:

$$\Delta F_{Lw} \cdot (x_S - x_{Nw}) = \Delta F_{Lel} \cdot (rh + x_{Nw} - x_S) \, ,$$

it is important in the event of a gust that the aircraft deflected about the lateral axis returns to the normal flight attitude as a result of the opposing reaction of the horizontal stabilizer. This ability is called *longitudinal stability*.
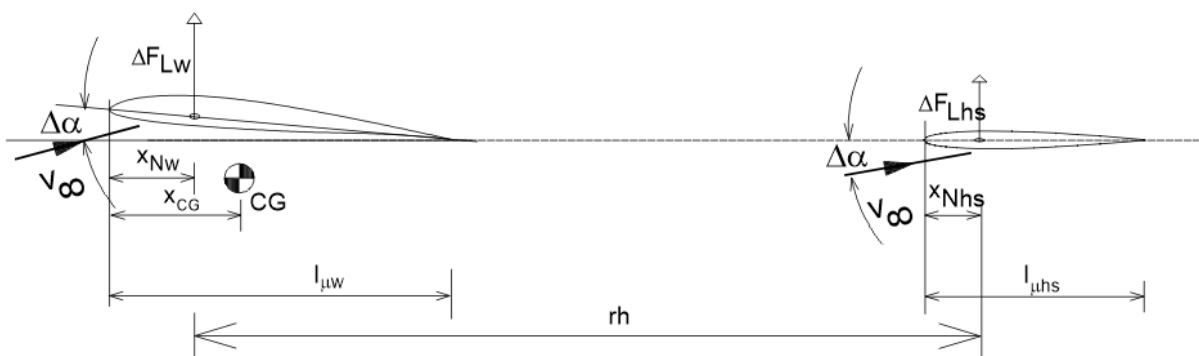

Fig. 7.9 A rearing up of the wing (= right-turning moment) due to an upward gust is counteracted by the horizontal tailplane with its left-turning moment. The settling time is $\Delta t \approx$ 100ms

As a result, the described force changes of the aerofoil and tail plane can be summarised to the effect of a force change ΔF_L at a aerodynamic center of whole model neutral point NP, Figure 7.10.
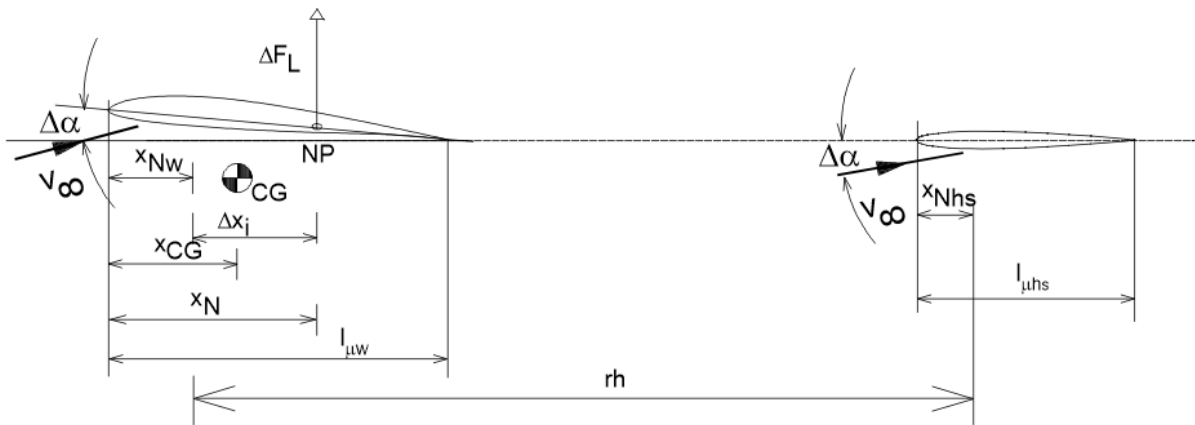

Fig. 7.10 An overall neutral point simplifies the statement on longitudinal stability

The model is longitudinally stable if the centre of gravity SP is in front of the neutral point NP, Figure 7.11a; the additional force ΔF_L applied after deflection at the neutral point returns the model to its normal position.
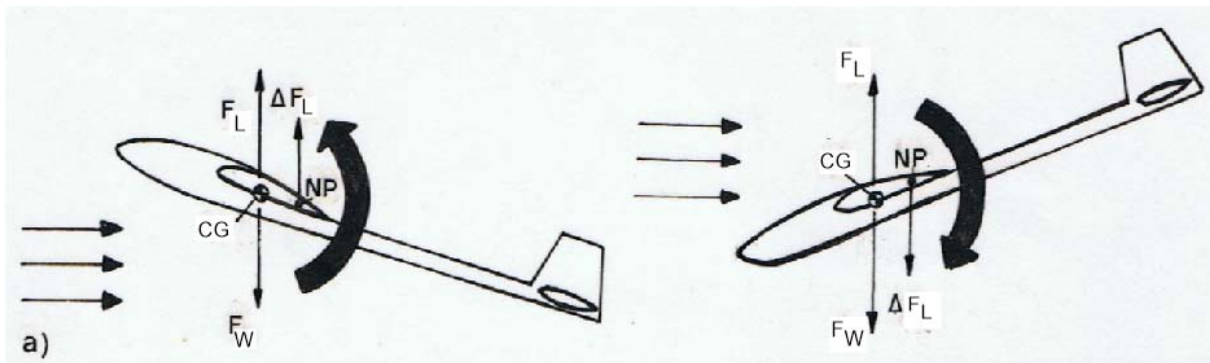

Fig. 7.11a) The center of gravity is in front of the neutral point - the model is longitudinally stable

If the centre of gravity SP is behind the neutral point NP, the additional force ΔF_A will have a destabilising effect after a gust deflection, it will reinforce the rotation that has started, Figure 7.10b
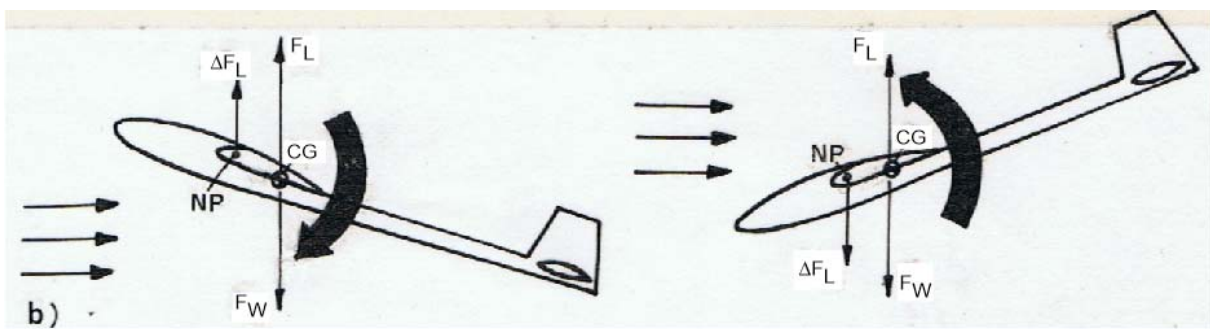

Fig. 7.11b) The centre of gravity is behind the neutral point - the model has no longitudinal stability

To obtain a stability measure as a numerical value, the position of the neutral point x_N must be calculated:

$$x_N = x_{Nw} + \Delta x_i \quad (7.5a), \quad \text{where} \quad \Delta x_i = Beu \cdot V_H \cdot l_{\mu w} \quad (7.5b) \quad \text{and} \quad V_H = \frac{r_h \cdot S_{hs}}{l_{\mu w} \cdot S_w} \quad (7.5c)$$

The quantity V_H is referred to in the literature as the empennage volume, presumably because the numerator results in a three-dimensional value in itself and it also indicates its influence on the centre of gravity position. A long moment arm r_h and a large horizontal stabilizer surface S_{hs} result in a large V_H in Eq(7.5c) and thus a shift of the neutral point towards the tail unit.

According to Musil [Mu78], a range of $0.55 \leq V_H \leq 0.7$ should be observed for thermal and slope flying models; with the values according to Figure 7.1b, $V_H = 0.7$ results. For $A_w = 7.5$ and $A_{hs} = 3.35$, the correction factor Beu = 0.42 can be estimated from the diagram in Figure 7.12. This gives the neutral point position according to Eq(7.5a) for the moment-replacement wing, Figure 7.1b, at $x_N = 0.82$dm.
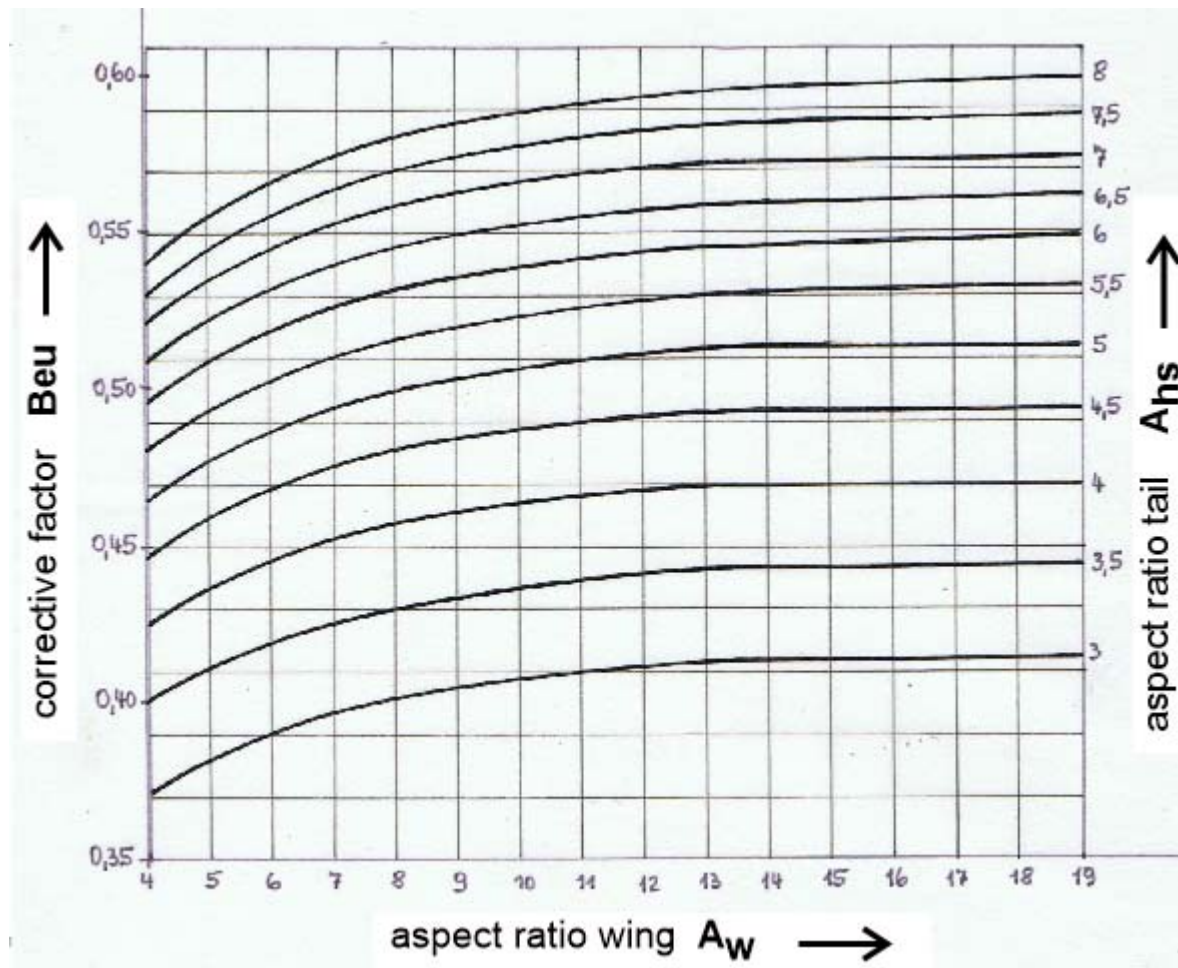

Fig. 7.12 The correction factor B_f [Beu58]

How far in front of the neutral point should the centre of gravity be? Figure 7.11a already shows that a greater distance $x_N - x_{cg}$ between the neutral point N_P and the centre of gravity CG results in greater longitudinal stability, and a smaller distance results in less longitudinal stability.

Derived from this consideration, the stability measure or Stability Margin is defined in relation to the

wing chord length $l_{\mu w}$:
$$SM = \frac{x_N - x_{cg}}{l_{\mu w}}$$
(7.6a)

For commercial aircraft, a stability factor σ of at least 0.05 is required; for gliders, it is in the range of $0.05 \leq SM \leq 0.15$. For RC glider models, $0.1 \leq SM \leq 0.2$ is common for normal flight regimes.

In the speed flight of F3B models, the centre of gravity is often moved back to the neutral point. In this case, it is already a matter of flying in an indifferent balance position, which requires the pilot's utmost concentration and can possibly only be mastered by him because it is only of short duration (≈ 20sec). However, RC models of other classes, e.g. F5x motorised gliders, are also flown at higher speeds in gliding flight in view of possible stronger winds, i.e. with a lower c_l than required for the best glide, i.e. with a lower EWD and therefore with the centre of gravity moved back. However, the lower stability can only be mastered by experienced RC pilots.

The following is selected for the beginner model *Strolch* $\sigma \approx 0.15$. From Eq(7.6a) we get

$$x_S = x_N - SM \cdot l_{\mu w} \qquad (7.6b)$$

and thus $x_S = (82 - 0.15 \cdot 151)mm = 59mm$

Of course, the calculated centre of gravity setting must be checked during a model's entry phase. After a certain "feel-good" speed has been found with manual starts using the trim, it should be brought into a
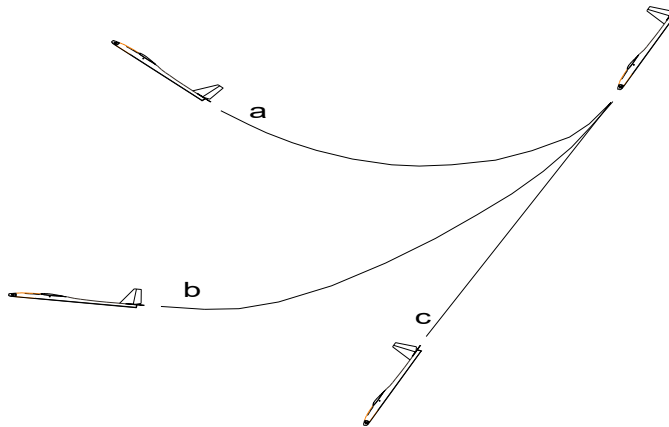

Fig. 7.13 Interception test to assess the SP_position

steep inclined flight path at right angles to the wind from an appropriate height, Fig. 7.13, c. After a few seconds, take your finger off the elevator stick and "leave the model to its own devices". Depending on the position of the centre of gravity, it can take different flight paths a, b or c. If it then climbs steeply upwards, case_a, the centre of gravity is too far forward and the EWD is slightly too high. If it continues to fly at virtually the same steep angle, case_c, the centre of gravity is almost at the neutral point, i.e. too far back, and the EWD is slightly too small; the flight attitude is indifferent. In both cases, the centre of gravity should be altered by changing the trim weights/shifting the battery to such an extent that only a moderate bounce as in case_b occurs. We understand the EWD change here as a slight trim change of the elevator.

However, there is also a recommendation for the size of the vertical stabiliser S_s in the interest of yaw stability, [Lab 8] :

$$V_V = \frac{r_v \cdot S_s}{l_{\mu f} \cdot S_f} \qquad (7.5d)$$

whereby, for the sake of simplicity, it is assumed that the distance between the centre of the vertical stabiliser and the centre of gravity x_{CG} is approximately the same as the stabiliser moment arm $r_s \approx r_h$. Following the literature with the value range $0.02 \leq V_V \leq 0.05$, the size of the vertical stabiliser $S_S = 1.56dm^2$ yields $V_V = 0.04$ and also conforms to the regulations.

7.5 Selecting the drive

Chapter 5.3-3/Motor and propeller explains the basic relationships between motor and propeller and is supplemented with rules for component selection. The following examples show that the drive and model can also be assessed with different initial data.

We will initially remain with the Strolch model, for which a required shaft power P_{sh} = 15W was calculated in example 5.3. With a further estimated motor efficiency η_{mot} = 0.7 (see Figure 5.16), we are looking for a motor with a minimum required electrical power $P_{el} \geq$ 21W. For the Hacker motor A10-13L, the data sheet shows a maximum electrical power P_{elmax} = 75W (15sec); with the specifications I_{max} = 9A (15s) and I_{cont} = 7A, a continuous power P_{el_cont} = 75W*(7/9) ≈ 60W can be estimated. There is therefore no risk of overheating, even without special cooling measures, as the motor is only operated at around one third of the permitted continuous electrical power. In addition, use in a motorised glider always provides sufficient cooling time during the thermal search or sailing time. For the selection of the propeller we also use the measured values, Table 5.1: $P_{sh} \approx$ 20W, revlotion at this operating point n ≈ 5000/min to 6000/min. If we use these values in the graph in Figure 5.33, we find characteristic curves for propellers 8x7 to 9x4, which roughly confirms the 8x4 and 9x5 propellers used for the measurements - and also used for flight operation.

A further limit must be checked: it must be avoided to come close to the speed of sound with the propeller circumferential speed, because otherwise performance-reducing aerodynamic effects occur at the blade tips. According to [MPX21], this should be at a maximum of half the speed of sound, i.e. for the speed

$$n \leq \frac{0{,}5 \cdot 330 \cdot \frac{m}{s}}{\pi \cdot D} \tag{7.7}$$

The maximum measured revolutions on the *Strolch* motor A13-L for the 7x4 propeller is only n = 8579/min, even for a battery voltage of 10.5V, see Table 5.1. 17720/min are permitted according to Eq (7.7); there is also a factor of 2 of safety here.

From the approximation Eq(5.24), the pitch H of the propeller can be checked:

$$H \approx \frac{v_{pr}}{n} \tag{7.8}$$

With the velocity of the air column $v_{pr} \approx$ 10m/s, see Table 5.1 and n = 6086/min, H = 4.5 is obtained. This means that the shortlisted props 8x4 and 9x5 are also correct in terms of pitch; the measurements of the climb rate, Figures 5.37, confirm this.

Fig. 7.14 Motorsegler *EasyStar 3* von *Multiplex*, [HebH10/20] und https://www.multiplex-rc.de/

In another example, we want to find out what climb rate v_{cr} the EasyStar 3 from Multiplex can achieve. The model was presented in FMT_H10/2020. The data of interest are: Mass m = 0.8kg; wingspan b_w = 1.37m, wing area S_w= 28dm2 → Aspect ratio A_w = 6.7. With these data and the assumption [ca; cw] = [1; 0.09] see Figure 7.4, a minimum sink rate according to Eq(5.4) is calculated as v_{sr} = 0.6m/s.

A more detailed analysis, such as the calculation of the sink or rise polars, is not possible,

because the airfoil of the wing used is not known. The Roxxy C28-30-09 motor used, see Table 7.1, is operated with a 3S battery. Here too, the manufacturer does not provide more detailed information, such as resistance R or no-load current Io. Estimates are nevertheless possible:

TYP	Turns / KV	Akku	max. Elek. Leistung 30s	Dauerleistung ca. 65°C	3D**		Scale**		Segler**		Speed**			aVP*
C28-30 • Gehäuse Ø28 x 26,5 • Gewicht 57g • Welle/Ersatz. 31 28 30														
C28-30-09	9 / 1280	2s	**217W** **26A**	160W 19.2A	9x4,5 3s 26A	12,5N	9x4,5 3s 26A	12,5N	8x6 3s 23A	9N	7x7 3s 22A	7,5N	31 4955	32,90*
		3s	**318W** **25A**	234W 18.6A										

Tabelle 7.1 Technical data for the Roxxy C28-30 [MPX21]

As the no-load current Io is not known, we estimate the idle speed to be $n_o \approx U_{ac} \cdot kv =$ 10.5V*1280/Vmin = 13440/min using Eq(5.20). The operating speed should then be $n > 0.65 \cdot n_o$, the usual range is $0.75 \cdot n_o \le n \le 0.85 \cdot n_o$. If we calculate with the upper value of 0.85, we obtain an operating revolution of $n \approx 11420$/min. This makes it possible to estimate the shaft power:

$$P_{sh} \approx \frac{1}{kv} \cdot I \cdot n \tag{7.9}$$

Initially using the continuous current value $I_{cont} = 18.6A$, the result is $P_{wdauer} \approx 160W$. From Eq(5.11), the rate of rise is calculated as follows

$$v_{cr} = \frac{P_{out}}{m \cdot g} - v_{si}$$

where P_{out} is equal to the power output of the propeller: $P_{out} = \eta_{prop} \cdot P_{sh}$. With an assumed propeller efficiency $\eta_{prop} = 0.5$, this results in a climb speed $v_{cr} = 10$m/s, which promises an impressive climb.

Could the model also torque? Using Eq(5.28), the static thrust is calculated as $F_{th\_cont} = 8.7N$, corresponding to holding a mass of m = 0.88kg ... that would be to little. However, if we briefly increase the motor current to $I_{15s} = 25A$, the thrust increases to $F_{th15s} = 12N$, a value that can also be found in the manufacturer's specifications, Table 7.1. The drive would hold a mass m = 1.2kg, with which the EasyStar3 could very probably torque, provided the pilot is able to do so.

To summarise, however, the many assumptions that were made in this case should be pointed out: they can certainly have the effect of tolerances towards the "good side", e.g. that even $v_{cr} = 12$m/s is achieved for the climb, but they can also generate disappointments, which means that torquing is not possible, for example.

Another example concerns a larger CFRP glider, the Stratus 4000, [BauH8/20], presented in FMT_H8/2020. Its data are: $b_w = 4$m; $S_w = 86.2$dm^2; → $A_w = 18.7$; m = 4.88kg; $m/S_w = 56$gm/dm^2. Despite its high wing loading, the sink rate is still $v_{sr} \le 0.5$m/s; however, with $v \ge 10$m/s the model is also travelling quite fast in thermals. Tight beards will be difficult to crank out.

The high-speed flight data described by the test author, which were recorded by GPS logger during interception from a steep inclined flight path, are interesting: v = 60m/s, acceleration in the interception arc a = 10.24m/s^2. With Eq(6.1), Figure 6.1 and $a = v^2/r$, the load multiple

$$lv = 1 + \frac{a}{g}$$

results in $l_v \approx 2$, so this was not a highly loaded strength case. The speed mentioned also allows you to get a feeling for the lift and drag coefficient with which the model flies. Assuming a trajectory inclination flight with the glide ratio $\varepsilon \approx 1:2$, i.e. E = 2, we obtain from the transformation of Eq(5.3)

$$c_l = \frac{m \cdot g \cdot 2}{S_w \cdot \rho} \cdot \frac{1}{v^2 \sqrt{1 + \frac{1}{E^2}}}$$

the values $c_l = 0.023$ and $c_d = c_l/E = 0.012$. A comparison with the polar curve of the beginner's motorglider, Figure 7.4, shows that this operating point lies on the dynamic polar curve of the airfoil in the angle of attack range $-0.9deg \leq \alpha \leq 0.75deg$. From this it could be concluded that the conventional assumption for the "harmful resistance":
$c_{ws} = 0,01 = const.$ is no longer appropriate.
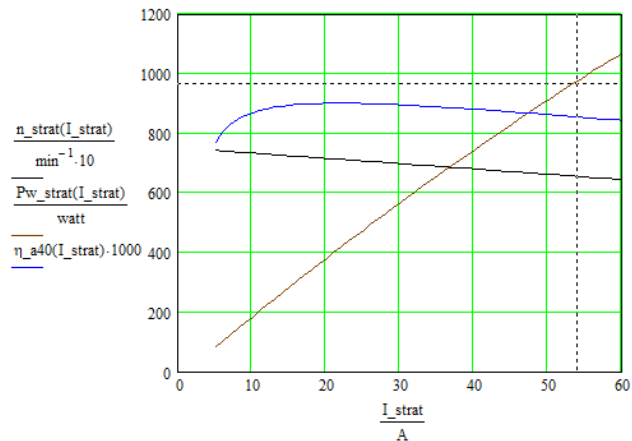Instead, a dependency cws(Re) should also be introduced for this.

Fig. 7.15a) *Stratus 4000 by Valenta* [BauH8/20]   b) Analysing the Hacker A40-14L-V4; U = 21.5V

The model is motorised with a 275g Hacker motor A40-14L-V4-14-Pole kv 355, [Hack21], which is powered by a 6S LiPo-Akku 3800mAh. The detailed manufacturer specifications $P_{el15s} = 1,1kW$; kv = 355/minV; R = 50mΩ; Io=0,85A@8,4V and U = 21,15V allow a performance analysis, Fig. 7.15b. This results in $P_{w15s} = 980W$ at $I_{15s} = 54A$ with $\eta_{mot} = 0.85$, n = 6550/Min.
The values for the propeller size can be surmised from the diagram Fig. 5.33: 16x13, 17x11 und 18x11; the evaluation of Eq(7.7) yields D ≤ 19'' ≈ 18''. The calculation according to the diagram given in [Schu80], Figure 7.17, and the formulae derived from it

$$c_s = v \cdot \sqrt[5]{\frac{\rho}{P_{wh} \cdot n^2}} \; ; \quad \lambda(c_s) = 0,124 \cdot c_s^2 + 0,365 \cdot c_s + 0,033 \cdot \frac{1}{1+c_s} \; ; \quad D(c_s) = \frac{v}{\lambda(c_s) \cdot n} \qquad (7.10)$$

also leads to the result D = 18,4'', if twice the speed of thermal gliding is assumed for the desired speed in powered flight, i.e. v = 2*10m/s=20m/s. The pitch of the propeller then follows the approximation [Brü21]

$$H(c_s) = D(c_s)*(0,253*c_s^2 + 0,0833*c_s + 0,3226) \qquad (7.11)$$

and results in H = 10''. The practically realised propeller has the well-matching size 17x10.

In a final case, a thermal motorised glider is described that can typically be used in the F5J competition class. The task here is to soar for 10 minutes from the lowest possible starting altitude and to complete the flight with a target landing at the end. A logger that flies with the model measures and records the maximum altitude that the model has reached during the engine runtime and up to 10 seconds after the engine stops. This altitude then has a negative effect on the points score: up to an altitude of 200m, half a point is deducted and from 200m, three points are deducted for every metre of altitude. It is therefore desirable to switch off the motor at low altitude and still achieve the flight time of 10 minutes as far as possible. The models are therefore designed for minimum sink rate and airspeed - this is achieved primarily by a low wing loading m/S_w, see equations (5.3) and (5.4). However, the motor and battery can also be selected in such a way that only the maximum sensible height h = 200m is reached within the permitted motor runtime $t_{mot} \leq 30s$, which is equivalent to a climb speed of $v_{cr} \geq 7m/s$.

Technical data of the model *Django*, [BauH2/20], published in FMT_H2/2020: $b_w = 3m$; $S_w = 52,3dm^2$; $\rightarrow A_w = 17$; m = 1kg; $m/S_w = 20.15g/dm^2$. This is a remarkably low wing loading for such a large model, which is also reflected in the low sink rate $v_{sr} \leq 0.3m/s$ and above all in the low airspeed $v \leq 6m/s$. The drive unit is also lightweight: Leopard LC250-30 6pol 5550kv with MicroEdition 5:1NL/T from *Reisenauer* [Reis21]. It has a mass of just 65g and still delivers a shaft power of $P_{sh} = 250W$ at I = 50A, Fig. 7.16b. Applying Eq(5.11), this results in a rate of climb $v_{st} \approx 12m/s$, if the efficiency of the propeller 11x22 is assumed to be only a weak value $\eta_{pr} = 0.5$.

Technical data of the drive unit: kv =1100/V*min, Imax = 50A, P_{elmax}=370W at 2S battery; The manufacturer also provides information for five selected propellers, static thrust in stationary operation see Table 7.2:

_____

Antriebsdaten im Stand:

2s - 7,4V - 9x21,5 GM CFK M35, 6536 rpm, 37 Amp. 271 Watt, VPitch 214 km/h, Eta 75,3%

2s - 7,4V - 11x22 GM CFK M35, 5947 rpm, 49 Amp. 365 Watt, VPitch 199 km/h, Eta 69,7%

2s - 7,4V - 12x8 RF F5J schmal M25, 7069 rpm, 25 Amp. 187 Watt, VPitch 86 km/h, Eta 79,1%

2s - 7,4V - 14x7 GM CFK M25, 6700 rpm, 33 Amp. 245 Watt, Schub 1569g, VPitch 71 km/h, Eta 76,7%

2s - 7,4V - 16x8 GM CFK M25, 6133 rpm, 45 Amp. 336 Watt, Schub 2554g, VPitch 75 km/h, Eta 71,5%

HINWEIS: Schubwerte gerechnet

Tabelle 7.2 Parameters of Leopard *LC250-30* in stationary operation. Thrust values calculated [Reis21]

These values can be used to calculate the missing parameters. Based on the motor equation Eq(5.19), the following can be written for two different measured load values:

$$U = I_1 \cdot R + c \cdot 2 \cdot \pi \cdot n_1$$
$$U = I_2 \cdot R + c \cdot 2 \cdot \pi \cdot n_2$$

The solution to this system of equations is

$$R = \frac{U \cdot (n_2 - n_1)}{I_1 \cdot n_2 - I_2 \cdot n_1} \quad (7.12a) \qquad c = \frac{U \cdot (I_1 - I_2)}{(I_1 \cdot n_2 - I_2 \cdot n_1) \cdot 2 \cdot \pi} \quad (7.12b)$$

For 14x7 and 11x22 this results in the values R = 42mΩ und kv =1/c2π = 1115/min*V. The latter value is very close to the speed constants specified in the data sheet. These values can also be used to calculate the third parameter, idling current Io = 1.94A. This makes it easy to analyse the performance of the motor. Fig. 7.16b)
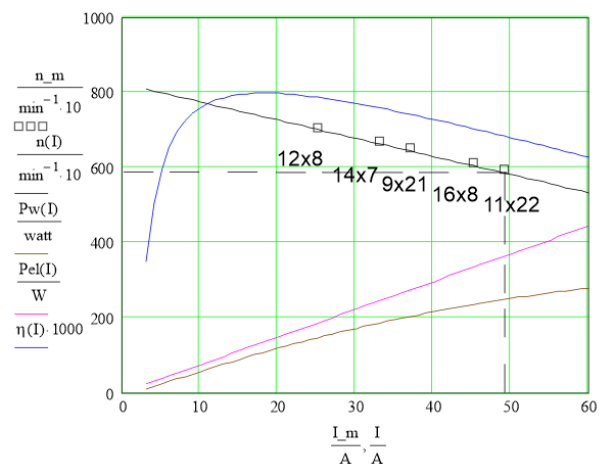

Fig. 7.16a): *Django* von www.sansibear.de

Fig. 7.16b): Analysis of Leopard LC250-30 6pol 5550kv, gear reduction ratio 5:1; U = 7.4V

Applying of Eq(7.10), (7.11) we obtain P_{sh} (49A)= 250W; n(49A)= 5047/min and with a desired velocity v = 10m/s the propeller D = 15,3''x 6,8''. The 14"x7" propeller was used in the FMT article mentioned above.

The following diagram is taken from the literature [Schu80]. It is based on NACA Report No. 350 from 1929.
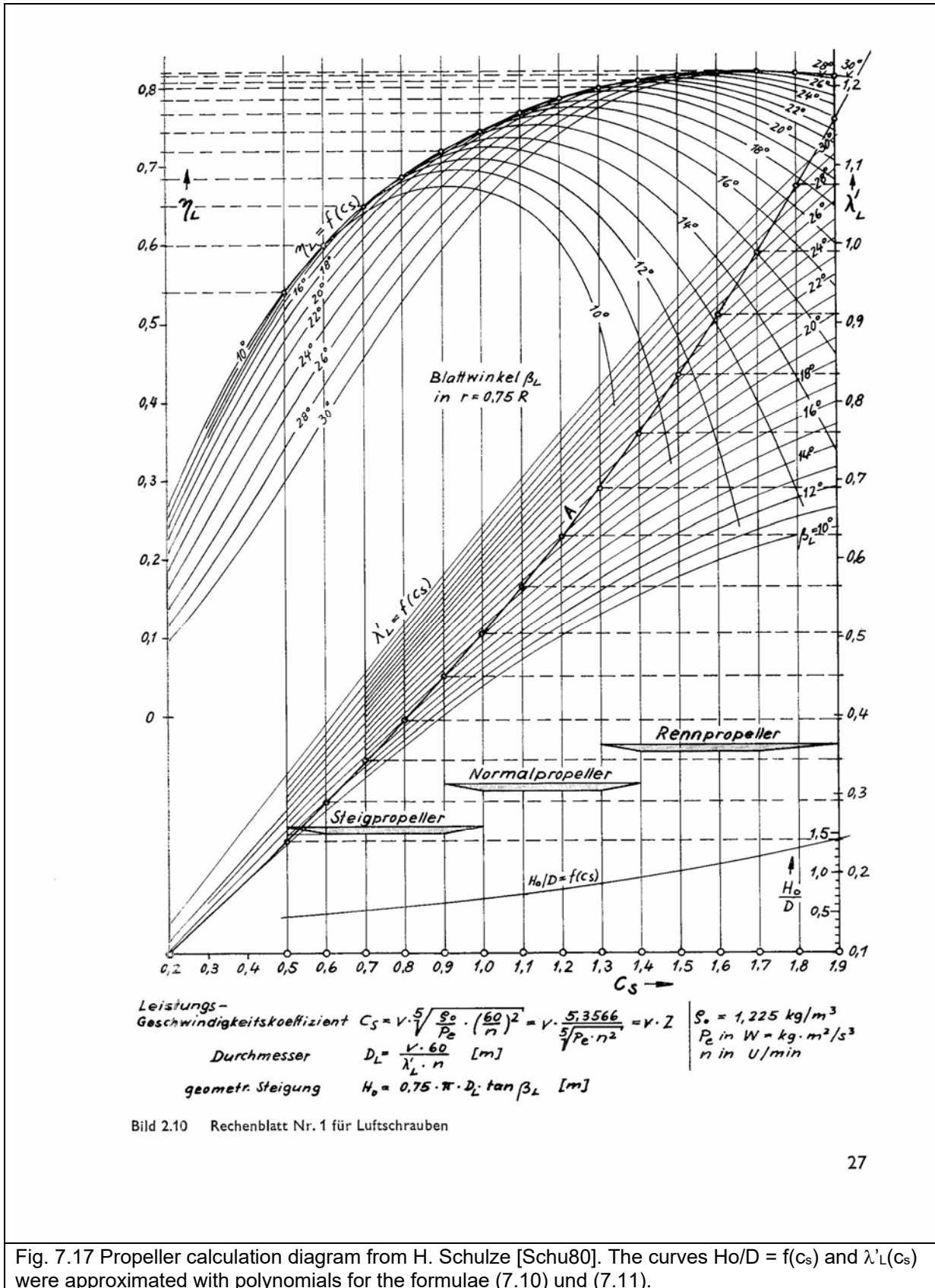

Bild 2.10   Rechenblatt Nr. 1 für Luftschrauben

27

Fig. 7.17 Propeller calculation diagram from H. Schulze [Schu80]. The curves Ho/D = f(c$_s$) and λ'$_L$(c$_s$) were approximated with polynomials for the formulae (7.10) und (7.11).

8.0 Selected themes

8.1 <u>Measurements on the indoor training model low-wing_ pusher</u>

The indoor training model low-wing_ pusher was developed especially for GTA flight training, fig. 6.18. The beginners learnt the basics of remote-controlled model flight. It has proven its worth over several years of student training: it flies well, its manoeuvrability supports last (milli-) second rescues and the robust design copes well with wall impacts or other beginner crashes. Speed measurements were carried out as part of the training programme in December 2013 with student support. The parameters are: m = 170gm, S_w = 16.4dm^2, A = 4,5.

<u>Slow flight</u>: over a distance of 30 metres, students recorded the flight time when flying over waymarks (10m, 15m, ... 30m). The model was flown at its minimum speed, which should be as constant as possible, in order to aim for a *uniform movement*. The slope of the linear interpolation (regression line) results in v_{sl} = 4.2m/s (the abbreviation sl stands for slow).

In horizontal flight, the lift force is equal to the weight force $F_L = F_W$, see Figure 5.10. The effective lift coefficient can be calculated from Eq(5.10) as follows
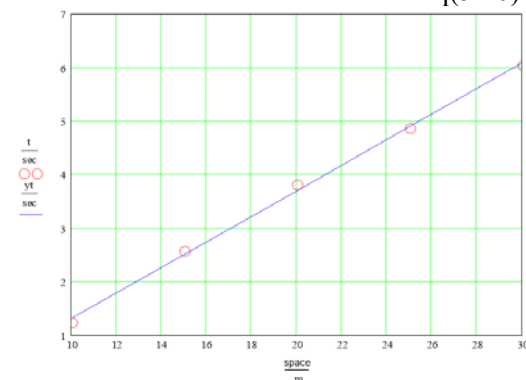

Fig 8.1: Time-distance diagram at minimum possible speed

$$c_{l\_sl} = \frac{2 \cdot m \cdot g}{\left(v_{\_sl}\right)^2 \cdot S_w \cdot \rho} \tag{8.1}$$

The result is c_{l_sl} = 0,94

If conclusions are to be drawn about the drive, the resistance value F_d must be known because $F_{th} = F_d$. To do this, we first determine the resistance coefficient, see Eq(7.2)

$$c_{dtot} = c_{dp} + c_{di} + c_{wh}$$

According to the measuring polars, fig 8.3, a c_{dp} = 0.035 applies to the airfoil Gö417a (Re =42000) at c_l = 0.94. With A_w = 4,5 we obtain for the induced resistance coefficient according to Gl(5.8)

$$c_{di} = \frac{c_l^{\;2}}{\pi \cdot \Lambda} = (0,94)^2 / 3,14*4,6 = 0,065$$

Using the harmful drag coefficient c_{dh} = 0,01, we obtain the coefficient value of the total drag in slow flight

$$c_{dtot\_sl} = 0,035 + 0,063 + 0,01 = 0,11$$

and for the drag force according to Gl(5.2)

$$F_D = \frac{\rho}{2} \cdot v^2 \cdot S \cdot c_{dtot\_sl} = (0,5*1,23\text{kgm}^{-3})*[(4,2\text{ms}^{-1})^2*0,164\text{m}^2*0,076)] = 0,195\text{N}$$

According to Figure 5.10, in steady level flight $F_S = F_W$ and therefore F_S = 0,195N. This propulsive *force* F_{th_sl} = 0,195N must be generated by the drive. The propulsive *power* results in
$P_{sl} = v_{sl}* F_{th\_sl}$ = 4,2ms^{-1}*0,195N = 0,82W.

With the coefficients $c_{d\_sl} \approx$ 0,11; c_{a_sl} = 0,94 we obtain the operating point 1 in the polar diagram fig 8.3

<u>Acceleration phase</u>: as a uniformly accelerated movement is to be expected here, a distance of 30 metres was now subdivided more finely and the roll path up to take-off with subsequent low-level flight was tracked over time. The measured values from at least 5 repetitions were analysed, Figure 8-2a. In this case, the interpolation through the measurement points (*curve fitting*) was used to find the acceleration value that showed the best path over time according to the relationship

$$s = \frac{a}{2} \cdot t^2$$

It resulted in $a = 2.3 \text{m/s}^2$. The velocity (represented by the straight line) reaches the value $v_{fa} = 11.5 \text{m/s}$ after the time $t = 5.5 \text{s}$ (the abbreviation fa stands for fast). Figure 8.2b now shows a calculation[8] of the velocity and displacement curve, taking into account the increasing resistance of the model. The velocity no longer increases in the further course but reaches a stationary value; it remains at $v = 11.5 \text{ m/s}$: the equilibrium between thrust and drag force assumed in Fig. 5.10 has been reached. On the other hand, this shows the limits of an approximation; it is always important to make an estimate for its range of validity ... in this case it is only correct for the first few seconds. The calculation of the transient process is more complicated.
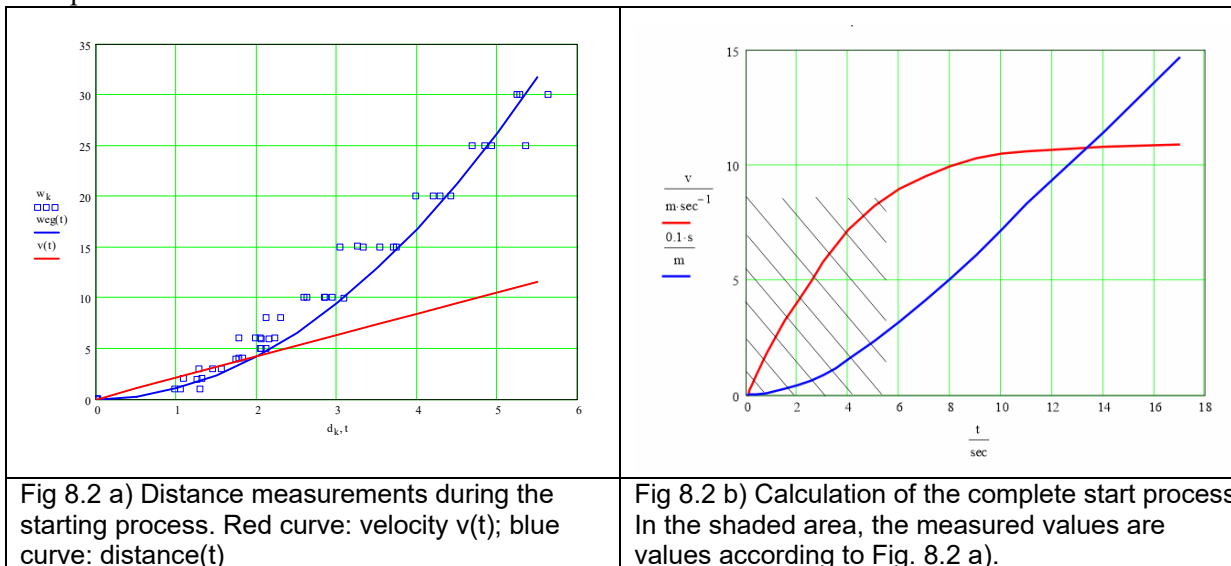

Fig 8.2 a) Distance measurements during the starting process. Red curve: velocity v(t); blue curve: distance(t)	Fig 8.2 b) Calculation of the complete start process In the shaded area, the measured values are values according to Fig. 8.2 a).

With the found acceleration value $a = 2.3 \text{m/s}^2$, the thrust force emitted by the propeller results in $F_{th\_fa} = \text{mass} \cdot a = 170 \text{g} \cdot 2.3 \text{m/s}^2 = 0.39 \text{N}$. The propulsive power is $P_{fa} = v_{fa} \cdot F_{th\_fa} = 11.5 \text{ms}^{-1} \cdot 0.39 \text{N} = 4.5 \text{W}$. In relation to cruising flight, the demand for thrust is therefore higher by a factor of 2 and for power by a factor of 5. This may remind us of our last medium- or long-haul flight: after climbing at full power, the aircraft becomes pleasantly quieter when it reaches cruising altitude.

Here, too, we want to determine a polar point: Again from Eq(8.1) we calculate c_l this time with the velocity value $v_{fa} = 11,5 \text{m/s}$. This results in the lift coefficient $c_{l\_fa} \approx 0.13$, the corresponding polar point is $c_{dp\_fa} = 0.04$. Te total value is $c_{dfa} = c_{dp\_fa} + c_{dh} = 0.05$, see operating point 2 in the polar diagram Figure 8.2 This point is also plausible, so our rather coarse measurement method provides satisfactorily accurate values.

What we can learn from this

Although students prefer to practise aerobatics or "aerial combat", they are prepared to take measurements if there is a chance that they will get a turn as a pilot. In this case, the challenge is to bring the model from the unusually high speed into a "calm path" after take-off and the initially flat (= slightly depressed) flight. With regard to the evaluation, there can be an aha experience when the acceleration value $a \approx 2 \text{m/s}^2$ is estimated "free eye" ... where else in practice is there the possibility of metrological contact with this physical quantity?

It is also interesting to compare the thrust F_{th_fa} emitted by the propeller during taxiing and flying with the value measured in static thrust: $F_{th\_fa}/F_{th\_st} = 0.39 \text{N}/0.8 \text{N} \approx 0.5$. We will encounter this ratio again in experiment 8.2/take-off trolley.

---

[8] The time curves are solution curves of a differential equation that describes the starting process, see also section 8.8
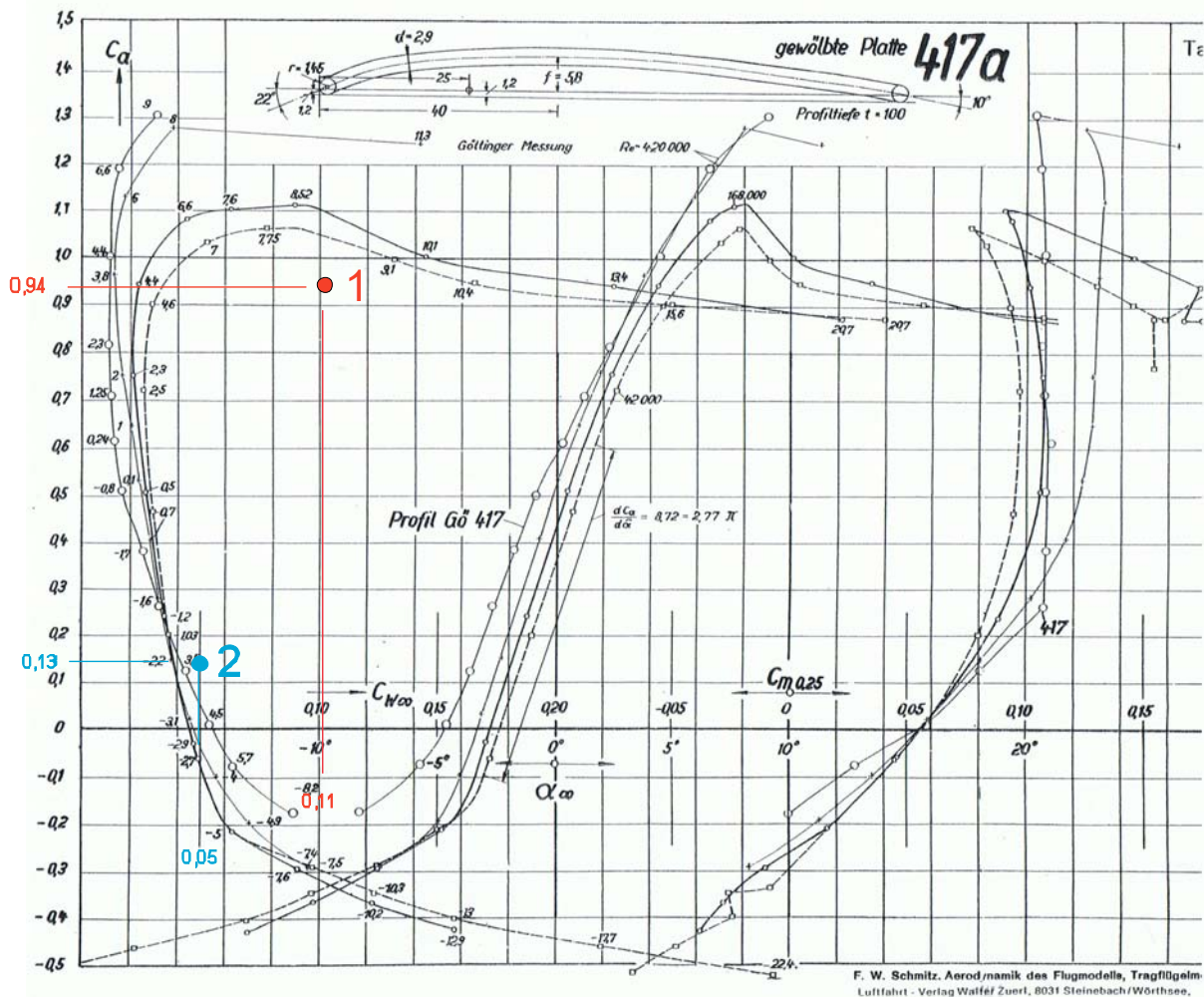
Fig 8.3: Wind tunnel results for the *Cambered plate* Gö417a, Re = 42000 bis 420000 by [Sz42].
The points entered 1 [c_{a_sl} = 0,94; c_{w_sl} = 0,11] und 2 [c_{a_fa} = 0,13; c_{w_fa} = 0,05]
result from measured values, which were determined with the participation of the pupils of the
Gymnasium Dresden- Bühlau in *slow and fast flight* of the <u>low-wing_ pusher</u> model.

8.2 <u>Motor glider Luxx on take-off trolley</u>

A student from the 8th grade chose the subject of flying for his physics project. As a practical contribution, he planned to add a landing gear to his motorised glider. However, he was persuaded to build a take-off trolley instead of the undercarriage [La18].
What should the trolley look like? For use on a grass runway a robust body and sufficiently large wheels were required. Ball bearings were to be used to minimise friction. And the angle at which the longitudinal axis of the body should lie in the trolley had to be clarified.

Fig 8.4: Motor glider Luxx on take-off trolley

How large must be the sum of the angles $\gamma + \alpha$ so that the model get airborne at a desired speed v?
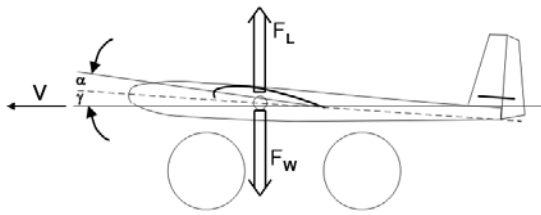
It lifts off when

$$F_L \geq F_W \text{ , where } F_W = mass \cdot g$$

From the lift formula Eq(5.1) one calculates the lift coefficient

$$c_l \geq \frac{2 \cdot F_L}{\rho \cdot v^2 \cdot S_w}$$

...and from the curve c_l vs. angle of attack α the required angle sum, Figure 8.5 is calculated. Using the data of the model Luxx: mass=0.47kg $F_L = 0.47kg * 9.81m/sec^2 = 4.58N$, $S = 0.21m^2$,

the angle sum of angels are given:
e.g. velocity 6m/sec, 8m/sec,10m/sec:

$$v = (6 \quad 8 \quad 10)m/sec;$$
$$\rightarrow c_l = 1.0 \quad 0.55 \quad 0.36$$
$$\rightarrow \gamma + \alpha = (8.2 \quad 3.6 \quad 1.4)deg$$
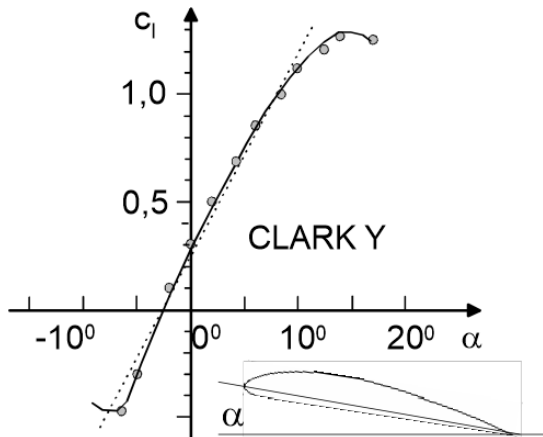
Fig 8.5: Take-off trolley and approximated airfoil

The practical implementation revealed summe $\gamma + \alpha = 7^0$. There is a question: is an accelleration to v = 6 …8 m/sec possible in a gym for testing? And would there still be enough space for a landing manoeuvre?

With $\quad \Delta t = \dfrac{\Delta v}{a} \quad$ in $\quad \Delta s = \dfrac{a}{2} \cdot \Delta t^2 \quad$ it yields $\quad s = \dfrac{v^2}{2 \cdot a}$

The numerical example: Desired speed v = 7m/s and assumed acceleration a = 2m/s² leads to $\Delta s = 12.3m$ ... a value that gives hope.

The positive test with video proof:

-c.g. in front-   -c.g. in back-   -c.g. middle-
Fig 8.6: Test with video proof: 3 take-offs and 3 videos with position-variation of center of gravity

The video observation shows: the model lifts off at the same point always! Just as it gets airborne and started to fly, longitudinal stability is affected by responsible parameters (e.g. angle difference wing to horizontal stabilizer and position of c.g.).

But: how fast was the model at the moment of take-off? The analysis of the video shows the parameters of interest: lift-off time t_{lo} = 2,8sec and lift-off distance s_{lo} = 9m. By solving the equations for the uniformly accelerated motion

$$v_{lo} = a \cdot t_{lo} \qquad\qquad s_{lo} = \frac{1}{2} \cdot a \cdot t_{lo}^2 \qquad\qquad (8.2)$$

we obtain $\quad v_{lo} = \dfrac{2 \cdot s_{lo}}{t_{lo}} = 6,43 \dfrac{m}{\sec} \quad$ and thus also $c_l = 0,86$ and $\gamma + \alpha = 7^0$

The result is plausible, it confirms the initially estimated speed range of 6...8m/s. However, in view of the approximate airfoil data and a simple measurement method, the calculated angle $\gamma + \alpha$ = 7deg matches the installed angle $\gamma + \alpha$ = 7deg suspiciously well!

Incidentally, it is not clear in this context whether the induced angle of attack, i.e. the effect of aspect ratio- in this case A_w = 8,57 – must be taken into account in this dynamic start-up process. If so, a measurement result of $\gamma + \alpha \approx$ 9deg would have been expected..

In addition, the effect of measurement tolerances must also be considered: if a tolerance of only 5% is assumed for time and distance measurement, $F_s = F_t = \pm 5\%$, speed is distorted by $\pm 10\%$ due to $F_v = F_s + F_t$, resulting in the angles 5,5deg and 9,5deg. For tolerance calculation, see section 8.5 / Tolerance considerations

Additional parameters can be calculated beyond the scope of the student's work:
*acceleration value a = 2,29m/s^2;
*Thrust force F_T = (mass_lx + mass_trolley)*a = (500gm+300gm)*2,3m/s^2 = 1,76N;
* Power delivered by the propeller P_{pr} = v_{lo}*F_{th} = 6,43m/s*1,76N = 11,3W;
*electrical power P_{el} = 7V*5A=35W and thus the total efficiency $\eta_{ges} = P_{pr}/P_{el}$ = 0,32;
* the estimated distribution of efficiencies η_{contr} = 0,92; η_{mot} = 0,9; η_{pr} = 0,4;
* with measured static thrust F_{T_st} = 3,3N the relation F_T/F_{T_st} = 1,76N/3,3N = 0,53.

What we can learn from it

With simple measurements during take-off phase students can determine the physical variables *velocity* and *accelleration* at the take-off point. This corresponds to 9th grade school physics.
The lift-off itself illustrates the term lifting force F_L

The model engine increased the trolley-speed linear up to the point where FA > FG and the modell takes off. Using the measured values take-off-time and take-off-distance students can calculate the angle of attack $\alpha+\gamma$ during take off. They learn how to use the diagram Lift Coefficient vs. Angle of Attack.

Besides a link to theory, a trolley is additional fun during RC control training.

8.3 Take off with tricycle undercarriage

The following model was intended for transition training from beginner training - Figures 6.17 and 6.18 - to indoor aerobatics. It was intended to introduce the students to aileron control. Nevertheless, it had to be impact-resistant, which is why the pusher configuration was also chosen here.

USA Lockheed P38 Lightning, first flight 1939. The aircraft was mainly used for long-range reconnaissance during the war.

Antoine de Saint-Exupéry, author of The *Little Prince*, did not return from a reconnaissance flight in such an aircraft in 1944.
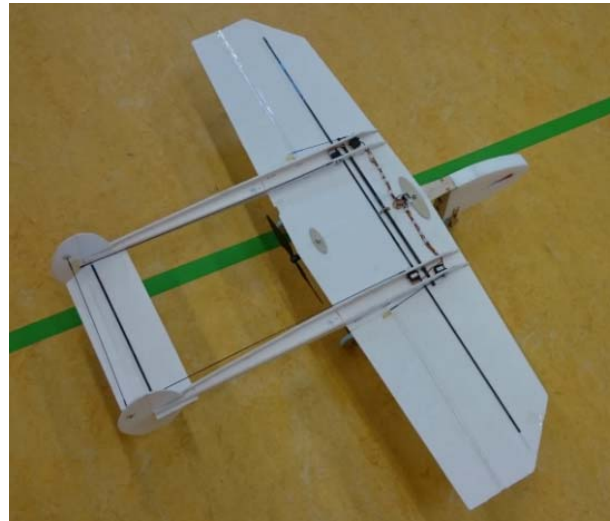
Model: b_w = 1m; S_w = 22dm^2; A_w = 4,6; m = 200g
tail plane S_{hs} = 1dm^2; A_{hs} = 2,7

Fig 8.7   P38 aeroplane and training model with protected drive for aerobatic preparation

Like the aeroplane, the model also is designed with a tripod undercarriage, which gave rise to the question: What angle of attack α had to be installed in the model so that it would rotate around the main undercarriage by "pulling the elevator" and take off at v = 10m/s? Like the previous models, the wings and tail units were to be made of 3 mm thick Depron panels, but now the "flat panel" was to be used for the airfoil. The results of wind tunnel measurements are shown in Figure 8.9, [Sz42].

With the lever ratios shown in Figure 8.8, the model rotates over the main landing gear if

is fulfilled
$$F_{hs} > m \cdot g \cdot \frac{x_1}{x_2} \qquad (8.3)$$
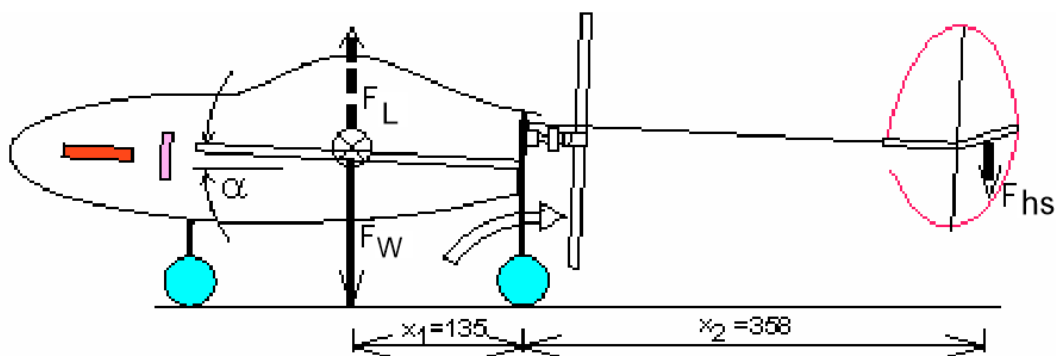
$$F_{hs} > 0,8N \qquad .$$

Fig 8.8 The take-off procedure consists of taxiing, rotating (increasing the angle of attack) and lift-off

If the horizontal tailplane were designed as a pendulum horizontal stabilizer, according to Eq(5.1) this value would be reached at a speed v ≥ 16 m/s, assuming a c_{l_hs} = 0.5. From Figure 8.9 we obtain a (negative) angle of attack $\beta \approx$ 5deg for that.
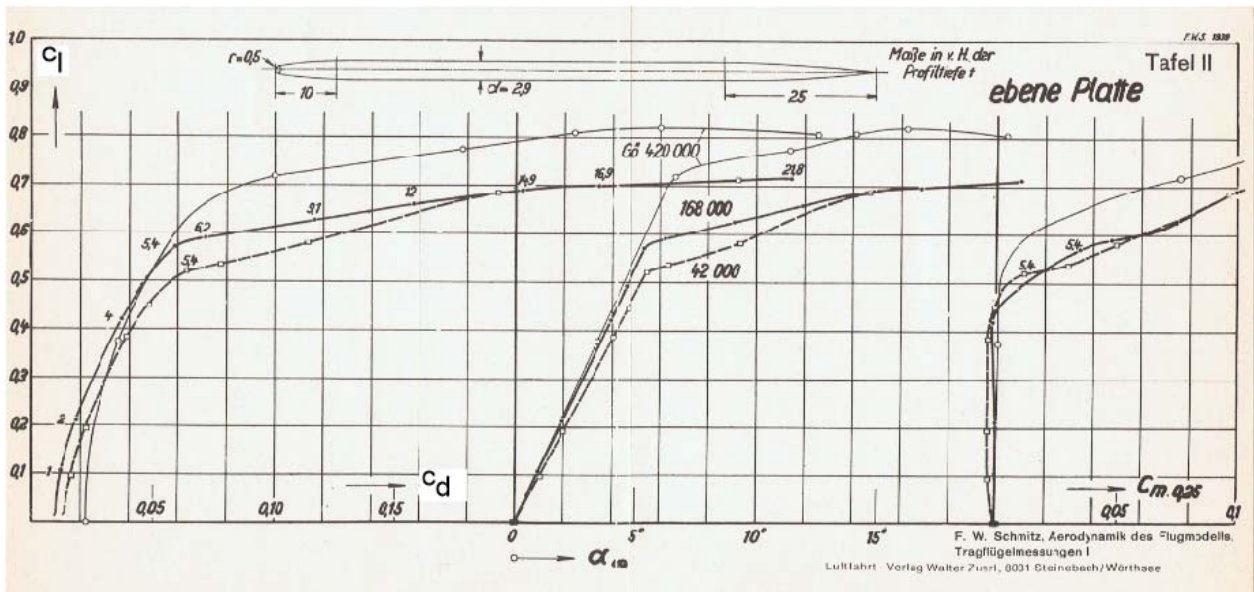
Fig 8.9 Wind tunnel results of the plane plate according to [Sz42]

For practical reasons, however, the tail plane was built with a flap. Musil provides a conversion diagram for this [Mu78], Figure 8.10; this applies in the linear range of lift behaviour. In this case, the ratio

$$\frac{l_{\mu\_f}}{l_\mu} = \frac{39mm}{105mm} = 0{,}37$$

becomes the ordinate value $\frac{\partial \beta}{\partial \eta} \approx 0{,}7$ and we obtain the required flap deflection $\partial\eta = \frac{5\deg}{0{,}7} = 7\deg$ instead of the pendulum elevator with the angular deflection $\beta \approx 5^0$.

However, if take-off is to take place at v = 10m/s, it is necessary to compensate the weight force F_W with the aid of the counteracting wing lift force F_L by means of the preset wing angle α to such an extent that the elevator deflection causes the model to rotate during taxiing.
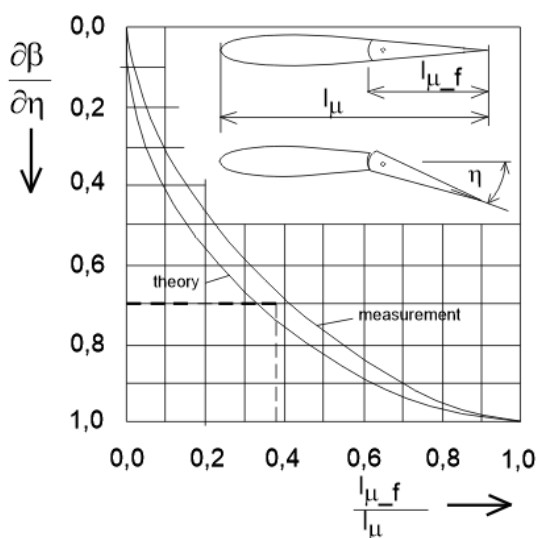

Fig 8.10 Effect of the flap length l_{μ_f}/l_μ on the required flap angle [Mu78]

As with the horizontal tailplane, only a maximum lift coefficient of $c_{lw} = 0.5$ can be generated at the wing. However, with $S_w = 22dm^2$, the surface area available for generating lift is around 20 times greater..

Even at v = 5m/s, $F_L \approx 1.7N$ is generated, even though the angle of attack required for $c_l = 0.5$ due to the only moderate aspect ratio $A_w = 4.6$ according to Eq(7.3) requires an induced angle of attack of $\alpha_{Aw} = 7deg$.

With the realised angle of $\alpha = 5deg$ in Figure 8.8, a satisfactory take-off procedure was achieved: after a few metres of taxiing, "pulling" the elevator led to rotation. The angle value was very easy to achieve with a slight extension of the nose wheel strut.

<u>What we can learn from it</u>
A nose wheel landing gear extends the range of examples in the modelling area: in addition to the lift calculations for a wing, lever laws must now also be applied.

An elevator is a small aerofoil with a flap. A diagram is used to show how the parameters *elevator flap* and *deflection angle* can be approximately converted to the angle of attack of an undivided wing with the same lift force.

8.4 <u>Calculation of speed polars in a Java programme</u>

In this case, a model flight-based work entitled "Important aerodynamic and physical variables on an aerofoil" was produced for the subject Information Technology (IT). In the practical part, the student from a year 10 class used the Java-based development environment Processing to display lift and drag curves and the sink rate of a glider in the programme he created, Figure 8.11
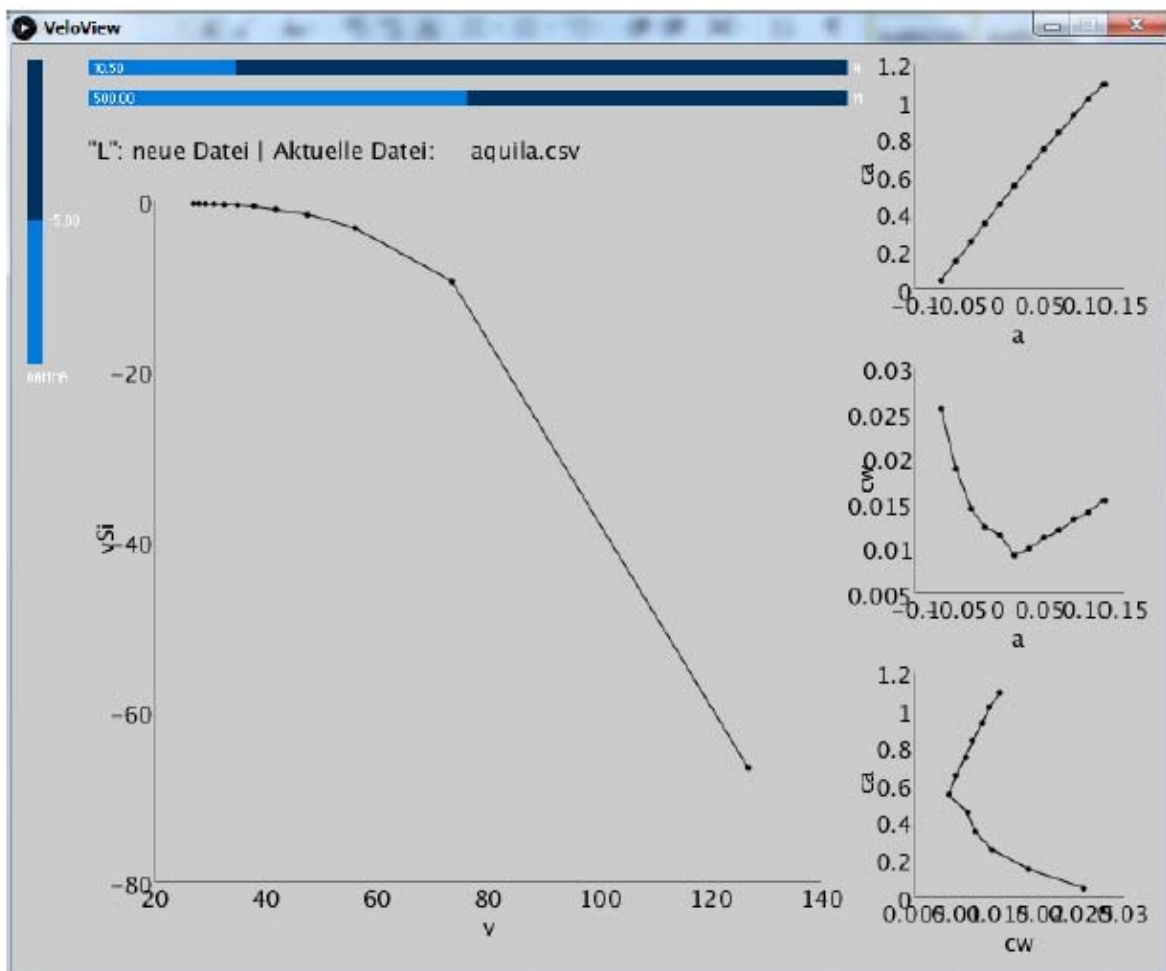

Fig 8.11 Result output with the help of the VeloView programme created

The basic principles presented in the introductory section are taken from the literature, and some examples are also taken from the first version of this booklet accompanying the GT lessons.

<u>What we can learn from it</u>
In this case, the application of GTA topics to school work relates to the IT subject. As done here, visualisation programs can initially be programmed to display characteristic curves; up to four parameters can be entered for this purpose. Further calculations are not yet possible, but it is a starting.

8.5 Measurement results and tolerances

There is a mocking proverb that says: "He who measures measures dung" - and the old master locksmith's saying: "Centimetres are a watchmaker's measure". Although the measurements in the above sections are intended to provide a basic understanding and make no claim to high accuracy, the following at least points out the sources of tolerances and their propagation.
Here is a simple example from electrical engineering: The measured voltage value across a resistor R may be subject to a tolerance ΔU, which may be caused by the tolerance of both the resistance ΔR and the current ΔI: $U \pm \Delta U = (I \pm \Delta I) \cdot (R \pm \Delta R)$. The value ΔU is determined by partial differentiation according to the individual components, whereby the other components are considered constant:

$$U = I \cdot R$$

$$\Delta U = \left| \frac{\partial U}{\partial I} \right| \cdot \Delta I + \left| \frac{\partial U}{\partial R} \right| \cdot \Delta R \tag{8.4}$$

$$\Delta U = R \cdot \Delta I + I \cdot \Delta R$$

It is useful to generate the relative sizes of the deviations from this

$$\frac{\Delta U}{U} = \frac{R \cdot \Delta I + I \cdot \Delta R}{I \cdot R}$$

$$\frac{\Delta U}{U} = \frac{\Delta I}{I} + \frac{\Delta R}{R} \tag{8.5}$$

so that the relative tolerance TO in abbreviated form is

$$TO_U = TO_I + TO_R$$

So if, in an electronic circuit, the voltage drop across this resistance may only have a maximum tolerance of $TO_U \leq 5\%$ for functional reasons, then this resistor may only have a tolerance of $TO_R = \pm 2\%$ if the current may also have an uncertainty of approximately $TO_I = \pm 2\%$. The calculation procedure for the tolerance analysis of the speed measurement of the take-off trolley, see section 8.2, is similarly simple.

Another example concerns the measurements of orbital and descent velocity, from which the coefficients c_l, c_d can be determined. The measurement technology for this is available today, it records these values and we have to insert them into the corresponding equations resolved according to c_l and c_d:

$$v = \sqrt{\frac{mass \cdot g}{S_w \cdot \frac{\rho}{2}} \cdot \frac{1}{\sqrt{c_l^2 + c_d^2}}} \tag{5.3} \qquad v_{si} = \sqrt{\frac{mass \cdot g}{S_w \cdot \frac{\rho}{2}} \cdot \frac{c_d^2}{\sqrt{(c_l^2 + c_d^2)^3}}} \tag{5.4}$$

each resolved according to $c_l(v, v_{sr})$ and $c_d(v, v_{sr})$ [La94]

$$c_l = \frac{mass \cdot g}{S_w} \cdot \frac{2}{\rho} \cdot \frac{1}{v^2} \cdot \sqrt{1 - \left[\frac{v_{sr}}{v} \right]^2} \tag{8.6a} \qquad c_d = \frac{mass \cdot g}{S_w} \cdot \frac{2}{\rho} \cdot \frac{v_{sr}}{v^3} \tag{8.6b}$$

How are the tolerances of the measured values of v and v_{sr} included in the accuracy of the coefficients? The calculation is somewhat more complex here. The result for the dependence of the lift coefficient and for the dependence of the drag coefficient is

$$\frac{\Delta c_l}{c_l} = \frac{\Delta \rho}{\rho} + 2 \cdot \frac{\Delta v}{v} + \frac{1}{\left(\dfrac{v}{v_{sr}}\right)^2 - 1} \cdot \frac{\Delta v_{sr}}{v_{sr}} \quad (8.7a) \qquad \frac{\Delta c_w}{c_w} = \frac{\Delta \rho}{\rho} + 3 \cdot \frac{\Delta v}{v} + \frac{\Delta v_{sr}}{v_{sr}} \quad (8.7b)$$

or in short form

$$TO_{c_l} = TO_\rho + 2 \cdot TO_v + \frac{TO_{v_{sr}}}{E^2 - 1} \quad (8.8a) \qquad TO_{c_d} = TO_\rho + 3 \cdot TO_v + TO_{v_{sr}} \quad (8.8b)$$
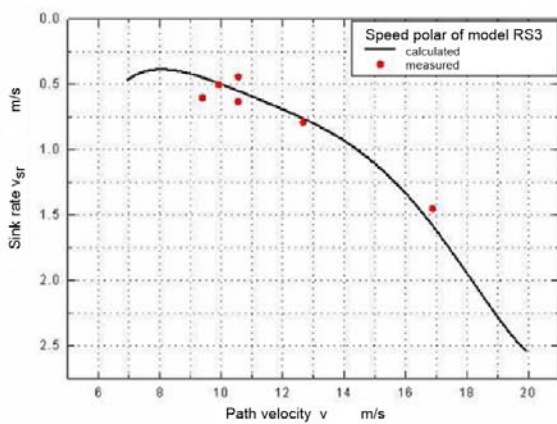

Fig 8.12 Speed polar of the RS3 F3J model [JW04], see also Fig 6.7a

We can see from this that the coefficients are particularly sensitive to the tolerance of the speed values: their measurement errors are included with factor of 2 for c_l and a factor of 3 for c_d. With regard to the factor for the sink rate in Eq(8.7a) or (8.8a), it should be noted that a range $E < 8$ is rarely of interest for polar measurements; thus the third term in Eq(8.8a) usually falls by the wayside, see as an example the velocity polar of the RS3 in Figure 8.12. Even steeper trajectory inclination flights, as carried out for force measurements on deflected wing flaps, see Figure 8.14b, remained at $E \geq 2.4$.

8.6 Servobelastung

Figure 5.3 already pointed out the advantage of variable airfoil geometries using flaps, especially in connection with the F3J-model RS3. In these cases, all wing sections are usually cambered at the same angle using the remote control setting. In addition, very large angles are also of interest, for example, if the model is to be brought down from a greater height without a significant amount of lift; the flaps then have the function of a brake and are not necessarily extended over the entire wing. It is easy to imagine that in these cases a greater force must be absorbed by the servo than with smaller angles.
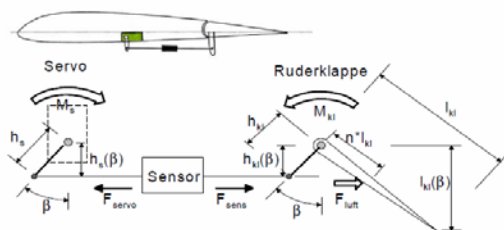

Fig 8.13 Force sensor between servo and wing-flap [Sc13].

The modelling industry offers servos in a wide torque range. But what values are involved in practice? In a Jugend-forscht project, theoretical estimates and measurements were made [Sc13].

Figure 8.13 shows the arrangement of the (tension-) force sensor between servo and a wing flap. The servo torque that must resist the torque

of the rudder flap can be specified for the sketched rudder position::

$$M_{servo} = F_{sens} \cdot h_s = F_{Luft} \cdot \frac{h_s \cdot n \cdot l_{kl}}{h_{kl} \cdot \cos(\beta)} \qquad (8.9)$$

With the measured value of the path inclination flight shown in Figure 8.14b F_{sens} = 3N and due to hs = 1cm, M_{servo} = 3Ncm results. Assuming the main load is applied at n = 0.5, the air flow presses on the flap with $F_{air} \approx$ 10N; the velocity is v = 14.7m/s,
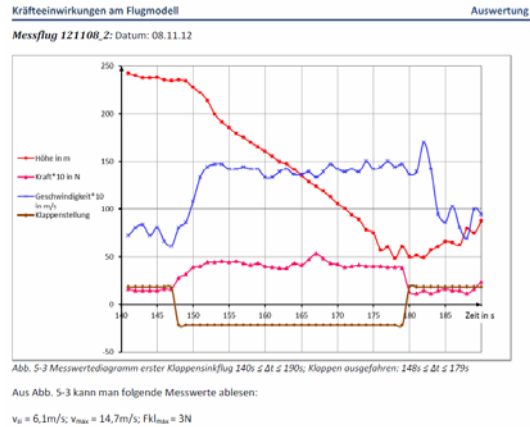

Fig 8.14a Test model Arcus Sport/robbe and b) Measurement plot: a trajectory inclination flight [Sc13]

The model is made of moulded foam (EPP). Its data are b = 2.56m, S_w = 51dm², m = 2.3kg

Lower two curves: status signal "flap" and sensor signal F_{sens}; upper two curves: quasi-linear height reduction h(t) and rectangular signal as response of the speed sensor v(t); v= dh/dt

As a result of the inclination flights and confirmation measurements in the Dresden-Klotzsche wind tunnel, a flap drag coefficient $c_{d\_fl} \approx$ 1.25 was defined. This means that the air force acting on the flap can be calculated approximately:

$$F_{air}(\beta) = 0{,}5 \cdot \rho \cdot c_{d\_fl} \cdot S_{fl} \cdot v^2 \cdot \sin(\beta) \qquad (8.10)$$

Diagram Figure 8.15 shows force curves for the ArcusSport flap calculated using this formula. These corresponds well with the measured values.
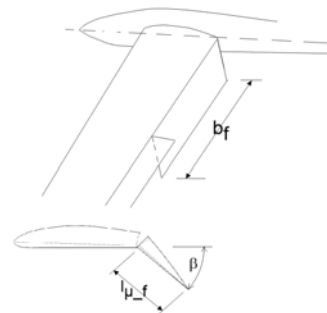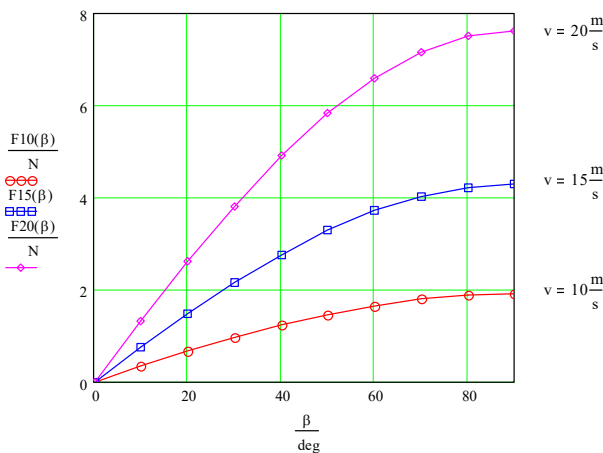
$$S_f = b_f \cdot l_{\mu f} = (4.5 \cdot 0.55) \cdot dm^2 = 2{,}5 dm^2$$

meas_exampl: v = 14,7m/s, v_{si} = 6,1m/s;
(E = 2,4),
β = 42⁰ → Force at servo F_s = 3N

Fig 8.15 Force $F_{air}(\beta)$ acting on the arcus flap, calculated with Gl(8.10)

Another example shows qualitatively the effect of centrifugal force on a flap, Figure 8.16. The model flies at a quasi-stationary speed v until the time t_1 = 3-49.014Min, then the elevator is pressed to initiate the

loop. The speed v decreases, the centrifugal force F_{c_el} (=Fz_{HR}) acting on the elevator increases until the loop is released at t_2 = 3-50.014.
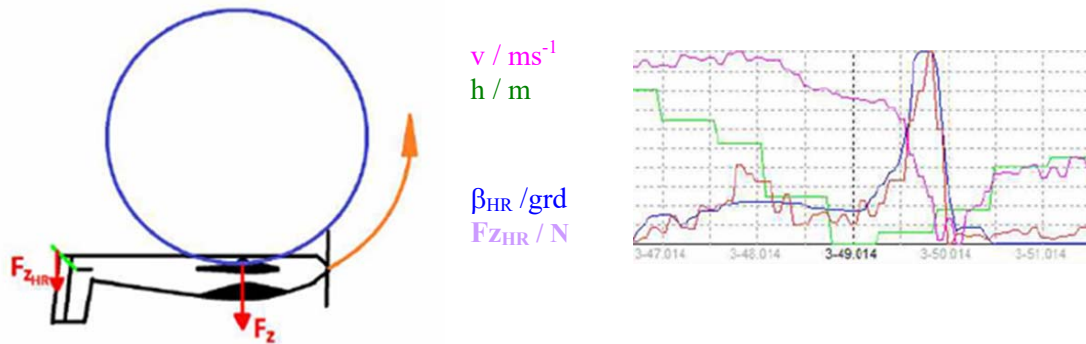

Fig 8.16 Inverted loop of an MPX Parkmaster 3D and measuring plot with centrifugal force Fz_{HS}

For larger aerobatic models, such as the Mx2, the effect of 3D figures on the servo load is now of interest. For this purpose, it is important to determine the position of the centre of gravity of the

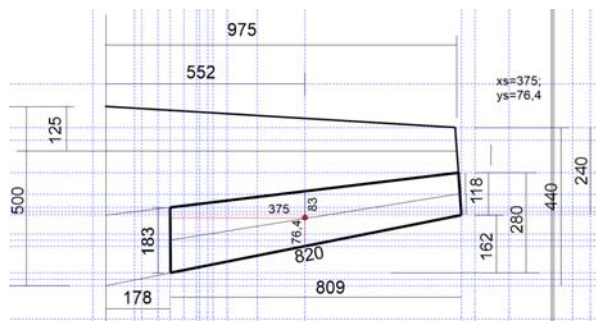Fig 8.17a The Mx2 is designed for 3D aerobatics

Fig 8.17b Coordinates of the cg of aileron
x_S = 375mm; y_S = 76,4mm; M_S = m_{QR}*83mm

control surfaces, see the aileron in Fig. 8.17b. If this centre of gravity is known, the hinge moment M_S = m_{ail}*83mm = 1.16kgcm can be specified using the mass of the aileron, e.g. m_{ail} = 140g. If the model is standing on the ground or flying horizontally, the gravitational acceleration g = 9.81m/s^2 leads to the static rudder moment M_{ail_st} = 11.4Ncm. If manoeuvres are flown, the resulting rudder moments can be estimated and it can be checked whether the use of servos recommended by the model manufacturer is justified.

Center of gravity position:
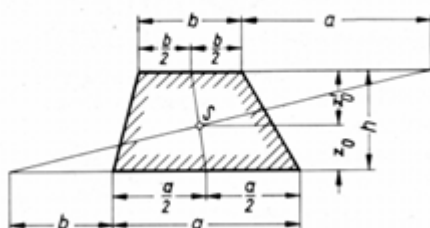
$$z_0 = \frac{h}{3} * \frac{a+2b}{a+b}$$

$$z'_0 = \frac{h}{3} * \frac{2a+b}{a+b}$$

The center of gravity lies on the line connecting of the centers of the parallel sides

Fig 8.18 Graphical determination of the centre of gravity [Gerh]

Load cases for flaps are
*airflow pressure during flap deflection or in the spin motion
*forces that arise during acceleration processes

To estimate the forces, the flap masses must be known and the centres of gravity surfaces must be calculated:
aileron:
$S_{ail} = 12.18dm^2$, Radius $R_{ail} = 83mm$, mass $m_{ail} = 140gm$
elevator, half area:
$S_{el} = 7.6dm^2$, Radius $R_{el} = 95mm$, mass $m_{el} = 55gm$
rudder:
$S_{rud} = 7.4dm^2$, Radius $R_{rud} = 91mm$, mass $m_{rud} = 50gm$

The following table shows the torques of the aileron and the half elevator occurring under different load conditions.
As it turns out, the cases of interception from a steep flight path and spin dominate. However, it is possible that spin rotations of 2/sec are already maximum values, so that even these only result in half load compared to interception.

The rudder is not calculated as its parameter values are close to those of the elevator.
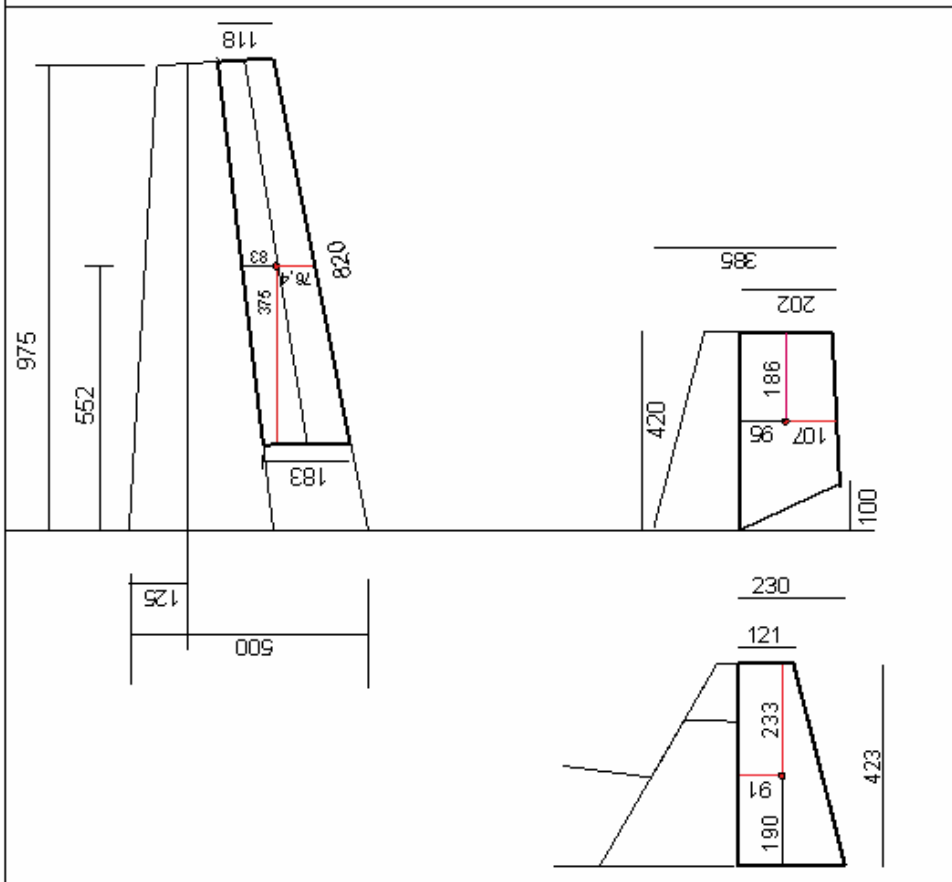
Fig 8.19 Control surfaces of the Mx2 model and position of the individual centres of gravity

contr. surfaces →	aileron	elevator
Flight manoeuvres ↓		
Model at rest or horizontal flight	R_{ail} = 83mm, m_{ail} = 140gm The acceleration due to gravity g = 9.81m/s² generates a static flap moment with the distance R_{ail} = 83mm of M_{ail_st} = 11Ncm	R_{el} = 95mm, m_{el} = 55gm The acceleration due to gravity g = 9.81m/s² generates a static flap moment with the distance Rhr = 93mm M_{el_st} = 5Ncm
Landing strokes acceleration	assumptions: sink rate v_{sr} = 1m/s; braking time 0.1s → flap moment M_{ail_br} = 23Ncm	assumptions: sink rate v_{sr} = 1m/s; braking time 0.1s → flap moment M_{el_br} = 10Ncm
Looping acceleration	assumptions: v = 10m/s, radius of loop r = 1m → flap moment M_{ail_lo} = 116Ncm	assumptions: v = 10m/s, radius of loop r = 1m → flap moment M_{el_lo} = 45Ncm
flap deflection air flow pressure	assumptions: v = 10m/s, flap angle β = 45° → flap moment M_{ail_air} = 50Ncm	assumptions: v = 10m/s, flap angle β = 45° → flap moment M_{el_ang} = 34Ncm
Spin acceleration air flow pressure total acceleration air flow pressure total	assumed spin rotations: n_{sp} = 2/sec → flap moment M_{ail_sp2acc} = 100Ncm → flap moment M_{ail_sp2air} = 36Ncm → $M_{ail\_sp2acc} + M_{ail\_sp2air}$ = 136Ncm n_{sp} = 5/sec → flap moment M_{ail_sp5acc} = 633Ncm → flap moment M_{ail_sp5air} = 225Ncm → $M_{ail\_sp5acc} + M_{ail\_sp5air}$ = 858Ncm	For the calculation, an assumption is missing for the radius with which the elevator circles downwards around an imaginary line during the spin
Interception acceleration	assumed: airfoil NACA 0012; c_{lmax} = 0.8; c_d = 0.04; mass = 3kg; v = 50m/s; Radius r = 10m: → load multible lv = 20 → flap moment M_{ail_int} = 230Ncm	load multible lv = 20 → flap moment M_{el_int} = 102Ncm

Tab. 8.1 Flight manoeuvres of a 3D aerobatic model and expected flap moments

8.7 Solar drive - how many cells are required?

In contrast to man-carrying aircraft, such as the Solarimpuls_2 [SI], in the model, the wing alone is considered as a surface for solar cells. For the sake of simplicity, a rectangular wing is assumed; design (strength) reasons mean that only a wing area reduced by a factor of k is available as a surface for the solar cells (red outline). Two typical values are assumed:
*k1 = 0,67: the solar cells cover from the main spar to the trailing edge;
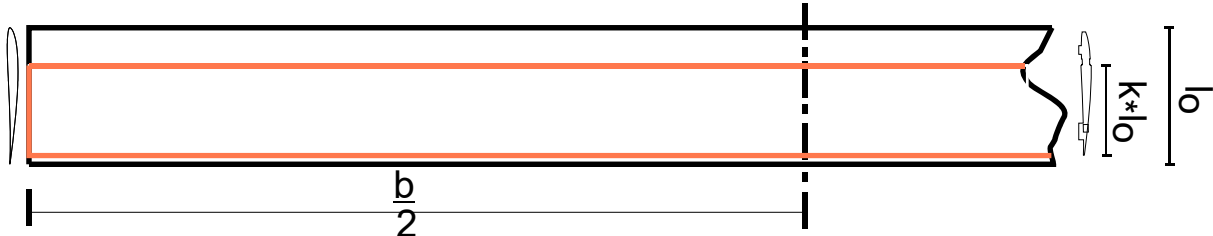*k2 = 0,88: the solar cells cover from the leading edge to the trailing edge.

Fig 8.20 Half-span of a rectangular wing

The question of the number of cells means: How large must the span be so that the model can climb safely? To do this, we need to know how much heavier the model will be when the solar cells are installed. Figure 7.3 shows the statistically determined relationship between the model mass m and the wing area S_w of motorised gliders built in the Modellflugclub Rossendorf without solar cells. This resulted in the function for the regression line

$$x(S_w) = 0,19 kg + 0,024 \frac{kg}{dm^2} \cdot S_w \qquad (8.11)$$

As an example of solar cells, we take those from Lemo-Solar [LeSol]. Their specific mass is $B_{SC} = (20 \ldots 26,6) g/dm^2$. This results in the new function for the mass m versus the wing area

$$m(S_w) = x(S_w) + B_{SC} \cdot k \cdot S_w \qquad (8.12)$$

The propeller must deliver at least the power according to Eq(5.11). Taking into account the efficiency of the actuator, motor and propeller, the electrical power is therefore required from the solar cells:

$$P_{SC\_req}(S_w) \geq \frac{m(S_w) \cdot g \cdot \left[v_{sr}(S_w, m) + v_{cr} \right]}{\eta_{ctr} \cdot \eta_{mot} \cdot \eta_{prop}} \qquad (5.11a)$$

However, the rate of descent also depends on the model mass m(S_w) and wing area S_w:

$$v_{si}(S_w) = \sqrt{\frac{m(S_w) \cdot g}{S_w \cdot \frac{\rho}{2}} \cdot \frac{\left(c_{dp} + \frac{c_l^2}{\pi \cdot S_w} \cdot l_\mu^2 + c_{dh} \right)^2}{\sqrt{\left(c_l^2 + \left(c_{dp} + \frac{c_l^2}{\pi \cdot S_w} \cdot l_\mu^2 + c_{dh} \right)^2 \right)^3}}} \qquad (5.4a)$$

Using Eq(5.4a) and Eq(8.12) in Eq(5.11a), we obtain the power P_{SC_requ} required by the solar cells as a function of the wing area S_w, Figure 8.21, red curve.
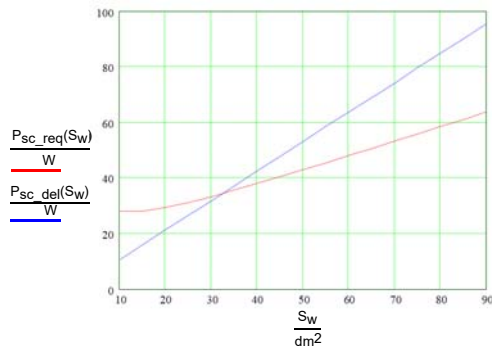

Fig 8.21 Requested and delivered power of the Solar cells with coverage k2 = 0.88

The following efficiency levels were assumed $\eta_{st} = 0{,}95$; $\eta_{mot} = 0{,}85$ und $\eta_{prop} = 0{,}6$; for cells we use $B_{sc} = 20$ g/dm^2.

The constant 1000W/m^2 applies to solar cells in space; due to atmospheric attenuation, 800W/m^2 is calculated on earth. The efficiency is usually $\eta_{SC} \approx 0.15$. This means that the power delivered by the cells can be written as follows

$$P_{SC\_del}(A_f) = k \cdot A_f \cdot 800 \cdot \frac{W}{m^2} \cdot \eta_{SC} \tag{8.13}$$

The blue curve in Figure 8.21 shows this function . At the intersection point at $S_w \approx 43$dm^2 the cell power just compensates the sink rate, the model flies horizontally. With a wing area $S_w \approx 75$dm^2 the cell power generates $P_{SC\_del} \approx 80$W and thus a climb speed of $v_{cr} = 0.7$m/s.
There is no room for manoeuvre for higher climb rates, e.g. reducing the flight mass from m(75dm^2) = 3.3kg $\rightarrow$ 2.5kg would only result in an improvement to $v_{cr} \approx 1$m/s.

In practice, the model could be realised with a wingspan b = 3m and a chord length of lμ = 250mm with 10 solar cells per half-span, each supplying around 12Vx7A. As battery 3S LiPo could be used for storage.

8.8 Start process of a model, calculated with the help of various precise mathematical approaches

8.8.1 Velocity v(t) and take-off roll distance s(t) without air resistance and rolling friction

The force F accelerating the model is equal to the thrust force F_T:

$$F = F_T$$

$$m*a = F_T \quad \rightarrow \quad a = F_T/m$$

For a motion process according to Fig 8.22 yields

$$v(t) = a*t + v_0 \, ,$$

and mit $v_0 = 0$ the speed curve is
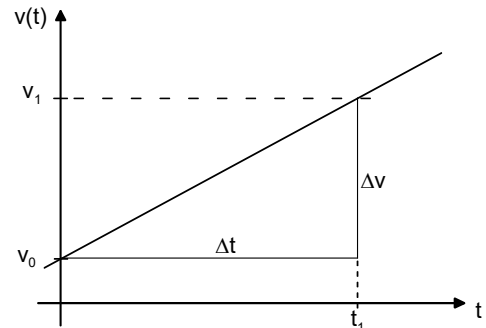
Fig 8.22 Velocity curve without resistances

$$v(t) = \frac{F_T}{mass} \cdot t \qquad (8.14)$$

Accordingly, the speed v_1 is reached at the time $t = t_1$. With uniform acceleration, i.e. a = const, the distance s(t) results from the mean value of both velocities:

$$s(t) = \frac{v_0 + v_1}{2} \cdot t$$

and with $v_0 = 0$:
$$s(t_1) = \frac{v_1}{2} \cdot t_1 \qquad (8.15)$$

Aus Gl(8.15):
$$t_1 = \frac{mass}{F_T} \cdot v_1 \qquad (8.14a)$$

in Gl (8.15):
$$s(t_1) = \frac{v_1^2}{2} \cdot \frac{mass}{F_T} \qquad (8.16)$$

example: mass m = 3kg, F_T = 6N. After what roll time t_{lo} does the model reach take-off velocity v_{lo} = 10m/s und how long is take-off distance?

mit $t_1 = t_{abh}$ und $v(t_1) = v(t_{abh})$ wird

nach Gl (8.14a) $\quad t_{abh} = v_{abh} * \dfrac{mass}{F_T} = 10 \cdot \dfrac{m}{s} \cdot \dfrac{3 \cdot kg}{6 \cdot N} = 10 \cdot \dfrac{m}{s} \cdot \dfrac{3 \cdot kg}{6 \cdot kg \cdot \dfrac{m}{s^2}} = 5s$

nach Gl(8.16) $\quad s(t_{abh}) = \dfrac{v_{abh}^2}{2} \dfrac{mass}{F_T} = \dfrac{\left(10 \cdot \dfrac{m}{s}\right)^2}{2} \cdot \dfrac{3 \cdot kg}{6 \cdot N} = 50 \cdot \dfrac{m^2}{s^2} \cdot \dfrac{1 \cdot kg}{2 \cdot \dfrac{kg \cdot m}{s^2}} = 25 \cdot m$

8.8.2 Speed v(t) and take-off roll distance s(t) taking into account the air resistance

The force F accelerating the model is now equal to the value obtained by subtracting the braking drag force F_D from the thrust force F_T:

$$F = F_T - F_D$$

If the speed v(t) has become so great that the drag force FD has reached the magnitude of the thrust force, i.e. $F_D = F_T$, an increase in speed is no longer possible.

From

$$F_D = \frac{\rho}{2} \cdot v^2 \cdot c_d \cdot S$$

folgt

$$v = \sqrt{F_D \cdot \frac{2}{\rho} \cdot \frac{1}{c_d} \cdot \frac{1}{S}}$$

und mit $F_D = F_T$

$$v_{max} = \sqrt{F_T \cdot \frac{2}{\rho} \cdot \frac{1}{c_d} \cdot \frac{1}{S}} \qquad (8.17)$$

example: $S = 60dm^2 = 0.6m^2$, $F_T = 6N$, aerodynamic quality $E = 10$, lift coefficient $c_l = 0{,}8$; drag coefficient $c_d = c_l/E = 0{,}08$. What maximum speed v_{max} can be achieved with the thrust F_T?

nach Gl (8.17)

$$v_{max} = \sqrt{6 \cdot \frac{kg \cdot m}{s^2} \cdot \frac{2}{1.25 \cdot \frac{kg}{m^3}} \cdot \frac{1}{0{,}08} \cdot \frac{1}{0.6 \cdot m^2}}$$

$$v_{max} = 14.14 \cdot \frac{m}{s}$$

However, it is not possible to make a statement about the velocity curve, such as according to Eq (8.14). For this, the process must be described as a differential equation (DGL):

$$m \cdot \frac{dv}{dt} = F_T - F_D$$

$$\frac{dv}{dt} = \frac{F_T}{m} - \frac{1}{m} \cdot \frac{\rho}{2} \cdot v^2 \cdot c_d \cdot S \qquad (8.18)$$

The required solution to this differential equation concerns the velocity v(t). Due to its non-linear cha-racter - v(t) occurs in the square - this can only be approximated analytically. Modelling the equation in a suitable calculation program, here Matlab&Simulink, is more detailed and also more elegant:
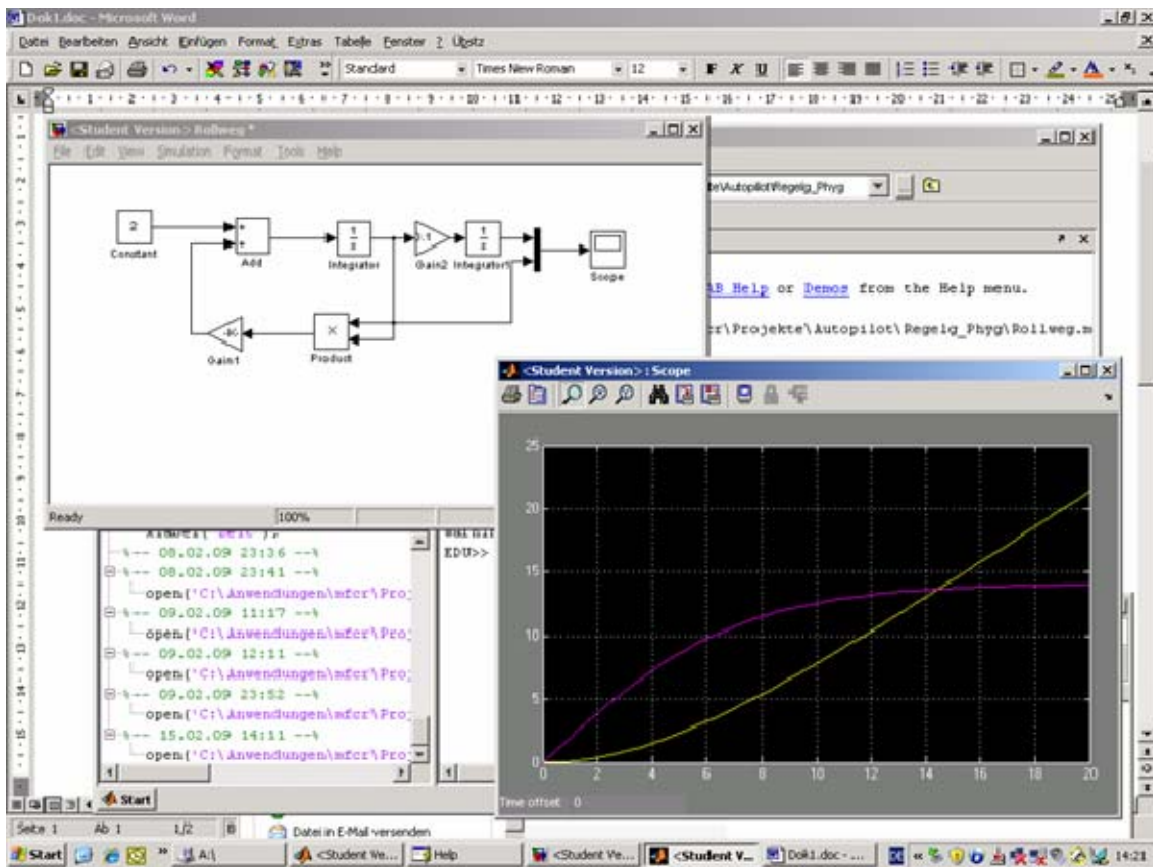
Fig 8.23 Simulink solution of the DGL(8.18). The velocity v(t) reaches its maximum at t ≈ 20s

The differential equation is described as a mathematical model at the top left. At the input of the first integrator, think of the derivative dv/dt. Then the quantity v(t) is obtained at its output. The velocity must be squared (block product) and multiplied by the corresponding coefficients $1/m$, $\rho/2$, cw, S and fed back to the input. The values of these coefficients are contained in the Gain block. At the top left, the constant is realised F_T/m. The second integrator generates the path s(t) from the velocity v(t) = ds/dt.

The solution shows the time course of velocity v(t), purple curve, and s(t), yellow curve. You can see that $v_{abh} = 10m/s$ is reached after $t_{abh} = 6s$, but now with a slightly longer rolling distance than calculated according to Eq (8.16), namely at s ≈ 30m. From this point onwards, the path should no longer be shown, as the model is now flying. The model reaches the maximum speed of $v_{max} ≈ 14m/s$ according to Eq (8.16) in t ≈ 20s, after it has already been in the air for 14s.

8.8.3 Velocity v(t) and take-off roll distance s(t), taking into account air resistance and rolling friction

The rolling friction F_{RF} must now be subtracted from the thrust force in addition to the drag force. The force F accelerating the model is then

$$F = F_T - F_D - F_{RF}$$

where $\quad\quad\quad\quad\quad F_{RF} = \mu(F_W - F_L)$

$$F_{RF} = \mu \cdot \left(m \cdot g - \frac{\rho}{2} \cdot v^2 \cdot c_l \cdot S \right)$$

The approach for the rolling friction force FR takes into account the fact that the model loads the ground less and less with increasing speed v - corresponding to increasing lift. In the literature, a typical value is $\mu \approx 0.06$. In extension of (8.18):

$$\frac{dv}{dt} = \frac{F_T}{m} - \frac{1}{m} \cdot \frac{\rho}{2} \cdot v^2 \cdot c_d \cdot S - \mu \cdot \left(g - \frac{\rho}{2} \cdot v^2 \cdot c_l \cdot \frac{S}{m} \right) \qquad (8.19)$$

When modelling the DGL, it is important that the influence of rolling friction is set to zero when the starting speed vabh is reached - an option that can be implemented very elegantly in the simulation using a comparator function:
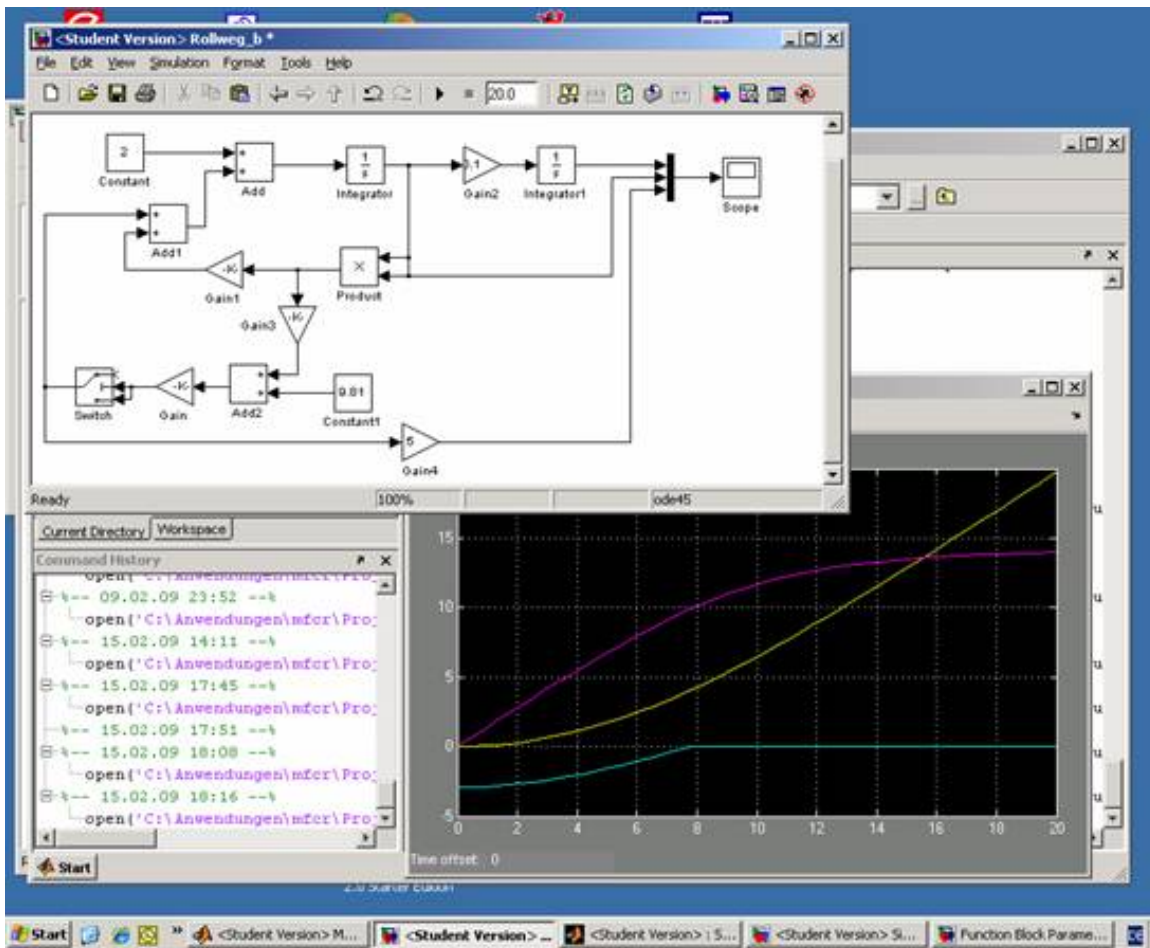
Fig 8.24 Simulink solution of the DGL(8.18). The lift-off speed of 10m/s is now reached at t_{abh} = 8s, the rolling distance is s = 40m. At this point, the influence of rolling friction is switched off.

Compared to the solution without rolling friction, Figure 8.23, the time of lift-off speed is extended to t_{abh} = 8s, the rolling distance is now about 40m. A comparator circuit *Switch* switches off the "rolling friction" signal path at the time t_{abh} because the variable $\mu(F_W - F_L)$, green curve, reaches the value zero.

<u>What we can learn from it</u>

The calculation of motion processes can be carried out with varying degrees of accuracy in the description of the physical facts. Using the take-off process of a model aircraft as an example, it is shown that the basic equations are sufficient for an initial estimate of the roll time and roll distance.

If the course of time and starting distance are of more interest, this requires a more refined description in the form of differential equations. In most cases, their solution is only possible with the help of common simulation methods.

	Basic equations	Consideration of air resistance	Consideration of air resistance and rolling friction
v_{abh}	10m/s	10m/s	10m/s
t_{abh}	5s	6s	8s
s_{abh}	25m	30m	40m
v_{max}	14m/s	14m/s	14m/s

Tabelle 8.2: Take-off values of a flight model calculated according to different mathematical approaches

8.9 Class F3K – Is it worth building lightweight models?

In the model flying class, the question is being discussed as to whether the greater height achieved by a heavier model does not also ensure a longer glide? [F3K-For]?
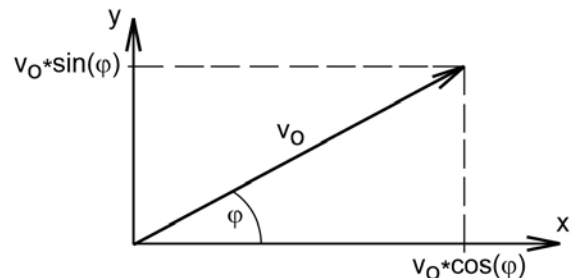

Fig 8.25a): Hand-launch of a F3K-model: world champion 2019, Henri Sander; Foto: Izabela Krawczyk [Kra19];   b) Splitting the oblique throw into vectors [uni_heidbg20]

The forces acting on a body with friction when thrown at an angle are described by a system of differential equations in vector form [uni_heidbg20].

The initial velocity acts

in x-direction with $v_o \cdot \cos(\varphi)$ $\dfrac{dx}{dt} = v_o \cdot \cos(\varphi)$

in y- direction with $v_o \cdot \sin(\varphi)$ $\dfrac{dy}{dt} = v_o \cdot \sin(\varphi)$

In ananolgy to Gl(8.19) it yields

in x-direction: $m \cdot \dfrac{d^2 x}{dt^2} = -\dfrac{\rho}{2} \cdot c_w \cdot A \cdot \cos(\varphi) \cdot \dfrac{dx}{dt} \cdot \sqrt{\left(\dfrac{dx}{dt}\right)^2 + \left(\dfrac{dy}{dt}\right)^2}$ $\dfrac{dx}{dt}(0) = v_o \cdot \cos(\varphi)$

(8.20a)

in y- direction: $m \cdot \dfrac{d^2 y}{dt^2} = -\dfrac{\rho}{2} \cdot c_w \cdot A \cdot \sin(\varphi) \cdot \dfrac{dy}{dt} \cdot \sqrt{\left(\dfrac{dx}{dt}\right)^2 + \left(\dfrac{dy}{dt}\right)^2} - m \cdot g$ $\dfrac{dy}{dt}(0) = v_o \cdot \sin(\varphi)$

(8.20b)

Using the Simulink programme applicable to these equations, Figure 8.26, the spin start is calculated with the following parameters:
        initial speed v_o = 25m/s; launch angle φ = 70^0
        mass = 100g, 150g, 200g; drag coefficient c_d: 0.01, 0.02;
From the maximum altitude reached, criterion $v_y(t) \to 0$, the duration tg for the glide is calculated with $tg_{max} = y(t)_{max}/v_{si}$ and the sink rate v_{si} according to Eq(5.4) with the parameters
        mass = 100g, 150g, 200g; link coefficient c_l = 1,0; drag coefficient $c_d = c_l/10$.
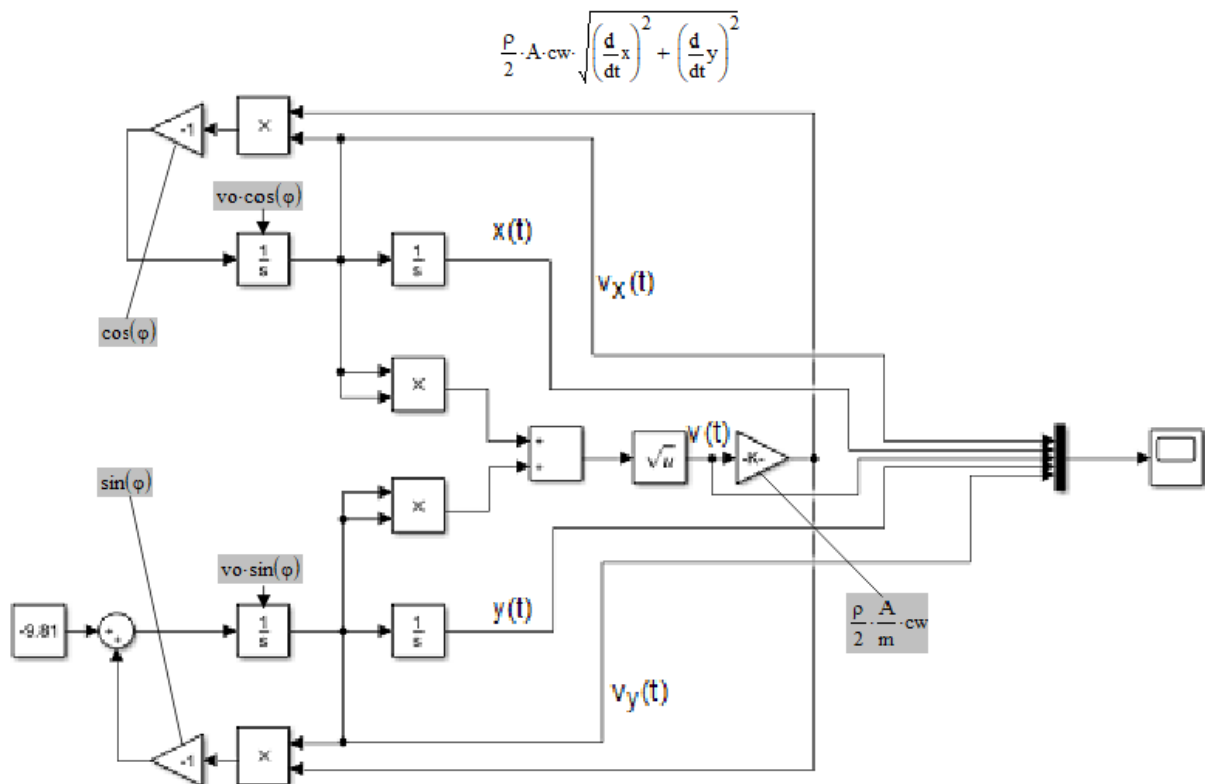
Fig 8.26 Si Simulink programme for the differential equation system Gln(8.20a,b)
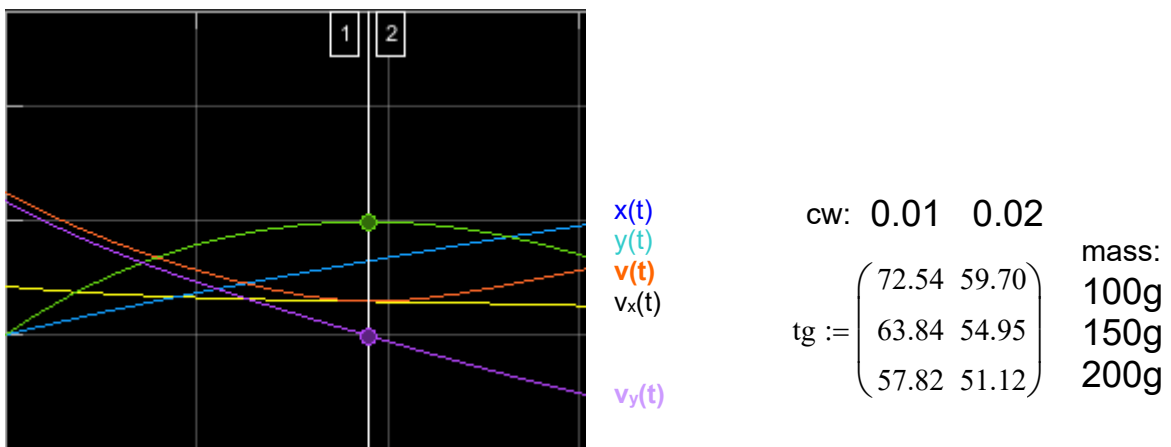
Fig 8.27 Solution curves of the DGL system Eq(8.20a,b) and numerical results for the sliding time tg/s

<u>What can we learn from this</u>

* with increasing mass, the achievable take-off altitude $y(t)_{max}$ becomes greater, Figure 8.27;
  with the same initial speed vo = 25m/s, the heavier model compensates better for the drag force ($\sim v^2$),
  which is particularly effective at the beginning of flight.
* With increasing mass, the rate of descent increases to such an extent that the height gain is
  cancelled out, the flight time in gliding flight becomes shorter.
* Lightweight construction is worthwhile!

8.10 Resümee

Submission of extracurricular cooperation partners for schools with all-day programmes (GTA)

Title of the offer/project/AG: Aeromodelling

Provider/name of cooperation partner: **Modellflugclub Rossendorf e.V.**
(Adresse, Tel., Fax, Email)   Hans Langenhagen
                                                                              Bautzner Landstraße 26
                                                                              01456 Radeberg OT Rossendorf
                                                                               mfcr@fz-rossendorf.de

Objectives: What should be achieved with the offer?
Model airplane construction: acquire the basics of craftsmanship, learn to read drawings; understand the load-appropriate use of materials;
Model flight: understanding the basics of flight physics, learning to control a model aircraft.
Internal impact: supporting physics lessons; **external impact**: publicising the grammar school through publications in newspapers and on the mfcR home page

Contents: What exactly will be done?
(Content, scheduling, involvement of students, requirements, age group, etc.)
Model airplane construction in the Rossendorf workshop and model flight in the gdb sports hall alternate on a weekly basis; in good weather conditions also flying on the mfcR club airfield (southern edge of Weißig).
1st course year: In the workshop, each student first builds a simple polystyrene and balsa glider, then groups of students build small remote-controlled motorised models (park flyers). In the sports hall, the students learn to control light - and therefore slow-flying - models (slow flyers); this is done using model flight simulators, teacher/student remote control systems and the club's own models.
2nd course year: depending on their interests, groups of students build a larger model (motorised glider) for use on the airfield and two slow flyers for indoor use. In terms of flying, they are offered the opportunity to take part in club comparison flights with motorised gliders, and they can practise simple aerobatics in the gym. Flight physics is also taught.
3rd course year: Design, partial construction and assembly of a model aircraft by groups of students. The flying tests should also be carried out with regard to the parameters achieved if possible (use of measurement technology)
4th course year: working on projects (e.g. minimum speed; maximum load ...)

Necessary material expenses: What is needed for the implementation? What does it cost?
(list in detail, indicate prices) for SY 2012_13
Material costs   874€
Labour costs   700€

Necessary labour expenses: What hourly remuneration is necessary? 17,50€

Specify criteria for the labour costs:
- Qualification, degree, certificates or similar.   Dipl.-Ing. of a technical specialisation
- Preparation effort and scope   ≥ 5h/event
- Pedagogical suitability, references if applicable
- Personal suitability
- Group size/how many pupils can take part, what age group? ≤15 (6 to 9 deg)

The all-day programme (GTA)) Model flying was offered at the Dresden-Bühlau secondary school (gdb) for over 10 years: from September 2009 to July 2019. Rudolf Zimmermann and Hans Langenhagen, who were responsible for the programme, started this working group in the hope of strengthening the club's youth membership, which was weakening at the time. The aim was also to introduce pupils to aviation topics that could be linked to their school physics and mathematics through an interesting programme.

In fact, the number of members of the youth group increased by around 10 pupils during the GTA period; the number of pupils joining from the lower classes and leaving from the upper classes was roughly balanced. However, there were also "drag" effects: Neighbouring children or friends who did not attend the high school joined.

Students with a longer-term interest remained in the working group even after the third year of the course; they now also built cleanly and purposefully and enjoyed taking part in comparison flights. The next few years will show how many of them grow up in the post_GTA_period.

As part of an all-day programme, the school requires two hours of supervision per week. As we had up to 10 interested students in the early days, we divided them up and alternated between model airplane construction in our club workshop and model flight - remote control - in the high school sports hall. This alone required a minimum of four supervisors; at the beginning, other club members were also very willing to help. In addition to motorised gliders from Höllein/Grüner construction kits, F. Schade also built hand-launch gliders (class F3K). The latter involved a self-built construction using balsa sheets as wings, on which the airfoil AG04 is milled. The company Aigner offers such Material. The mfcR also

continued to support the purchase of performance models in this class, which benefited interested pupils - including his son Paul when he was promoted to the national team/youth class.

The indoor remote control training proved to be very effective [La16]. For example, the 2012/13 school year showed that four of the five beginners were able to take part in the Lilienthal competition at the end of the school year in the Steutz holiday week after a short training period in both the hand-lunch class and the motorised glider class.

From around 2016, A. Scheffler's offer to provide advanced students with indoor aerobatics training proved to be interesting and attractive. Between three and five of them took up this offer with enthusiasm. However, only a few of them came to the Margon Arena, where Alfons organised flying time for club members and external guests on several Sundays.

At the beginning of our GTA years, the grammar school had only reached about half of its planned pupil capacity. It was no problem to get two school hours for training in the hall. This was then reduced to one school lesson, where there were more frequent blockages due to overruns in the sports lessons ahead of us. It became obvious that the sports teachers wanted us out of the hall. The official reason given was that the number of pupils had grown to 1000. Unofficially, we heard comments that our 3 to 5 pupils in a three-field hall (50 metres) would be considered a huge disproportion to the possible three school classes that could use the hall at the same time. We were granted alternative lessons at the weekend, but they were nowhere near as popular with the pupils as the lessons immediately after school.

But the club's capacity for coaching also dwindled, and from 2018 R. Zimmermann and I were once again coaching alone in the workshop. I moved the flying to our field: partly on the afternoons of the previous indoor times, partly on Saturdays, or I invited people to take part in competitions.

What we can learn from this

Offering model flying as part of an all-day programme (GTA) is definitely the most direct way to bring children/young people into contact with this subject. However, a club should have sufficient staffing potential to ensure that it can also look after the "flash in the pan" candidates for the minimum required first half of the school year while providing the same level of interesting support for the advanced students.

The idea of introducing pupils to aviation topics that could be combined with their knowledge of physics and maths was only realised in a few cases, see the previous sections 8.1 to 8.4. The topic of "take-off trolley" in particular could have been expanded with regard to investigating the measurement method for variable angles of attack and aspect ratios.

Incidentally, measurements on topics 8.1 and 8.2 produced the acceleration value a ⎕ 2.3m/s2 for drives of very different sizes .... Does this reflect the starting behaviour of brushless motors? Here too, comparative measurements with larger models would be interesting.

This publication is an attempt to describe the supervision of model flying offered to pupils at a grammar school during a 10-year period and to provide a theoretical basis for the sub-disciplines covered. Perhaps participants in this study group will not only be able to reminisce but also be inspired to deal with theoretical and metrological questions of any kind at a later date.

It is also possible, however, that there will be suggestions for aeromodelling colleagues who are thinking of setting up a student support programme in model flying.

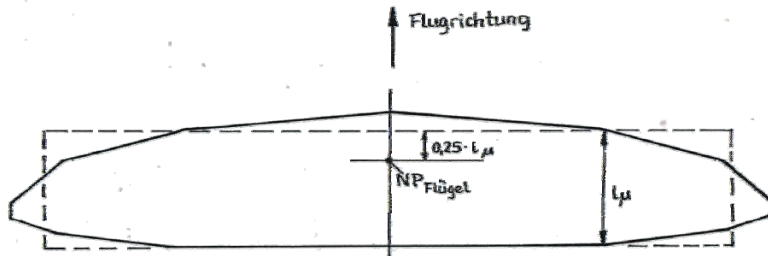Hans Langenhagen   Rossendorf, am 21. Juli 2021

9.0 Anhang

9.1 <u>Calculation of torque replacement wing</u>

The rectangular aerofoil geometry represents a special case of the possible wing shapes. However, this

offers the advantage of a clear aerodynamic view, e.g. for finding the aerodynamic center (neutral point NP_w). The reference wing chord $l\mu$ is determined for the real wing, shown as a line in Fig. 9.1, and the entire rectangular replacement wing is finally determined from the surface. Its neutral point is as known at $x_{Nw} = 0.25*l\mu$

Fig 9.1: The size and position of the replacement rectangular wing are calculated from the real trapezoidal ground plan of the aerofoil

JUST [Ju65] gives the following calculation rule for the double trapezoidal wing, Fig 9.2:

Wing surface
$$S_w = s_1 \cdot (l_1 + l_2) + s_2 \cdot (l_2 + l_3) \qquad 9.1)$$

Reference wing chord:
$$l_\mu = \frac{2}{3 \cdot S_w} \cdot \left[s_1 (l_1^2 + l_2^2 + l_1 \cdot l_2) + s_2 \cdot (l_2^2 + l_3^2 + l_2 \cdot l_3) \right] \qquad (9.2)$$

Position of the replacement wing:

$$x_E = \frac{1}{3 \cdot S_w} \cdot \left[x_2 \cdot s_1 (l_1 + 2 \cdot l_2) + x_2 \cdot s_2 \cdot (l_3 + 2 \cdot l_2) + x_3 \cdot s_2 \cdot (l_2 + 2 \cdot l_3) \right] \qquad (9.3)$$
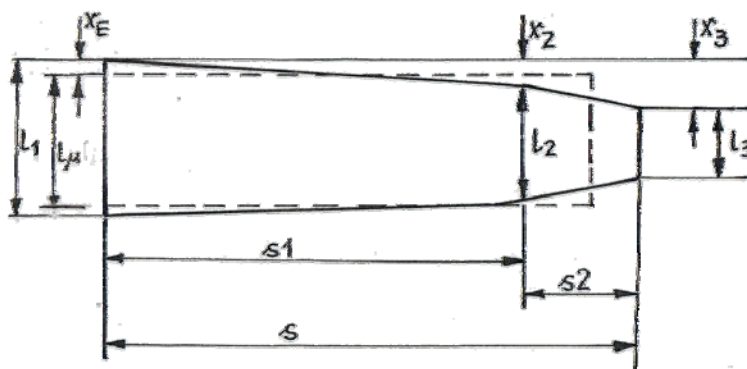
Fig 9.2: Zur Ermittlung des Rechteck-Ersatzflügels aus dem Doppel-Trapezflügel

Example 9.1
Where is the neutral point x_{Nw} of the Strolch trapezoidal wing with the following dimensions, see Fig 7.1a:
s_1 = 3.5dm, s_2 = 2.1dm, l_1 =1.6dm, l_2 = 1.6dm, l_3 = 1.0dm, x_2 = 0.0dm, x_3 = 0.154dm

First, we determine the position and size of the (rectangular) moment-replacement wing using the equations Eqs. 9.1 to (9.3). Based on this, we obtain the new centre point position of the trapezoidal wing:

according to Eq(9.1):
$$S_w = 3,5dm \cdot (1,6dm + 1,6dm) + 2,1dm \cdot (1,6dm + 1,0dm) = 16,7dm^2$$

according to Eq(9.2):

$$l_\mu = \frac{2}{3 \cdot 16,7dm^2} \cdot \left[3,5dm(1,6dm^2 + 1,6dm^2 + 2,56dm^2) + 2,1dm \cdot (1,6dm^2 + 1,0dm^2 + 1,6dm^2) \right] = 1,51dm$$

according to Eq(9.3) where $x_2 = 0$:

$$x_E = \frac{1}{3 \cdot 16,7\,dm^2} \cdot \left[15,4 \cdot 2.1\,dm^2 \cdot (1,6\,dm + 2 \cdot 1\,dm)\right] = 2,33\,mm$$

The neutral point x_{Nw} of the rectangular wing is at $x_{Nf\_R} = 0,25*l_\mu = 0,25*1,51\,dm = 0,377\,dm = 37,7\,mm$ from its leading edge. This means that the neutral point of the trapezoidal wing is 40 mm away from its leading edge $x_{Nw} = x_{Nw\_R} + x_E = 37,7\,mm + 2,33\,mm = 40\,mm$. The measure for x_{Nf} can then be used to determine the neutral point of the overall model x_N (aerodynamic center of whole model) according to equations Eqn(7.5a) to (7.5c) and Fig 7.12. From this, the position of the centre of gravity x_S is finally calculated for a given stability measure, see Eq(7.6b).

Literatur

[A80]   Althaus, D.
Profilpolaren für den Modellflug
Neckar-Verlag VS-Villingen, 1980, ISBN 3-7883-0158-9

[A320_a]   Morgenstern/Plath
Airbus A330/A340 – Die großen Europäer
Motorbuchverlag Stuttgart, 1996

[A320_b]   http://de.wikipedia.org/wiki/Airbus-A320-Familie#Zwischenf.C3.A4lle > Technische Daten
geprüft: Mai 2014

[A320_c]   http://www.aero.de/forum/Allgemeines-aus-der-Luftfahrtbranche/Gleitzahl-eines-Airbusses-A320-/
> clean configuration

[Aer19]   Leistungsdiagamm für Elektro-Luftschrauben Cam-Carbon,
Grafik im Firmenkatalog Aeronaut 2019

[Alt20]   https://www.aerobtec.com gepr. 2019

[AS19]   Scheffler, A., persönliche Mitteilung 2019

[BB14]   Böswirth, L. und S. Bschorer
Technische Strömungslehre
10. überarbeitete und erweiterte Auflage 2014, Springer Vieweg

[BauH2/20] Baumeister, W.
Thermik $\geq$ 0 – Django Neon XL von Sansibar
FMT_H02/2020, S.74 … 81

[BauH8/20] Baumeister, W.
Jäger der verlorenen Thermik – Stratus 4000 von Schmierer/Valenta
FMT_H08/2020, S.98 … 105

[Beu58]   Beuermann, K.
Wie erreiche ich eine gute Längsstabilität
Der Flugmodellbau, H.1 , H2 1959
C. Lange Verlag Duisburg

[Böl90]   Bölkow, L.
Ein Jahrhundert Flugzeuge
VDI-Verlag GmbH, Düsseldorf 1990, ISBN 3-18-400816-9

[Br80]   Bruß, H.
Elektroflug
Franzis-Verlag München 1980

[Br/Frie98] Brenner, Th. und U. Friedemann
Programm zur Berechnung der Geschwindigkeitspolare unter Einbeziehung
windkanal-vermessener Profile
Vortrag auf DGLR- Nachwuchstagung 1998 Bremen

[Brü21]   Brückner, N., persönliche Mitteilung 1921

[Bü10]   Büchi, R.
Faszination Quadrocopter
Verlag für Technik und Handwerk, Baden-Baden, 2010

[Bü11]   Büchi, R.
              Brushless-Motoren und -Regler
              Verlag für Technik und Handwerk, Baden-Baden, 2011

[DJ20]   DJI Mavic Mini im Test (drohnen.de) gepr. 2020

[EK07]   Elle, T. und M. Klein
              Luftbilder aus dem Modellflugzeug – Untersuchung zu Einsatzmöglichkeiten in der
              Landwirtschaft
              Landeswettbewerb Sachsen „Jugend forscht" 2007, eingereicht von Jugendlichen des
              Modellflugclub Rossendorf e.V.;
              Vortrag auf der DGLR-Nachwuchstagung in Berlin, 2007

[F3K-For]   Drehwurftechnik SAL leichter gleich höher? steiler gleich höher?
              https://www.rclineforum.de/forum/board19-fl%C3%A4chenflugmodelle/board27-
segler/board86-hlg-sal-dlg/75448-drehwurftechnik-sal-leichter-gleich-h%C3%B6her-steiler-gleich-
h%C3%B6her/ gepr. 2021

[Gerh]   Gerhard, W.
              http://www.wolfgang-gerhards.de/zip/schwerpunkt.pdf gepr. 2021

[Gie15]   Giese, G.: Das kleine LiPo-Abc, http://www.elektromodellflug.de/ gpr. 2019

[Hack19]   https://www.hacker-motor-shop.com/ > A10-13L

[Hack21]   https://www.voelkner.de/ > Hacker A40-14L-V4-14-Pole kv 355

[HebH10/20]   Hebbeker, P.
              Test: EasyStar 3 von Multiplex
              FMT, H.10/2020, S.100
              https://www.multiplex-rc.de/

[Hep18]   Hepperle, M.
              https://www.mh-aerotools.de/ > Model Aero > Propellers   gepr.2018

[HK85]   Haftmann, B; Kiekebusch, B.
              Details zur Optimierung des Reiseflugwiderstandes des Airbus A320
              DGLR-Jahrbuch 1985, S. 89-1 … 89-36

[HL10]   Hapag-Lloyd-Flug 3378 – Wikipedia

[Ho81]   Hofmann, R.
              Überlegungen zum Kräftespiel beim Hochstart
              Flug- und Modelltechnik (FMT), Baden-Baden, H.4/1981, S.342-344

[Jant2b]   http://www.piotrp.de/SZYBOWCE/dszd42.htm

[Jant78]   Firmenschrift
              Flughandbuch des Segelflugzeuges SZD-42-2 JANTAR 2B
              Ausgabe II vom 14.11.1978
              Szybownictwa „PLZ Bielsko"

[Jä40]   R. Jäschke
              Flugzeugberechnung
              R.Oldenburg-Verlag München und Berlin 1949

[Ju65]   Just, W.
              Flugmechanik
              Verlag Flugtechnik Stuttgart 1965

[JW04]   Jach, F. und S. Wolrab
Entwicklung eines Leistungssegelflugmodells
Vortrag auf DGLR-Nachwuchstagung, Dresden 2004
eingereicht von Jugendlichen des Modellflugclub Rossendorf e.V.

[Kra19]   Izabela Krawczyk
https://www.aeroclub-nrw.de/tag/zdf/

[KN77]   Kopenhagen, W; Neustädt, R
Das große Flugzeugtypenbuch
transpress, VEB Verlag für Verkehrswesen, Berlin 1977

[La91]   Langenhagen, H.
RC-Segelflugmodelle
Entwurfsmethodik, Technologie, Flugpraxis
eingereicht bei Transpress VEB Verlag für Verkehrswesen, Berlin 1985
mit Status *Satzreife* gekündigt 1991

[La94]   Langenhagen, H. und R. Zimmermann
Messungen am fliegenden Fernlenkflugmodell – ein Stück experimentelle Flugphysik
FMT-Kolleg Nr. 17, 1994, Verlag für Technik und Handwerk GmbH, Baden-Baden

[La16]   Langenhagen, H.
Nachwuchsgewinnung im Schülerbereich – Rossendorfer Versuche –
Vortrag zur Übungsleiterschulung Modellflug, Haus der Luftsportjugend Laucha, 03.2016
http://mfc-rossendorf.de/fileadmin/mfcr_upload/mfc/Angebote/Schulen/Erfahrungen/nachwuchsSch%C3%BCler_c.pdf

Langenhagen, H.
Recruiting pupils for Aeromodelling
Lecture at the Annual Meeting of FAI Aeromodelling Commission (CIAM), 04. 2016, Lausanne
http://mfc-rossendorf.de/fileadmin/mfcr_upload/mfc/Angebote/Schulen/Erfahrungen/recruitment_EN.pdf

Langenhagen, H.
Report: Modellflug in der Schule
www.vth.de/fmt/fmt-blog/lorem-ipsum-dolor-sit-amet-consetetur-sadipscing-elitr
FMT-online 18.07.2016

[La18]   Langenhagen, H.
Lift off from the take-off trolley – uplift force without side effect
FAI-CIAM-Meeting/SC Education, April 2018, Lausanne
https://www.mfc-rossendorf.de >CIAM Flyer zu unserem Schulprojekt >Startwagen_EN

[La19]   Langenhagen, H.
Aeromodelling and Aeronautic - A review through History and Physics of Aeronautic –
FAI-CIAM-Meeting/SC Education, April 2019
https://www.mfc-rossendorf.de > News >Unser Wort bei der CIAM in Lausanne >Anhang_EN

[Lab 08]   MIT OpenCourseWare Lab 8 Notes – Basic Aircraft Design Rules 6 Apr 06 –
https://ocw.mit.edu/courses/16-01-unified-engineering-i-ii-iii-iv-fall-2005-spring-2006/ffbff8a4985ee6ea819afb90c40834e3_spl8.pdf

[LeSol]   https://lemo-solar.de/shop/modellbautechnik.php (alter shop, wird nicht mehr gepflegt)
https://shop.lemo-solar.de/ (neu)

[LH]   Lernhelfer/Schülerlexikon > Physik > Gleichstrommotor
https://www.lernhelfer.de/schuelerlexikon/physik/artikel/gleichstrommotor#

[MB10]   http://www.urlaub-und-hobby.de/metallbaukasten/so04dt.html > sonstige Projekte
              > Kenngrößen von Gleichstrommotoren

[Mu78]   Musil, M.
              Aerodynamika modernich leteckých modelu Prag, 1978

[Mü14]   Müller, M. www.eCalc.ch
              Elektrisch, aber richtig; Artikelserie in Aufwind 2014/H4 bis 2016/H2

[MPX21]   Roxxy-Antriebsfibel
              https://www.multiplex-rc.de/Downloads/Multiplex/Kataloge/Roxxy-Motoren-Fibel-web.pdf gepr.
              März 2021

[NaWi14]   Nacht der Wissenschaften 2014; Poster Leibniz-Institut für Polymerforschung Dresden
[Neu67]   Neunaß, E.
              Praktische Strömungslehre
              VEB Verlag Technik Berlin, 1967

[Pi16]   https://shop.pichler.de/Startseite > XQ-Card   gepr. 2016

[Reis21]   https://www.reisenauer.de/aid-2195-Leopard-LC250-30-6pol-5550KV-br-mit-Micro-
              Edition-5-1NL-T.html   gepr. 04. 2021

[R&G20]   https://shop1.r-g.de/list/Carbon-und-Glasfaser-Staebe---Rohre gepr. 2020

[Sc13]   Schmidt, F.
              Kräfteeinwirkungen am Flugmodell
              – welche Kraft muss eine Rudermaschine wirklich aufbringen? –
              Landeswettbewerb Sachsen „Jugend forscht" 20013, eingereicht von Jugendlichen des
              Modellflugclub Rossendorf e.V

[Sche02]   Schenk, H
              Abschätzung des Antriebs von Elektroflugmodellen
              https://www.rc-network.de/threads/absch%C3%A4tzung-des-antriebs-von-
              elektroflugmodellen.11779892/

[Sche03]   Schenk, H.
              Der Standschub von Propellern und Rotoren
              http://www.rc-network.de/magazin/artikel_02/art_02-0037/Standschub.pdf
              gepr: Jan. 2011

[Sche07]   Schenk, H.
              PropCalc 3.0 für Windows; - Einführung, Fortschrittsgrad&Co, Prop und Motor -
              http://www.drivecalc.de/PropCalc/index.html   gepr: Jan. 2011

[Schu80]   Schulze, Horst
              Luftschrauben für Modellantriebe
              Transpress VEB Verlag für Verkehrswesen, Berlin 1980

[Se89]   Selig, M., Donovan, F. and Fraser, D. B.
              Airfoils at low speeds
              Soartech 8, H.A.Stokely, publisher
              1504 North Horseshoe Circle, Vorginia 23451, USA
              http://airfoiltools.com/airfoil/details?airfoil=s7012-il gepr. 2020

[Seid62a]   Seidler, Fritz
              Die stationären Flugzustände
              Franksche Verlagsbuchhandlung, Stuttgart 1962

[Seid62b]   Seidler, Fritz
Die Stabilität in der Flugmechanik
Franksche Verlagsbuchhandlung, Stuttgart 1962

[SI]   Mit den Flügeln der Sonne -- Solar Impulse 2: ohne Treibstoff um die Welt
https://www.scinexx.de/service/dossier_print_all.php?dossierID=91238 gepr.2021

[SLZ77]   Schulze,H., Löffler, A., Zenker, W.
Modellflug in Theorie und Praxis
transpress VEB Verlag für Verkehrswesen, Berlin 1977

[Sz42]   Schmitz, F.W.
Aerodynamik des Flugmodells
Luftfahrt-Verlag Walter Zuerl; Steinebach –Wörthsee, 6. ergänzte Auflage, 1975